

Study of variations of the dynamics of the Metal-Insulator transition of thin films of
Vanadium Dioxide with an ultra-fast laser

Elizabeth L. Radue

Mount Airy, Maryland

Master of Science, College of William and Mary, 2011
Bachelor of Arts, Mount Holyoke College, 2009

A Dissertation presented to the Graduate Faculty
of the College of William and Mary in Candidacy for the Degree of
Doctor of Philosophy

Department of Physics

The College of William and Mary
August 2016

©2016
Elizabeth L. Radue
All rights reserved.

APPROVAL PAGE

This Dissertation is submitted in partial fulfillment of
the requirements for the degree of

Doctor of Philosophy



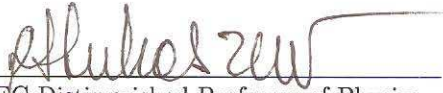
Elizabeth L. Radue

Approved by the Committee, August, 2016



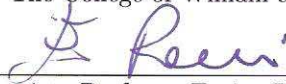
Committee Chair

Associate Professor of Physics Irina Novikova, Physics
The College of William and Mary



VMEC Distinguished Professor of Physics

R. A. Lukaszew, Physics
The College of William and Mary



Associate Professor Enrico Rossi, Physics
The College of William and Mary



Associate Professor Mumtaz Qazilbash, Physics
The College of William and Mary



Dr. Russell A. Wincheski, Aerospace Technologist
NASA Langley Research Center

ABSTRACT

Vanadium dioxide is an intensely studied material, since it goes through an insulator-metal transition at a critical temperature just above room temperature at 340 K. The dramatic change in conductivity and the easily accessible transition temperature makes it an attractive material for novel technologies. Thin films of VO_2 have a reversible transition without any significant degradation in contrast, and depending on the microstructure of the films, the properties of the transition are tunable. In this work, I study the dynamics of the insulator-transition in thin films grown on different substrates using a pump-probe configuration. The energy needed to trigger the transition, as well as the time constants of the change in reflectivity are affected by the strain in the VO_2 films. I also characterized the samples using Raman spectroscopy and XRD measurements in order to identify what underlies the differences in behavior. Finally, in collaboration with Dr. Yamaguchi's group at RPI, I show that it is possible to trigger the transition using a THz pulse that directly pumps energy into the lattice, and at lower energies than needed to pump films by photoinducing the electrons across the band gap.

TABLE OF CONTENTS

Acknowledgments	iv
Dedication	v
List of Tables	vi
List of Figures	vii
CHAPTER	
1 Motivation for studying VO ₂	2
2 Background on Insulator-Metal Transition in VO ₂	5
2.1 Phases of VO ₂	5
2.2 Band Theory	7
2.3 Insulator-Metal transition in VO ₂	10
2.4 Optical properties of VO ₂	11
2.5 Ultrafast studies of VO ₂	12
2.6 Microstructure effects on IMT	13
3 Characterization of heat induced IMT in thin films	15
3.1 Description of samples	15
3.2 Continuous Wave Reflection and Transmission measurements	16
3.3 X-Ray Diffraction	16
3.3.1 Grain size	24
3.4 Continuous Wave Measurements	24
3.4.1 Modeling Reflection and Transmission	29
3.5 Raman Spectroscopy	30

3.5.1	Raman Scattering	30
3.5.2	Raman spectroscopy experimental set up	31
3.5.3	Conclusion	39
4	Ultrafast Pump-probe Experimental Set Up	40
4.1	Ultrafast Laser system	40
4.2	Characterizing Pulses	42
4.2.1	Pulse duration	42
4.2.2	Fluence and Spot size	45
4.3	Pump-probe set up	46
5	Phase Diagram of the Dynamics of the Ultrafast Response	49
5.1	Introduction	49
5.2	Measurements of the IMT Temporal Evolution	50
5.3	Mechanisms of Ultrafast MIT	54
5.4	Conclusion	59
6	VO ₂ sub-picosecond polarization dependent response	61
6.1	Sub-picosecond response	61
6.2	Changing pulse duration (Δt)	64
6.3	Electro-Magnetic Field	66
6.4	Analysis and Conclusion	69
7	Effect of inhomogeneities and substrate on the recovery dynamics of the metal-insulator transition in VO ₂ thin films	71
7.1	Introduction	71
7.2	Experimental setup	74
7.3	Theoretical modeling of inhomogeneities	77
7.4	Theoretical modeling of the relaxation dynamics of the MIT	82

7.5	Effect of inhomogeneities on the relaxation dynamics of the photo-induced MIT	88
7.6	Conclusions	94
8	Directly pumping the lattice of VO ₂ films with THz pulses	97
9	Conclusion and Outlook	104
9.1	Summary	104
9.2	Outlook	105
	Bibliography	107
	BIBLIOGRAPHY	107
	Vita	119

ACKNOWLEDGMENTS

I would like to thank my advisor Irina Novikova for all her guidance and support in this project. I would also like to thank Ale Lukaszew, both for the generous use of her lab and for her mentorship. I would like to thank Enrico Rossi for working with us on the theory, Buzz Wincheski for allowing us to use the facilities at NASA Langley, and Dr. Yamaguchi and his student Zhengping Fu for aiding us with the THz pump measurements at RPI. I would also like to thank all the students I worked with, particularly Matt Simons, Lei Wang, Martin Rodriguez-Vega, Evan Crisman, Ashna Aggarwal, and Haley Bauser. Thanks also go to my fellow lab mates Gleb and Mi, for patiently listening to me complain about temperamental lasers.

I would also like to express my gratitude to all the excellent physics teachers that have gotten me this far, in particular to my undergraduate advisor Shubha Tewari. Thank you for all your encouragement and your continued support over the years. Finally, I would like to extend profound thanks to all my friends and family, Peter, Nanette, Mariah, and Edward, who have been my cheerleaders in the past 6 years. You kept me laughing and gave me the confidence I needed to see this through.

I present this thesis in honor of my parents, Peter and Nanette Radue.

LIST OF TABLES

3.1	Comparison of measured monoclinic VO ₂ Raman resonances with previously reported results.	33
3.2	Average transition temperature, grain size, and estimated value of constant A for VO ₂ films grown on each substrate. The error bars for the values of A are calculated using 1° uncertainty in the transition temperature measurements	38
5.1	Summary of basic properties of the two VO ₂ samples.	60
7.1	Comparative table between VO ₂ /TiO ₂ , and VO ₂ /Al ₂ O ₃ sample parameters.	82
7.2	Parameters of VO ₂ and substrates.	90

LIST OF FIGURES

2.1	Schematics of the VO_2 lattice structure and electron energy band structure below and above the critical MIT temperature. High-temperature metallic phase corresponds to the tetragonal (or rutile) lattice structure. Upon cooling through the thermally induced phase transition the V^{4+} ions dimerize along the c-axis of the tetragonal phase, breaking the symmetry and forming monoclinic lattice cells. At the same time the d band splits into two different bands, while the π^* band shifts above the Fermi level E_F , drastically decreasing electron conductivity.[1]	6
2.2	Here is a graph based on the Hubbard model, showing two avenues that a material could go through a insulator-metal transition. The band-controlled model changes the relationship between U and t , creating localization do to the energy cost of moving electrons. The filling controlled model changes the number of electrons in a band, which makes U play a larger role in increasing the energy cost of moving electrons within the lattice[2]	9
2.3	Measured complex dielectric constants for VO_2 , both in bulk and for a 1000 Å film on Al_2O_3 . a) is the real part of ϵ , and b) is the imaginary part at room temperature, and c) and d) show the same for the material heated up to 355 K. From Ref. [3].	12
3.1	Here is a picture of the various VO_2 thin film samples used in these studies.	16
3.2	Atomic force microscopy images of our samples taken at UVA.	17
3.3	X-ray diffraction uses the interference between layers in a crystalline material. The x-rays constructively interfere when Bragg's Law (as shown above) is satisfied. By scanning over θ we can find for what angles there is a diffraction point, and from there calculate d	18
3.4	This is a calculated powder XRD pattern of M1- VO_2 . The peaks we see in our $\theta - 2\theta$ measurements are consistent with the peaks seen here.[4]	19
3.5	In order to access different family of planes within a thin film sample, it is necessary to rotate the stage. $\theta - 2\theta$ scans are when the source and detector move to change the incident angle of the x-ray beam. ϕ rotates the stage about the normal of the sample surface. χ tilts the stage, rotating the sample's normal with respect to the incident beam.	20

3.6	Here is the XRD data from VO ₂ on Al ₂ O ₃ . a) shows the $\theta - 2\theta$ curve, which shows the strong substrate signal and the weaker VO ₂ peak. Because the x-ray source has both Cu K- α 1 and K- α 2, the narrower substrate peak is narrow enough to resolve both wavelengths. b) is a depiction of the (020) plane in M-VO ₂ . c) is an asymmetric $\theta - 2\theta$ scan at $\chi=44.8^\circ$ of the M-VO ₂ plane (011). d) shows the ϕ -scan at $\chi = 44.8$, showing 3-fold symmetry. . . .	21
3.7	Here is the XRD data from VO ₂ on TiO ₂ . a) shows the $\theta - 2\theta$ curve, which shows the strong substrate signal and the weaker (011) R-VO ₂ peak. b) depicts how the film lattice would be oriented in either phase. c) show the asymmetric (110) M-VO ₂ scan, and d) shows us a ϕ -scan with tetragonal symmetry, indicating there is clamping of the film by the substrate.	22
3.8	Here is the XRD data from VO ₂ on SiO ₂ . a) shows the $\theta - 2\theta$ curve, which shows the strong substrate signal and the weaker (011) M-VO ₂ peak. There are no peaks from the film in the ϕ -scan, indicating the film is polycrystalline.	23
3.9	Here are measurements taken by Cesar Clavero and Irina Novikova looking at the reflection (a)) and transmission (b)) for VO ₂ on Al ₂ O ₃ . As we move from visible light into the infrared regime, the response becomes more dramatic for both transmission and reflection.	25
3.10	The experimental set up of our continuous wave measurements. Beam was focused on sample, and the polarization of the incident beam was controlled with a half-wave plate. Films were mounted on a peltier heater allowing us to control the temperature. We looked at both transmission and reflection measurements.	26
3.11	Here are continuous wave measurements of the reflection off of VO ₂ on a) Al ₂ O ₃ , b) TiO ₂ , and c) SiO ₂ , taken with a 780 nm diode laser. The reflection drops as the films are heated through the transition, and we see all the films show the characteristic hysteresis of the transition. Each film has a very different transition temperature T_c and transition width, which can be explained by the different microstructures we found in each film. . .	27
3.12	Here is the normalized reflection off of VO ₂ on TiO ₂ at 780 nm. The change in reflectivity is different depending on the orientation of the film, due to the mono-crystalline nature of the film and the anisotropic nature of VO ₂	28
3.13	Here are the calculations of M-VO ₂ on TiO ₂ . The optical constants were measured by ellipsometry. a) shows the s and p reflectivity as a function of incident angle for one orientation of the film. b) shows the p-polarized reflection at an incident angle of 20° as we rotate the sample and c) shows the change in reflection as we rotate the polarization.	29

3.14	Raman spectra for VO ₂ thin films deposited on quartz substrates obtained using different excitation lasers.	32
3.15	Evolution of Raman spectra for VO ₂ thin films deposited on (a) quartz, (b) sapphire, and (c) rutile substrates through the thermally induced MIT. Dashed vertical lines indicate expected positions of M-VO ₂ Raman resonances. Unmarked peaks are substrate resonances. Two particularly strong rutile peaks are out of range in (c) in order to highlight the much weaker VO ₂ peaks.	34
3.16	Comparison of the MIT evolution for VO ₂ thin films grown on different substrates. Left column: Reflectivity measurements with a 780 nm cw laser. Right column: Change in Raman peak intensity in each film. (a) VO ₂ film on quartz, peak 224 cm ⁻¹ . (b) VO ₂ film on sapphire, peak 224 cm ⁻¹ . (c) VO ₂ film on rutile, peak 309 cm ⁻¹ . For the anisotropic rutile sample, the reflection for two orthogonal polarizations is shown. Some variation in transition temperature between the two detection methods may be due local heating due to focused pump beam in the Raman spectrometer. Vertical lines indicate the temperature for the phase transition temperature T _c . . .	36
4.1	This is the measured bandwidth of the ultrafast pulse coming out of the Legend amplifier (the pulses used for most of this work). By fitting with a Gaussian, we can get an estimate of the limit on the duration of the pulses coming out of the system.	43
4.2	An autocorrelator divides the pulse into two pathways. Recombining the beams in a Beta Barium Borate (BBO) crystal will only produce blue light when the pulses overlap both temporally and spatially. By looking at the profile of the blue light we can determine the pulse duration Δt	44
4.3	The image from the camera of our autocorrelator shows the SHG from the combination of the two pulses in the BBO crystal. The width of the beam is related to the pulse duration. Each pixel is 7.4 microns.	44

4.4	Schematics of the optical pump-probe experimental setup. The output of the amplified ultrafast laser is split into weak probe and strong pump beams using a (20/80) beamsplitter (BS). The energy of the pump pulses is controlled by the variable neutral-density filter ND1, while the probe beam was sent through a computer-controlled variable delay stage (VDS) and further attenuated using ND2 (OD=3.0). The probe and pump beams were focused on the same spot at the surface of the sample, placed inside a cryostat, using 250-mm and 500-mm lenses, correspondingly. The reflected probe power was measured by a photodetector (PD), and further analyzed using a lock-in amplifier.	47
5.1	Sample time-dependent changes in the probe reflection corresponding to various dynamical phases of MIT, measured for (a) VO ₂ /TiO ₂ and (b) VO ₂ /Al ₂ O ₃ samples. The pump pulse hits the sample at zero time, and positive delay times correspond to the probe beam interacting with the sample after the pump beam.	50
5.2	"Slow growth" of relative reflectivity with time, measured for (a) VO ₂ /TiO ₂ and (b) VO ₂ /Al ₂ O ₃ samples with pump fluence of 15 mJ/cm ² at 298 K, using a log-log scale ("slow growth" phase data in Fig.5.1). Log-log scale clearly shows two time scales of growth for both films. For the VO ₂ /Al ₂ O ₃ sample, the initial faster reflectivity growth (time constant 7.4± 0.3 ps) for the first 40 ps was followed by much slower growth with time constant of 33± 8 ps. For the VO ₂ /TiO ₂ film the switch occurred at approximately 67 ps, from the time constant 6.3±0.2 ps to 15.0± 0.6 ps.	51

5.3	Threshold measurements for the onset and for the full IMT of VO ₂ thin films grown on a)TiO ₂ and b)Al ₂ O ₃ . Blue stars/Green diamonds correspond to the threshold fluence needed to see a 2% rise in reflectivity at 10 ps and 50 ps, correspondingly. The red squares and cyan triangles correspond to the fluence required to reach the reflectivity value for a fully metallic film in the first 10 ps and 50 ps, correspondingly. The purple circles indicate the boundary where the "slow-growth" phase starts Φ_{SM} . To define this boundary, we took several measurements of the probe reflectivity $\Delta R/R$ as a function of time for the first 20 ps at a range of pump fluences, fitted their linear slopes, and then found fluence values at which the slope becomes indistinguishable from zero within the measurement uncertainty. The dashed lines are the calculated photo-excited electron densities at the front and the back of the films. The shaded region between the solid lines is calculated fluence needed to bring the films up to the transition temperature.	52
6.1	This is a measurement taken with the sample of VO ₂ on TiO ₂ . The sub-ps feature can be clearly seen in this graph when the pump and probe are cross polarized.	62
6.2	These measurements were taken with a pump power of 11 mJ/cm ² , and a pulse durations of 520 fs, with both the pump and probe p-polarized. When heated, there is no longer a long term change in $\Delta R/R$, and the feature is no longer present.	63
6.3	Here are a series of measurements of VO ₂ in the pump-probe configuration. The pulse length (as measured with an autocorrelator) goes from 130 fs to 1 ps. The length in the pulse changes how quickly the film responds when the pump and the probe have the same polarization. However, when the pump and probe are cross-polarized there is a ~ 100 fs feature that does not depend on the pulse length.	65
6.4	This graph shows the same feature on the film on a) VO ₂ /Al ₂ O ₃ and VO ₂ /TiO ₂ , with a Gaussian fit. While the fit for b) VO ₂ /TiO ₂ gives us a shorter δt , the fit does not account for the entire feature.	66
6.5	This graph shows the relationship between the intensity of the pump, and the depth of the sub-ps feature. a) Shows the measurement for three different fluences, and one can see a decrease in $\Delta R/R$ for the higher fluence. b) shows the peak of sub-ps feature as a relationship with the fluence.	67

6.6	The experimental set up we used for these measurements were much the same as the basic pump-probe measurements, except the sample was not mounted in a cryostat, and there is an electromagnet that creates a magnetic field parallel to the sample surface.	68
7.1	Relative change in reflectivity ($\Delta R/R$) for the VO ₂ film on (a) Al ₂ O ₃ substrate and (b) TiO ₂ substrate as a function of time after the MIT is induced at time $t = 0$ by a strong ultrafast pump pulse. The values of the pump fluence are shown in the legend, and the sample temperature is set to 311 K in (a) and 280 K in (b), which correspond to approximately 30 K below the critical temperature T_c for thermally-induced MIT for each sample.	73
7.2	Schematic of the experimental setup using a continuous-wave probe laser.	75
7.3	Dependence of metal state decay constant τ on the laser pump fluence and substrate temperature. Dots represent experimental data, and lines corresponds to the results of the theoretical calculations. The initial temperature T_s for both sample substrates was approximately 30 K below their respective MIT critical temperatures.	75
7.4	Evolution of the reflectivity across the thermally induced MIT for the case of sapphire and rutile substrates normalized to the average critical transition temperature. The open circles (red) correspond to the measured reflectivity in the heating branch, the solid circles (blue) correspond to the measured reflectivity in the cooling branch, and the solid curve corresponds to the theoretical result. For rutile substrate $\langle T_c \rangle = 314.0$ K, and for the sapphire substrate $\langle T_c \rangle = 340.1$ K.	78
7.5	(a) and (b) show the grain size distributions normalized to the average grain size for sapphire ($\langle D \rangle = 64.7$ nm) and rutile ($\langle D \rangle = 17.4$ nm) substrate respectively. (c) and (d) show the critical temperature distribution normalized to the average critical temperature for sapphire ($\langle T_c \rangle = 340.1$ K) and rutile ($\langle T_c \rangle = 314.0$ K) respectively. The bulk critical temperature is taken to be $T_c^{(bulk)} = 355$ K.	83
7.6	Evolution of the insulating partial volume η_I across the thermally induced MIT for case of (a) sapphire and (b) rutile substrates. For rutile, $\langle T_c \rangle = 314.0$ K, and for sapphire $\langle T_c \rangle = 340.1$ K.	84

7.7	Sketch of the heterostructure considered in this work. It is composed of a vanadium dioxide (VO_2) thin-film deposited on top of a substrate. The substrates considered in this work are titanium dioxide (TiO_2), and aluminum oxide (Al_2O_3). For VO_2/TiO_2 $d = 110$ nm while for $\text{VO}_2/\text{Al}_2\text{O}_3$ $d = 80$ nm. For both substrates, $L = 0.5$ mm.	84
7.8	Full numerical calculation of the dependence of metal state decay constant τ on σ_{T_c} for two different values of the sample average critical temperature $\langle T_c \rangle$, and $T_s(L) = 280$ K. The initial temperature $T_0 = 360$ K is such that the sample is initially fully metallic, and $(T_0 - \langle T_c \rangle)/(\sqrt{2}\sigma_{T_c}) \approx 9$	89
7.9	$\text{VO}_2/\text{Al}_2\text{O}_3$ metal state decay time τ dependence on the Kapitza constant σ_k for $\langle D \rangle = 64.7$ nm, $\sigma_D = 38.5$ nm, substrate temperature $T_s(L) = 310$ K, and fluence $\phi = 8$ mJ/cm ² . The red dots correspond to numerical calculations, and the dashed line is given by $\tau \propto \sigma_K^{-1}$	89
7.10	(a) Time evolution of reflectivity after the photo-induced MIT for VO_2/TiO_2 for three different $T_s(L)$ and $\phi = 9$ mJ/cm ² . The solid curves correspond to the theoretical results, and the dashed curves correspond to the experimental results. For the three theory curves we use $\sigma_K = 1100$ W/(K cm ²). Panel (b) shows the corresponding insulating fraction time evolution. . . .	92
7.11	Dependence of the VO_2/TiO_2 metal state decay time constant τ on σ_D for two values of $\langle \ln D \rangle$, as defined in Eq. (7.5), Kapitza constant $\sigma_K = 1100$ W/(K cm ²), substrate temperature $T_s(L) = 280$ K, and initial fluence $\phi = 9$ mJ/cm ²	93
7.12	$\text{VO}_2/\text{Al}_2\text{O}_3$ reflectivity time evolution after photo-induced MIT for $\phi = 7.5$ mJ/cm ² . The red dots correspond to the experimental result. The dotted curve correspond to the theory with $\sigma_K = 1100$ W/(K cm ²), and the solid curve corresponds to $\sigma_K = 13000$ W/(K cm ²).	93
7.13	Film and substrate temperature time evolution. For sapphire (a), $T_s(L) = 310$ K, and for rutile (b), $T_s(L) = 280$ K.	94
7.14	Dependence of metal state decay constant τ on fluence and substrate temperature for VO_2/TiO_2	95
8.1	(a) Schematics of the THz pump - optical probe experimental setup. (b) Optical probe reflection by the VO_2 film on a TiO_2 substrate and by the TiO_2 substrate only after interaction with the THz pump pulse.	98

8.2	a) shows the probe reflectivity response as the THz pump is attenuated. b) shows all the curves, normalized with respect to the max pump power of 100 kV/cm. Note that they all have the same rate of change over time before the change in reflection flattens out. This is different than the behavior of the film when pumped optically. c) and d) show the relationship between pump power and the resulting change in reflection for THz and 800 nm respectively.	100
8.3	Electric field temporal profiles (a) and spectra (b) for an attenuated broadband and spectrally filtered THz pump pulses. The sharp cut-off of the unfiltered THz pulse spectrum at 8 THz is due to detector response; actual pulse extends to 12 THz. (c) Recorded optical response of the VO ₂ film to these THz pump pulses.	103

STUDY OF VARIATIONS OF THE DYNAMICS OF THE METAL-INSULATOR
TRANSITION OF THIN FILMS OF VANADIUM DIOXIDE WITH AN ULTRA-FAST
LASER

CHAPTER 1

Motivation for studying VO₂

Vanadium is a transition metal with its valence electrons in the d band. The overlap between d orbitals in transition metals tend to be small, leading to narrow bands, further narrowed in oxides by hybridization with the oxygen ions. These narrow bands, along with large band gaps, mean that the system cannot be accurately modeled by assuming that there is a delocalized electronic gas. The localization and coulomb repulsion makes the electron-electron interaction important to the behavior in the system. This leads to useful and interesting properties in transition metal oxides such as VO₂, and also high T_c superconductors, Mott insulators, and insulator-metal transitions.

This phase transition in VO₂ is interesting on many levels. It makes this material attractive for novel technologies such as ultrafast switches, plasmonic sensors, and smart window coatings.[5, 6] In addition, despite VO₂ being studied for decades, there is still disagreement on what mechanism drives the transition. [7, 8, 9, 10, 11, 12, 11, 13, 14]

One of the reasons that VO₂ has had so much attention compared to other materials that display a insulator-metal transition is the fact that the transition happens right above room temperature at 340 K (68° C)[7, 15]. This is an easily accessible temperature for

experimenters. Other similar materials that have an insulator-metal transition have a T_c that is either accessible at lower temperature requiring a cryostat, like V_2O_3 which has a T_c at 150 K [16], or happens at a temperatures difficult to achieve in the lab, like NbO_2 which has a T_c at 1082 K [17]. This convenient T_c also makes VO_2 an attractive material to implement in new technologies. There is a large change in conductivity that can happen on a femtosecond timescale when light-induced with an optimal light frequency ($\sim 800nm$), faster than most electronic systems can respond. VO_2 could be used for ultrafast switches, in both electronic and plasmonic systems. It has also been proposed that it could be used as a coating for smart windows that would automatically change how much inferred radiation is reflected depending on the temperature, making buildings more energy efficient. [5]

Implementation of such VO_2 -based new technologies requires the ability to tailor the MIT properties to the demands of the particular application. For example, several studies demonstrated that the critical temperature of a thermally-induced MIT can be adjusted by doping VO_2 films, or by applying pressure along the rutile c-axis.[18, 19, 20]. When using VO_2 in these applications, it is typically in the form of a nanocrystal or thin film. While bulk VO_2 cracks and deforms under the strain of the transition, nanoscale VO_2 can go through the insulator-metal transition without significant damage. Thin films also have reversible transitions, and the properties of the insulator-metal transition can be tuned by changing the strain and defects in the film[21, 22, 23, 24, 25]. We also find that films with different micro-structures exhibit different dynamics when optically pumped, both in transitioning to the metallic state, and recovering back to the insulating state.

In this work, I first introduce the background on the current understanding of the insulator-metal transition in VO_2 in Chapter 2, including the previous work that has been done with ultrafast studies. In Chapter 3 I go over the characterization of our samples. This includes measurements done with continuous wave lasers while heating the films through the transition, dc-conductivity measurements with four-point probe, ellipsometry,

and Raman spectroscopy measurements.

Chapter 4 then describes the pump-probe experimental set-up, which is the primary experimental method used in this work. This covers the laser system used, the characterization of the pulses, and the cryostat system used for cooling the samples. Chapter 5 discusses the work we did mapping out the response of the VO_2 thin films, varying the pump fluence and the initial temperature of the thin films. Then in Chapter 6 I show some interesting measurements looking at the sub-picosecond response in the films when we change the duration of the pump and probe pulse. The following chapter, Chapter 7 looks at the recovery times back to the insulating state once the films have been optically pumped. Finally, Chapter 8 covers the experiments performed at RPI with Dr. Yamaguchi's group, pumping with a broad-band THz pump, instead of an optical pump.

CHAPTER 2

Background on Insulator-Metal Transition in VO_2

2.1 Phases of VO_2

Vanadium Dioxide is a highly correlated material that undergoes an insulator-metal transition when heated. At low temperatures the material is an insulator (or semiconductor), and when it is heated past the critical temperature T_c the dc conductivity increases by five-six orders of magnitude [7]. This is an easily accessible transition temperature, making VO_2 a popular material to study. In addition, the optical properties change as well, most dramatically in the infrared range.

VO_2 has four different phases currently known. At high temperatures, above a critical temperature $T_c=340$ K (for bulk VO_2), vanadium dioxide has a tetragonal/rutile lattice structure, with lattice constants of $a_r=4.55$ Å and $c_r=2.85$ Å. This is known as R- VO_2 and is the metallic phase. There is the low temperature M1 phase (referred to here as M- VO_2), where the lattice structure is monoclinic. In this phase, the lattice breaks symmetry,

and the vanadium ions pair up and tilt off the c_r axis with the oxygen ions still in a octahedra around the V^{+4} ions. The monoclinic lattice constants are $a_m \approx 2c_r$, $b_m \approx a_r$, and $c_m \approx a_r - c_r$ ($a_m = 5.70 \text{ \AA}$ $b_m = 4.55 \text{ \AA}$ $c_m = 5.37 \text{ \AA}$)[7]. Figure 2.1 shows both the change in symmetry and shift in band structure in VO_2 .

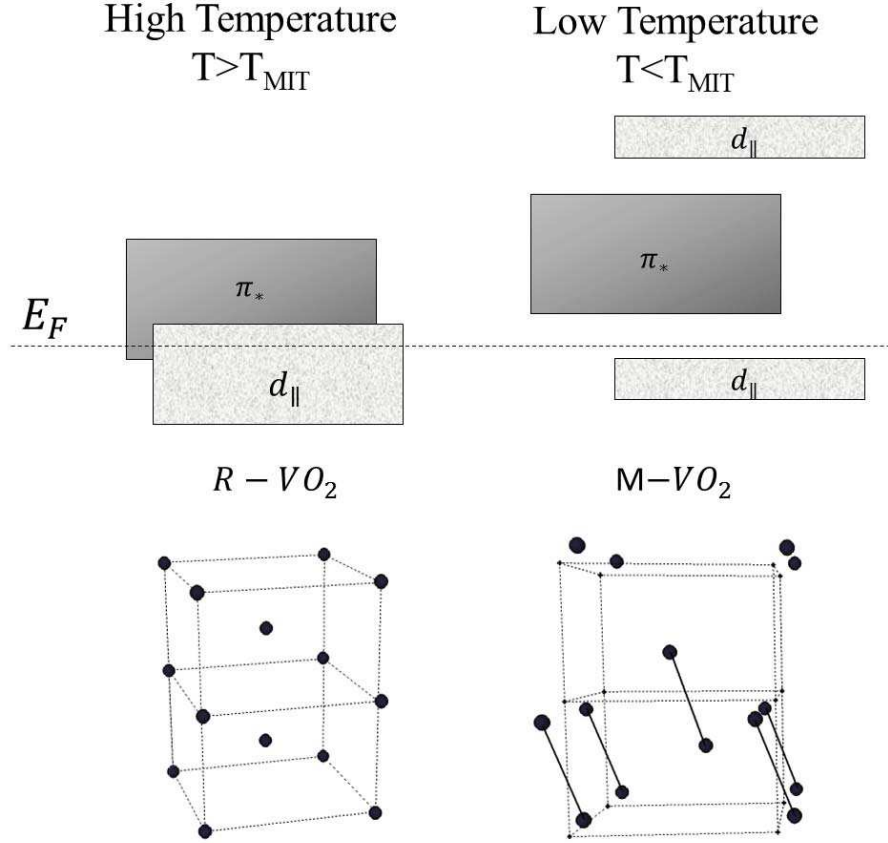


FIG. 2.1: Schematics of the VO_2 lattice structure and electron energy band structure below and above the critical MIT temperature. High-temperature metallic phase corresponds to the tetragonal (or rutile) lattice structure. Upon cooling through the thermally induced phase transition the V^{4+} ions dimerize along the c -axis of the tetragonal phase, breaking the symmetry and forming monoclinic lattice cells. At the same time the d band splits into two different bands, while the π^* band shifts above the Fermi level E_F , drastically decreasing electron conductivity.[1]

When VO_2 is placed under pressure, two other phases emerge. M2 is similar to M1 in that the Vanadium ions pair up and dimerize, but the V^{+4} pairs do not twist off-axis,

and only every other row dimerizes. There is also a triclinic T phase which is intermediate between M1 and M2.[2, 26] However, neither of these phases appear in our films, and are not relevant to this work.

Along with the change in lattice structure, there is a large shift in the electronic bands, changing it from a poor insulator to a dirty metal. Unfortunately, the band structure in VO₂ is difficult to qualitatively calculate from first principles, leading to continued debate as to what is the primary transition mechanism, as discussed in the following section. [7, 8, 9, 10, 11, 12, 11, 13, 14]

2.2 Band Theory

Modeling crystalline highly correlated systems from first principles is a difficult task. A Hamiltonian that accounts for all the coulomb potentials between all the ions and all the electrons in the system becomes prohibitively complicated to compute.

$$\hat{H} = \hat{H}_{ion} + \hat{H}_{electrons} \quad (2.1)$$

If \hat{H} is the Hamiltonian for an electron in a crystalline lattice, H_{ion} can be simplified as a periodic potential; that still leaves all the electron-electron interactions which are too computationally costly to compute.

The most naive way of simplifying the problem is to use the Free-electron model, which makes a good approximation for crystalline metals[27], particularly in calculating conductivity. We assume that the ions in the background are smeared out to be a constant positive background, and the electrons behave as a gas. From the resulting electron density, one can calculate what the plasmon frequencies are, and what electromagnetic wavelengths are absorbed or reflected in metals.

This a useful, but highly simplistic model, and does not explain why some materials

are insulators and some are metals/semiconductors. In order to provide a more complete description of insulators and semi-conductors, we can use band theory. In band theory we take advantage of the periodicity of the lattice.[27]

$$H = \frac{-\hbar^2 \nabla^2}{2m} + U(\vec{r}) \quad (2.2)$$

where $U(\vec{r})$ is periodic and has the property of $U(\vec{r} + \vec{R}) = U(\vec{r})$. This periodicity of the lattice results in the electrons having energy bands, separated by the forbidden energy regions, or gaps. We can then fill the lattice with many electrons (assuming that there is no interaction between them) and Pauli's exclusion principle mandates how the electrons must fill these energy bands. If the Fermi level lies within a band then, the material is metallic, since it is easy for the electrons with the highest energy to be excited enough to be mobile. If the Fermi level lies within a band gap, however, then there is a much higher energy cost to excite the electrons to be mobile, and the material is considered to be an insulator. Semiconductors have the Fermi level within a gap, but the gap is small enough that good electrical conductivity is not as difficult to achieve as for an insulator. [27]

Because we are assuming the electrons are not interacting, this is still a simplistic model, but it is still effective for many materials. However, transition metals, with partially filled d orbitals, behave like insulators, even though traditional band theory would predict that they should be metallic.[2] Pierls was the first to suggest that electron-electron correlations play an important role in these insulators. It was Mott, however, that proposed a model for 'Mott insulators'[2]. He described a 1D lattice where each electron sits on a lattice site, and if you ignore Coulomb forces, a band fills when there are two electrons at each site (one spin up the other spin down). But if the electrons interact strongly, then any second electron at a lattice site feels a repulsion from the first electrons, and the

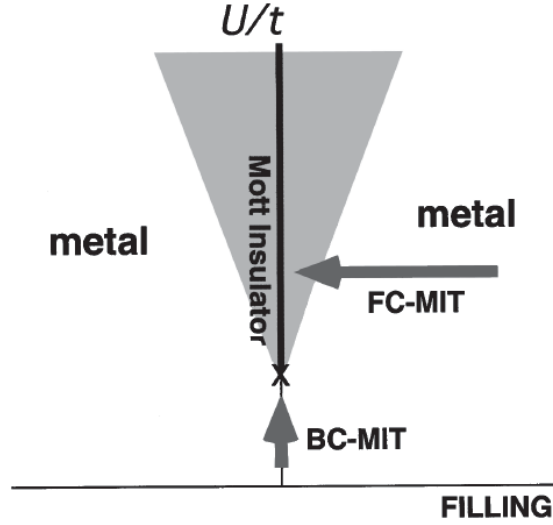


FIG. 2.2: Here is a graph based on the Hubbard model, showing two avenues that a material could go through a insulator-metal transition. The band-controlled model changes the relationship between U and t , creating localization do to the energy cost of moving electrons. The filling controlled model changes the number of electrons in a band, which makes U play a larger role in increasing the energy cost of moving electrons within the lattice[2]

energy cost of placing such electron there is higher. This leads to a splitting of the band, and the lower energy band is now full when each lattice site has an electron.

Some of these Mott insulators can transition into a metallic phase. Figure 2.2 shows two paths along which a metal-insulator transition can happen based on the Hubbard model, where electron behavior is dependent on U , the energy cost of placing an electron at a lattice site, and t , the transfer energy it takes to transfer an electron from one site to another [27]. One path to MIT is filling controlled, where fewer electrons inhabit the valence band, and the importance of U goes down. In band-controlled MIT, the filling of the bands stays the same, but the band structure changes. [2]

2.3 Insulator-Metal transition in VO₂

VO₂ is a transition metal oxide, and like many other transition metal oxides, is a highly correlated material. Theorists are still working to quantitatively model the phase transition, but have encountered difficulties coming up with a first principles model that both works for the low temperature insulating monoclinic phase as well as the high temperature metallic phase. Goodenough in the sixties made a calculation of the band structure in both insulating and metallic phases, based on spectroscopic data.[1] There are two bands that fall on the Fermi level, as can be seen in figure 2.1. One is the $d_{||}$ orbitals from the VO₂ orbitals, the other is the π^* , which comes from the hybridization with the oxygen ions.

What makes VO₂ more complicated than other materials that go through an insulator-metal transition is that there are two mechanisms at play. At low temperatures the $d_{||}$ band splits, with one below the fermi level and one above. At higher temperatures the bands collapse, making VO₂ metallic. There is also a shift in the π^* band which lowers it to the Fermi level. However, this band collapse is accompanied by the crystalline lattice changing to the higher symmetry tetragonal phase. The V⁺⁴ ions are no longer dimerized, which changes the shielding of the valence electrons, and affects the electron-correlation, as well as shifts the overall energy of the bands in a Peierls type transition [2]. The question, which researchers have been struggling with since VO₂ was discovered, is which mechanism is the primary driver of the insulator-metal transition. While a complete description of the transition mechanism has not yet been achieved, it is generally accepted that the MIT in VO₂ is due to the interplay of a Mott-Hubbard electronic instability in which the electron-electron interactions play the critical role, and a Peierls instability of the lattice.[12, 11, 13, 14, 28, 29] There are several different ways researchers induce the transition, attempting to elucidate which is the path followed during the IMT. There is heating, as well as voltage application, doping, pressure, and optically pumping the

material[7, 11, 26, 8, 30]. One promising avenue of study, which our experiments are based on, is looking at time resolved optically pumped measurements.

2.4 Optical properties of VO₂

While the dc conductivity has a dramatic increase across T_c during the thermally induced IMT, if we probe with other parts of the electromagnetic spectrum, the contrast in the probe signal across the transition is smaller, depending on the susceptibility at this wavelength. This can be seen if we look at the data from Ref. [3], as shown in figure 2.3. These graphs show the real and imaginary parts of the dielectric constant ϵ from 0.5 eV to 2.5 eV (2500 nm to 500 nm), where a) and b) are for VO₂ below 355 K and c) and d) are VO₂ above 355 K. For a non-magnetic material (like VO₂), where $\mu_o = 1$, we can calculate the complex index of refraction n^* from ϵ :

$$n^* = \sqrt{\epsilon} \quad (2.3)$$

that defines how light is transmitted and reflected in a material. $\text{Im}(\epsilon^*)$ tells us how much light will be absorbed. We can see that visible light (1.0 eV - 0.5 eV) does not change much as the film is heated up, which is consistent with the fact that we don't see much change in transmission and reflection when we heat our films through the transition.

In the IR regime, there is a much stronger optical response. The $\text{Im}(\epsilon)$ increases greatly below 1.0 eV, becoming more metallic, and VO₂ becomes more reflective at those wavelengths. At 1.5 eV (800 nm) where most of our measurements are taken, we actually see a drop in reflectivity as well as a slight drop in transmission, as the film absorbs strongly at that wavelength.

In bulk VO₂, both the M-VO₂ and R-VO₂ are anisotropic, as shown in figure 2.3. When thin films have multiple orientations within the film, this washes out the anisotropy,

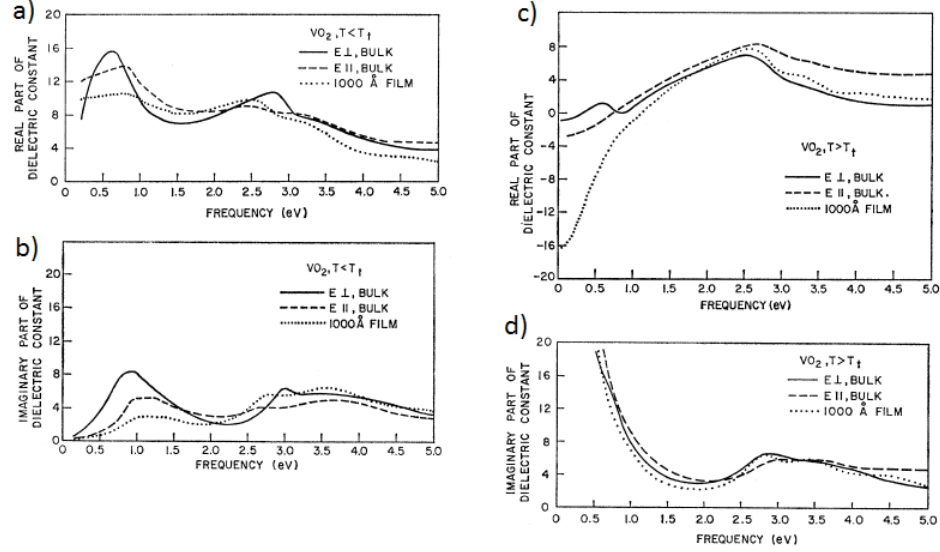


FIG. 2.3: Measured complex dielectric constants for VO_2 , both in bulk and for a 1000 Å film on Al_2O_3 . a) is the real part of ϵ , and b) is the imaginary part at room temperature, and c) and d) show the same for the material heated up to 355 K. From Ref. [3].

as can be seen with Verleur et al.'s 100 nm VO_2 thin film measurements. For our samples, only the one that is monocrystalline shows any sign of anisotropy, as described in Chapter 4.

2.5 Ultrafast studies of VO_2

With the advent of ultrafast lasers, a new avenue of study of the insulator-metal transition in VO_2 was enabled.[31] With the development of laser pulses in the femtosecond scale, there was soon an interest in looking at the time dynamics of the VO_2 metal-insulator transition. The hope was to separate the response of the lattice from the faster electronic response. Sufficiently short light pulses can photoexcite the electrons in a material before the lattice has time to respond. By picking a photon energy that is sufficient to photoexcite the electrons above the band gap, it is possible to quickly induce the transition.[32]

Because the debate about the primary mechanism of the VO_2 phase transition is

between a Peierls type transition and a Mott type transition, one of the ways that ultrafast studies can contribute to the debate is to look at the rate of change in transition. Electrons can respond on a sub-femtosecond scale, so electronic responses in the film happens within femtoseconds of the pump pulse hitting the sample, while the lattice takes picoseconds to respond. The time it takes for the excited electrons to transfer energy to the lattice takes on the order of tens of picoseconds.[9]

The first pump-probe studies were unable to measure the limit of the switching time [33, 31] due to the limit in pulse durations available. Only when lasers were able to get down to the femtosecond regime could experimentalists resolve how fast the insulator-metal transition could happen. Cavalleri et al. found by varying the duration of the pump pulse that the transition has a bottleneck of 80 fs.[32] 80 fs is half a period of the 5-6 THz Ag modes that are believed to play a prominent role in the phase transition, since they map the M-VO₂ lattice structure to the tetragonal R-VO₂ lattice.

Hilton et al. showed [9] that the threshold power changes when the sample is heated closer to the transition temperature, with less energy needed to induce the transition due to the softening of the lattice. Cocker et al.[12] expand upon this further by mapping out the threshold fluence for the VO₂ transition at a temperature range of 17-350 K. They find four different distinct behaviors in the dynamics of the insulator-metal transition. I discuss this in further detail in Chapter 5, as my experimental results closely followed their process.

2.6 Microstructure effects on IMT

The difficulty and advantage of working with thin films is the variability in bulk properties that arises from the strain and grain boundaries[34, 35, 36, 37, 38]. Bulk VO₂ has a very well defined transition temperature at 340 K, with a small hysteresis, although the insulator-metal transition is not repeatable due to the strain on the lattice cracking and

deforming the material as it goes past T_c . Small nanocrystals of VO_2 also exhibit transition temperatures close to bulk, repeatably since the smaller crystals have more surface area to accommodate for lattice transformations.[39] Studies have shown that it is possible to shift the T_c of these VO_2 nano crystals by applying pressure along the c_R axis, as well as transitioning the material to the M2 and T phases.[26]

This shifting in T_c also happens with highly strained thin films. Compressive strain along c_R reduces T_c , while expansive strain pushes the transition closer to the bulk T_c . [40]

CHAPTER 3

Characterization of heat induced IMT in thin films

3.1 Description of samples

All the samples we have used for these experiments were grown at the University of Virginia. [20, 41] They were grown on crystalline substrates by Reactive Biased Sputter deposition. We received films grown on (001) SiO_2 , c-cut (0001) Al_2O_3 , and one on (001) TiO_2 . Because of the similarity of the insulator-metal transition for the VO_2 films on Al_2O_3 and on SiO_2 , most of the work here focuses on the difference between the films on TiO_2 and Al_2O_3 . Figure 3.1 displays a photograph of the VO_2 films on the various substrates, and figure 3.2 has the AFM images taken at UVA, showing the different grain sizes for the different samples.

We were given a series of film thicknesses grown on Al_2O_3 ranging from 50 nm to 100 nm. The film grown on SiO_2 is 80 nm and the film grown on TiO_2 is 110 nm.

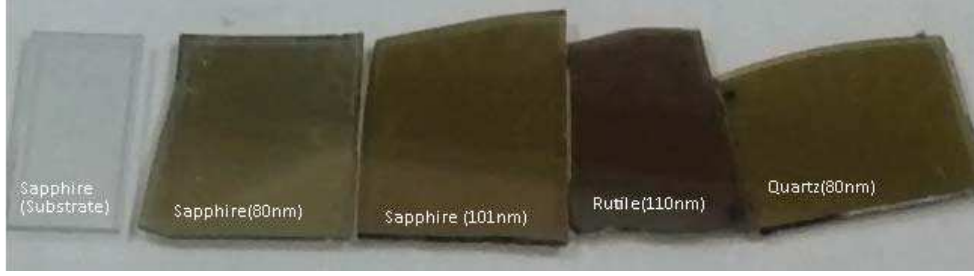


FIG. 3.1: Here is a picture of the various VO_2 thin film samples used in these studies.

3.2 Continuous Wave Reflection and Transmission measurements

The primary property we have used to characterize the insulator-metal transition in our VO_2 thin film samples was their reflectivity. We have also looked at the phase transition by measuring the DC conductivity with a four-point probe, and measuring the Raman peaks with a Raman spectrometer.

We measured the DC conductivity by applying a 4-point probe technique and found the DC conductivity of VO_2 films on Al_2O_3 at 370 K to be $2.24 \times 10^5 \text{ S/m}$, while the DC conductivity of VO_2 films on TiO_2 at 340 K was found to be $3.03 \times 10^5 \text{ S/m}$. At 297 K the DC conductivity is $1.71 \times 10^2 \text{ S/m}$ for VO_2 on Al_2O_3 and $7.01 \times 10^3 \text{ S/m}$ for VO_2 on TiO_2 .

3.3 X-Ray Diffraction

An important technique that we used to characterize the thin film samples was X-Ray diffraction (XRD). XRD is an essential technique to determine the crystallinity, thickness, and strain in our films. In a crystal, periodicity in the lattice creates reflectivity maxima when x-rays reflecting off the planes of a lattice have a path length that leads to constructive interference between atomic layers. Depending on the symmetry of the crystal, each

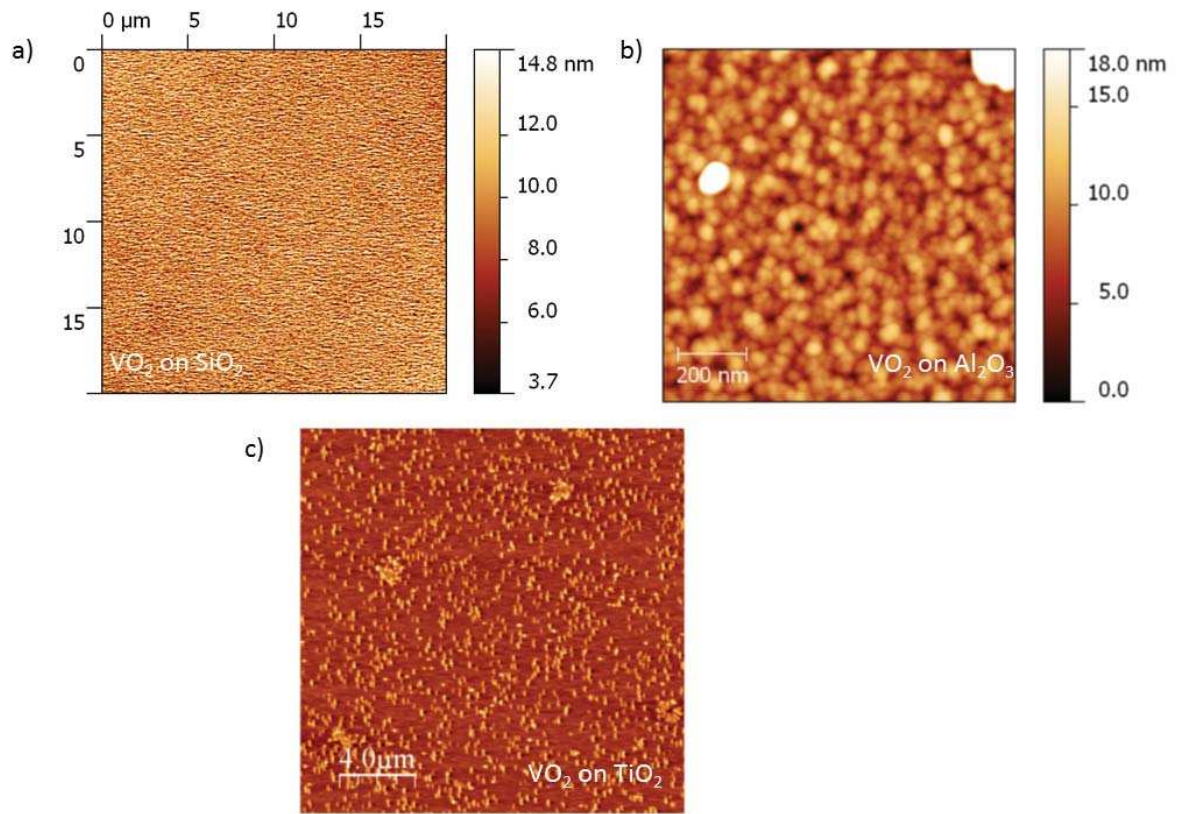


FIG. 3.2: Atomic force microscopy images of our samples taken at UVA.

material has an individual XRD fingerprint, which allows us to identify what is contained in the sample. XRD is an important tool for determining if our films are really VO_2 and not some other Vanadium oxide. It also give us a wealth of additional information: such as the orientation and thickness of the films, whether the films are mono-crystalline or polycrystalline, the size of the grains, and the strain due to mismatch with the substrate. These characteristics can affect the properties of the insulator-metal transition, and are considered in our analysis for the experiments in this work.

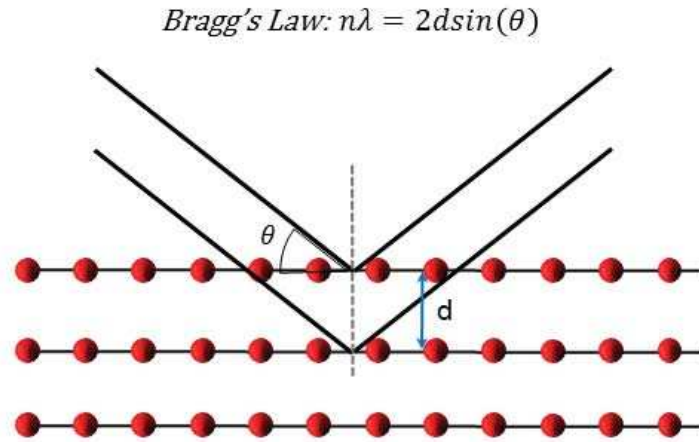


FIG. 3.3: X-ray diffraction uses the interference between layers in a crystalline material. The x-rays constructively interfere when Bragg's Law (as shown above) is satisfied. By scanning over θ we can find for what angles there is a diffraction point, and from there calculate d .

Figure 3.3 shows the basic principle behind XRD. Since x-rays are on the same length scale as lattice spacings in crystals, we can use the interference between layers to calculate the distance between planes using Bragg's Law. When using an X-ray source with a fixed wavelength, one must consider the geometry of the x-ray source and the detector. Each set

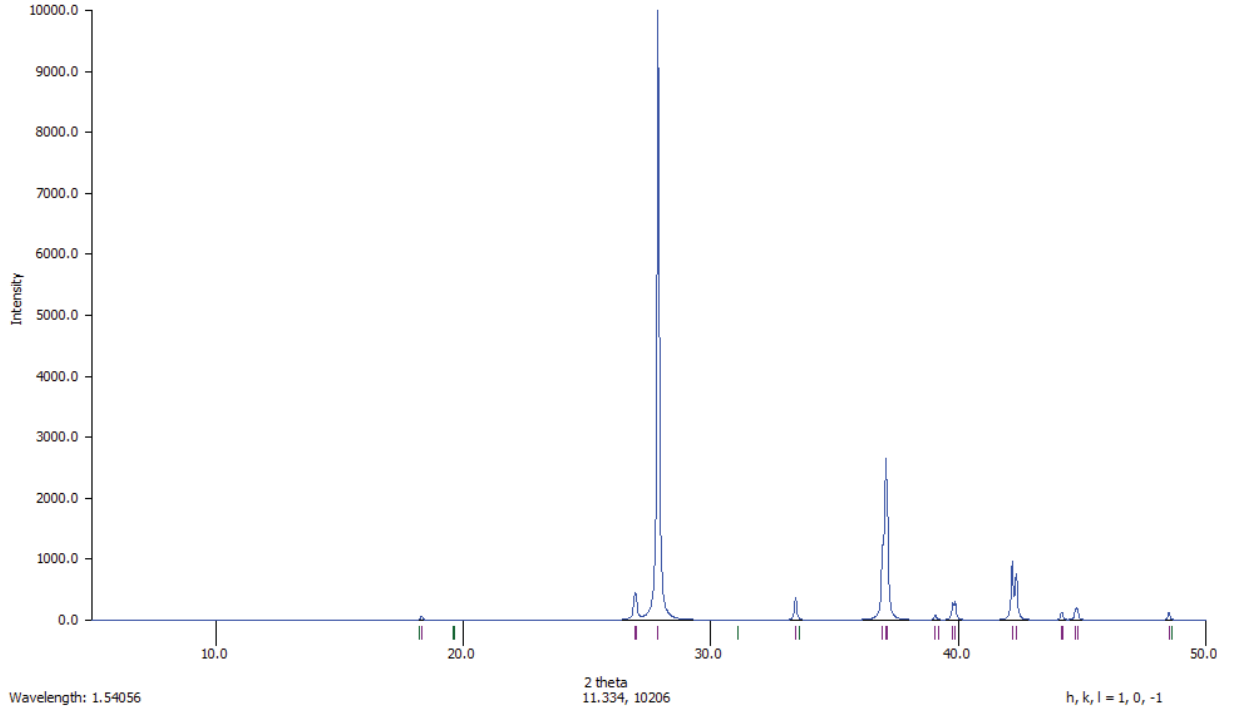


FIG. 3.4: This is a calculated powder XRD pattern of M1-VO₂. The peaks we see in our $\theta - 2\theta$ measurements are consistent with the peaks seen here.[4]

of planes constructively interfere at a specific angle, so in order to get a complete picture of the crystal one must measure over all the incident angles ($\theta - 2\theta$). If a sample is powdered, the XRD measurement contains all possible XRD peaks due to all orientations since there are many different nanocrystals in different orientations. Figure 3.4 displays a calculated powder XRD spectrum for M-VO₂. In epitaxial thin films, the peaks that one can see over a 2θ scan depend on the orientation of the film. This requires us to rotate the film to different orientations to scan different peaks. Figure 3.5 shows how the sample stage can rotate. Tilting the stage about χ lets us access crystalline planes of different orientations. Scanning about ϕ tells us if there is more than one crystalline orientation present within the films. If there are more than one set of peaks when we scan about ϕ , other than the allowed multiples of the main orientation, then there was more than one preferred grain orientation when the film was grown on the substrate.

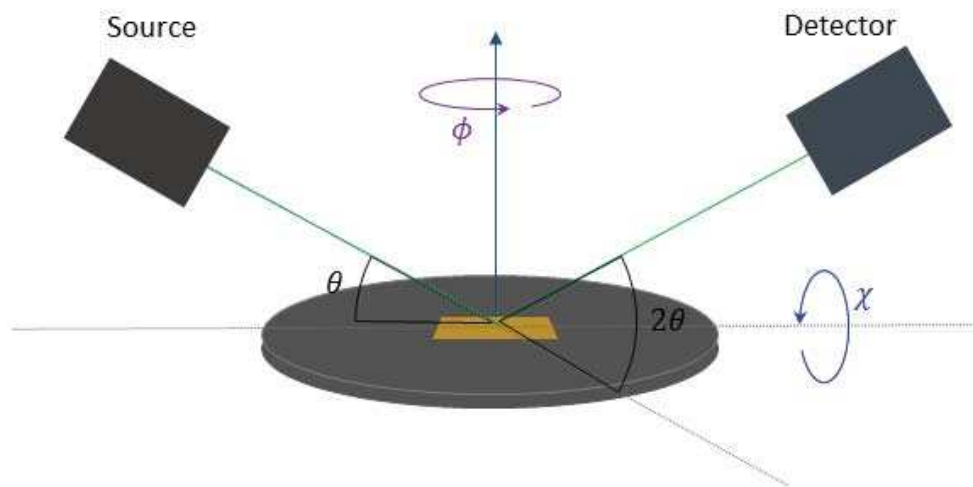


FIG. 3.5: In order to access different family of planes within a thin film sample, it is necessary to rotate the stage. $\theta - 2\theta$ scans are when the source and detector move to change the incident angle of the x-ray beam. ϕ rotates the stage about the normal of the sample surface. χ tilts the stage, rotating the sample's normal with respect to the incident beam.

A cathode ray tube provides the source of the x-rays with a wavelength corresponding to Cu K- α , which has a wavelength of 1.54 Å. We used a commercial system Empyrean from Paralytical, which is particularly well suited to measure XRD of thin films, due to its 4-circles goniometer.

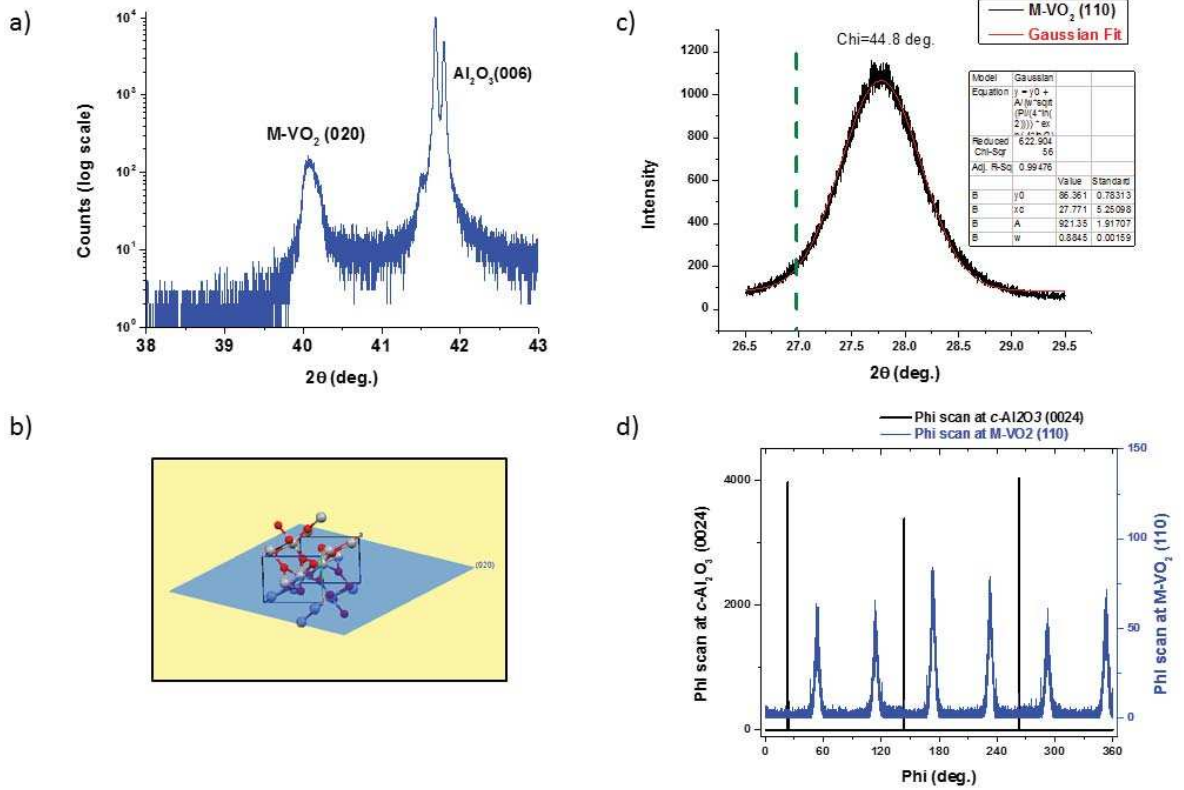


FIG. 3.6: Here is the XRD data from VO₂ on Al₂O₃. a) shows the $\theta - 2\theta$ curve, which shows the strong substrate signal and the weaker VO₂ peak. Because the x-ray source has both Cu K- α 1 and K- α 2, the narrower substrate peak is narrow enough to resolve both wavelengths. b) is a depiction of the (020) plane in M-VO₂. c) is an asymmetric $\theta - 2\theta$ scan at $\chi = 44.8^\circ$ of the M-VO₂ plane (011). d) shows the ϕ -scan at $\chi = 44.8^\circ$, showing 3-fold symmetry.

Figure 3.6 shows the XRD measurements for the 80 nm VO₂ film on Al₂O₃ (thickness was measured at low angle measurements). We identify the substrate peak as being the strong signal on the right in figure 3.6 a), and a single peak from the film. This peak corresponds to the (020) M-VO₂ plane. As this is the only peak from the film for the

symmetric scan, we can infer there is only one crystal orientation out of plane.

From the asymmetric scan in figure 3.6 c) we identified the M-VO₂ (110) peak at $\chi = 44.8^\circ$. The ϕ scan shows six peaks from the film, which corresponds to a 3-fold symmetry in the film. This makes sense when we consider how M-VO₂ would map onto the substrate. The substrate is c-cut Al₂O₃ which is trigonal and looks like an array of hexagons from top view. Since the angle between c_m and a_m in M-VO₂ is $\gamma = 123^\circ$ [7], it would naturally deposit on the substrate in 3 possible orientations, with (020) pointing up. This film is crystalline, and from the shift of the peak relative to the bulk peak position, it has an in-plane strain of -0.53% and an out of plane strain of -2.81%.

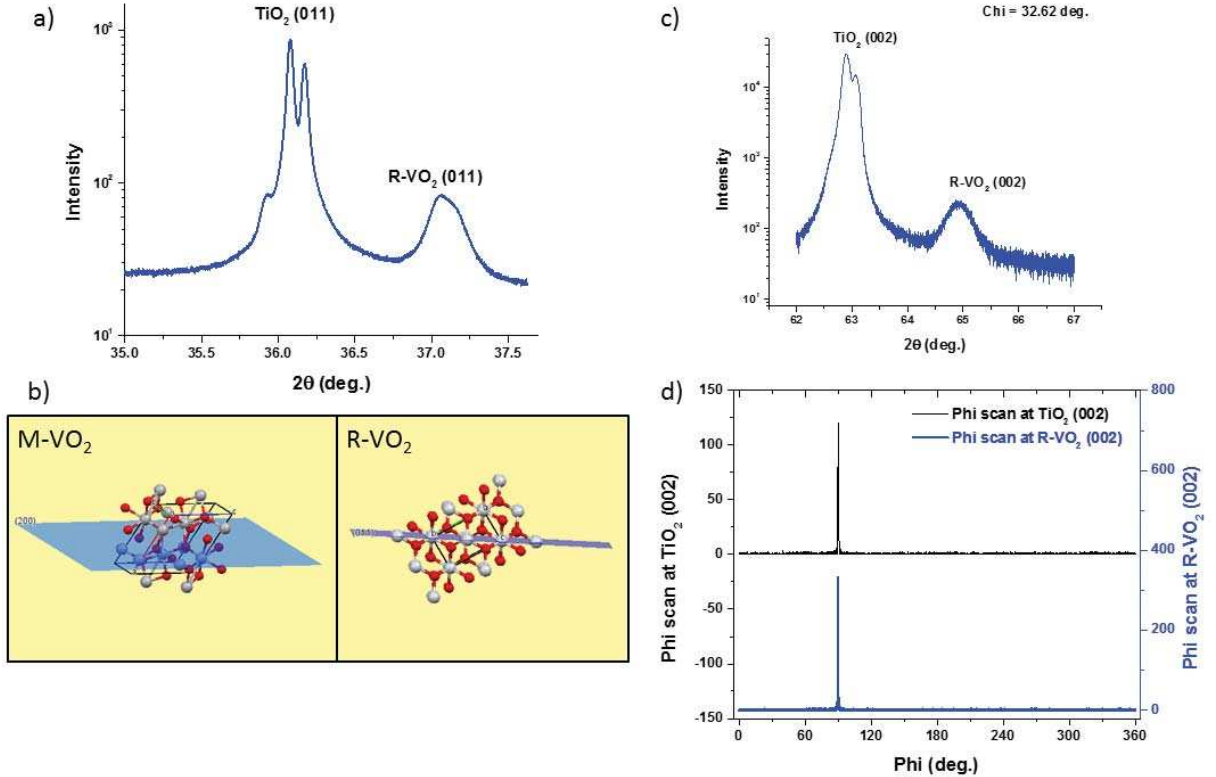


FIG. 3.7: Here is the XRD data from VO₂ on TiO₂. a) shows the $\theta - 2\theta$ curve, which shows the strong substrate signal and the weaker (011) R-VO₂ peak. b) depicts how the film lattice would be oriented in either phase. c) show the asymmetric (110) M-VO₂ scan, and d) shows us a ϕ -scan with tetragonal symmetry, indicating there is clamping of the film by the substrate.

Figure 3.7 a) shows the symmetric $\theta - 2\theta$ scan for the 100 nm VO_2 film on TiO_2 . The TiO_2 (011) substrate is tetragonal, like R- VO_2 phase, so it is a natural material to grow VO_2 films on. The symmetric $\theta - 2\theta$ scan gives us a film peak at 37.1° . This could correspond to either M- VO_2 (200) or R- VO_2 (011). As shown in figure 3.7 b), those planes represent the two different phases in the same orientation. The ϕ scan shows a single peak, which tells us there is a single crystalline orientation and the film is truly mono-crystalline. The strain out of plane is 0.14% and in plane is 0.53%.

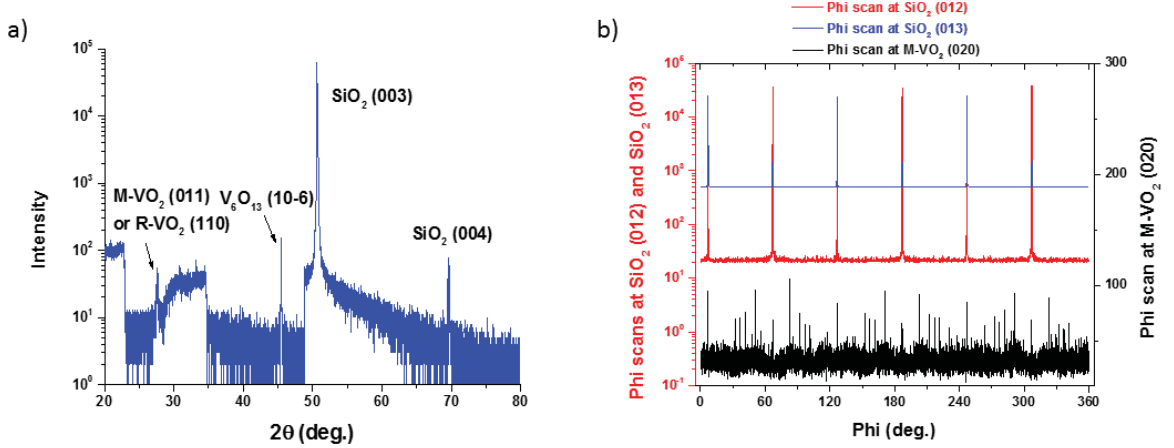


FIG. 3.8: Here is the XRD data from VO_2 on SiO_2 . a) shows the $\theta - 2\theta$ curve, which shows the strong substrate signal and the weaker (011) M- VO_2 peak. There are no peaks from the film in the ϕ -scan, indicating the film is polycrystalline.

The XRD scans for VO_2 on SiO_2 shown in figure 3.8 show a single M- VO_2 peak at $2\theta = 27.61^\circ$. There is another peak at $\sim 45^\circ$, but that is associated with another oxide, which means this film is not as pure as the others. But it does exhibit a single orientation out of plane. The figure 3.8 b) shows a ϕ scan which is different from the ones for the previous two samples. There are not clear peaks, meaning there is no preferred orientation when the film was grown on the substrate and is polycrystalline. There is an out of plane strain of 0.92%.

3.3.1 Grain size

The width of the film's x-ray peaks in figures 3.6-3.8 can also tell us about the average grain size. The relationship between the peak width is defined by the Scherrer equation [42]:

$$B_{crystal} = \frac{k\lambda}{L\cos\theta} \quad (3.1)$$

where $B_{crystal}$ is the full width of the XRD peak, k is a constant based on the shape of the grains in the film, L is the average grain size and θ is the Bragg angle. For the films grown on Al_2O_3 , TiO_2 , and SiO_2 we find an average grain size of 65 nm for $\text{VO}_2/\text{Al}_2\text{O}_3$, 12 nm for VO_2/TiO_2 , and 20 nm for VO_2/SiO_2 .

3.4 Continuous Wave Measurements

When a material's dc conductivity changes, the optical properties change as well, since light is an electromagnetic wave, and is sensitive to such changes. The susceptibility of a film depends on its band structure.

Figure 3.9 shows the IMT measured with several different wavelengths, in both absolute transmission and reflection. In visible range the changes in transmission and reflection across the transition is $\langle 5\%$ until we get to 800 nm, where the absorption increases through the transition. In figure 3.9 we can see that the sensitivity of the transition has a dependence on the incident beam's wavelength (λ). The reflection and transmission do not change much with the insulator-metal transition in the visible light regime, as indicated by the dielectric constant in figure 2.3. At longer wavelengths, starting at 800 nm we see a large amount of absorption, as both transmission and reflection drop as the film goes through the transition. At 1520 nm we see the most profound transition, with a 10% increase in reflection and a 23% drop in transmission, again consistent with ϵ measured

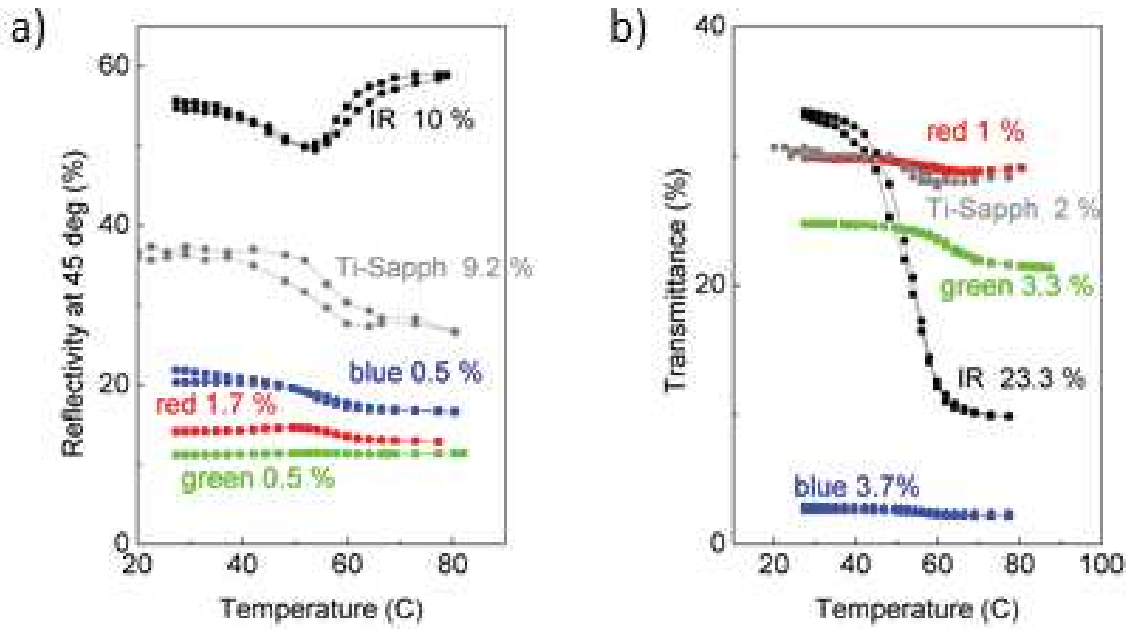


FIG. 3.9: Here are measurements taken by Cesar Clavero and Irina Novikova looking at the reflection (a)) and transmission (b)) for VO₂ on Al₂O₃. As we move from visible light into the infrared regime, the response becomes more dramatic for both transmission and reflection.

previously [3]. This is why VO₂ has been proposed as a candidate for a coating for smart windows. Because the reduction of infrared transmission is so much more than for visible light, one can reduce IR radiation from the sun without darkening too much at the visible ranges.

Our cw measurements were primarily with 800 nm, as this is the wavelength of our ultrafast pulses, and approximately 25% of the incident light is reflected by the film at near normal incidence. The experimental set up, as shown in figure 3.10, is a simple reflectivity and transmission measurement. The beam is reflected off the surface of the VO₂ sample, and both transmission and reflection can be measured as the film is heated through the transition. The change in transmission is detectable, but the change in ΔR is much larger,

so we used reflection for our probe. A half-wave plate allowed us to look for anisotropy in the transition by changing the polarization of the incident beam. Films were mounted on a Peltier heater stage that allowed us to control the temperature of the films. The temperature was monitored with a 10 k Ω thermistor and controlled with a TEC controller from Thorlabs.

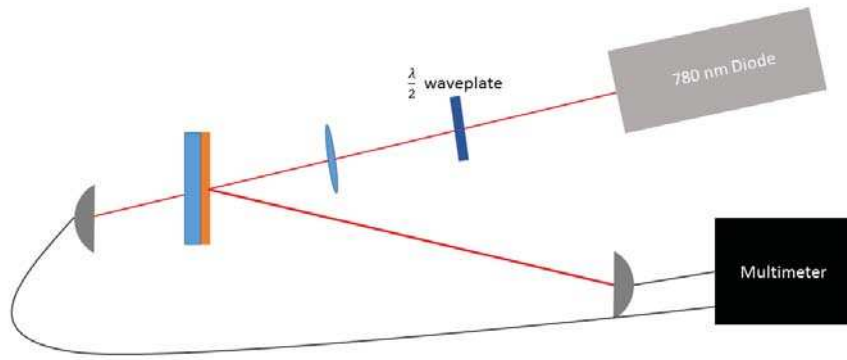


FIG. 3.10: The experimental set up of our continuous wave measurements. Beam was focused on sample, and the polarization of the incident beam was controlled with a half-wave plate. Films were mounted on a peltier heater allowing us to control the temperature. We looked at both transmission and reflection measurements.

Figure 3.11 shows the change in reflection as we heat VO₂ through the insulator metal transition for the 100 nm thick samples on Al₂O₃, TiO₂, and the 80 nm thick sample on SiO₂. The reflection is normalized with respect to the intensity of the reflection at room temperature. It is clear that the different films have noticeable differences in their transitions. The transition temperature (T_c) of VO₂ on TiO₂ at 310 K is much lower than the T_c of VO₂ on Al₂O₃ or SiO₂. The T_c for VO₂ on Al₂O₃ is much closer to bulk at 340 K, and for VO₂ on SiO₂ the phase transition is in between at T_c =326 K. The width of the transitions (the difference in temperature between heating and cooling the sample)

are quite different for these samples as well, 26 K ($\text{VO}_2/\text{Al}_2\text{O}_3$), 9 K (VO_2/TiO_2), and 15 K (VO_2/SiO_2).

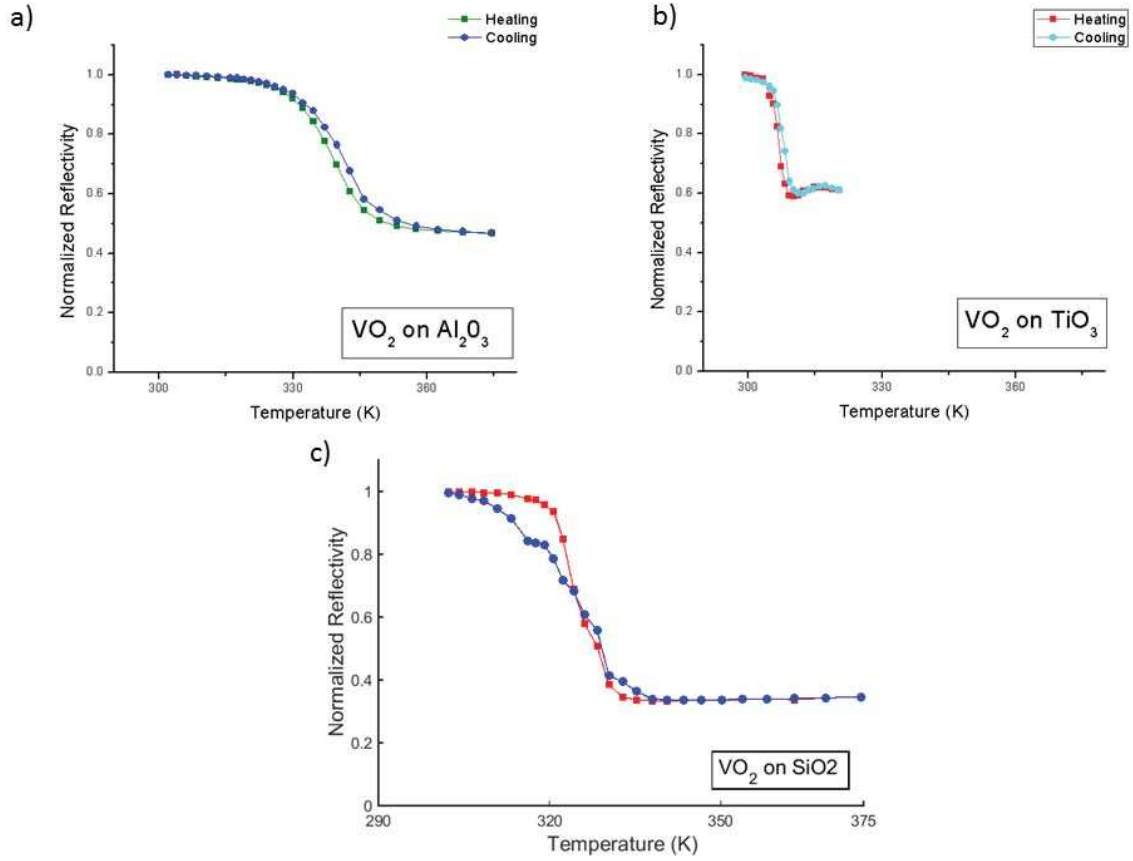


FIG. 3.11: Here are continuous wave measurements of the reflection off of VO_2 on a) Al_2O_3 , b) TiO_2 , and c) SiO_2 , taken with a 780 nm diode laser. The reflection drops as the films are heated through the transition, and we see all the films show the characteristic hysteresis of the transition. Each film has a very different transition temperature T_c and transition width, which can be explained by the different microstructures we found in each film.

One way in which the film of VO_2 on TiO_2 is unique compared to the other samples is that the transition is anisotropic. Bulk VO_2 is anisotropic, but most of our films have multiple orientations in the plane, and so there is no preferred direction for reflectivity. However, VO_2 on TiO_2 is a monocrystalline film, and shows a difference in both conductivity and optical properties depending on the orientation of the film. Figure 3.12 shows the

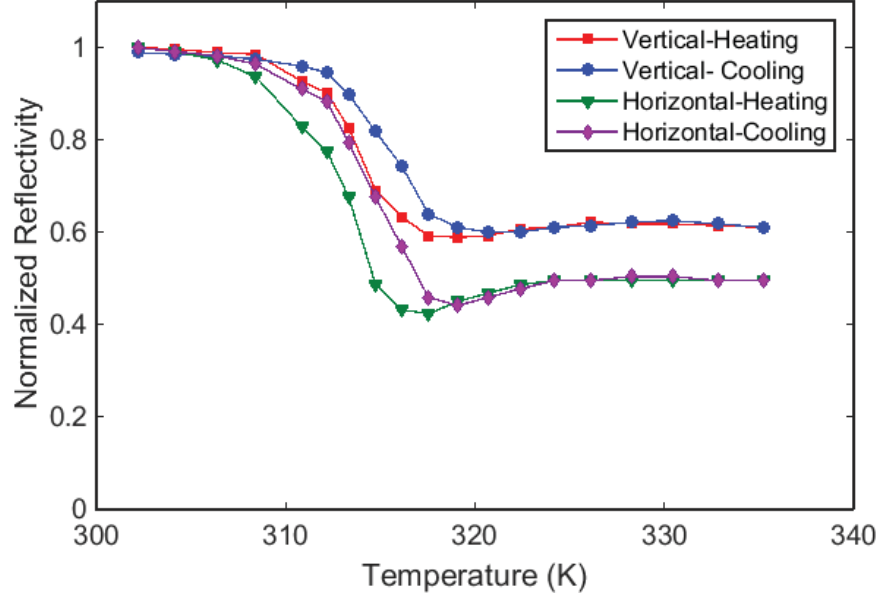


FIG. 3.12: Here is the normalized reflection off of VO_2 on TiO_2 at 780 nm. The change in reflectivity is different depending on the orientation of the film, due to the mono-crystalline nature of the film and the anisotropic nature of VO_2 .

normalized reflectivity along the two different orientations. There is a noticeable difference in the drop in reflection along the two different axes. This is consistent with previous measurements on comparable films.[22]

We also evaluated the penetration depth at 800 nm for both films. For the film grown on Al_2O_3 we looked at the reflection and transmission with a cw laser, which gave us a penetration depth of $\delta = 294$ nm, where $I = I_o \times 10^{-x/\delta}$. The TiO_2 substrate did not have a polished backside, unlike our other samples, so we used ellipsometry to measure its optical constants at a range of wavelengths between 420 nm to 749 nm. We took this data and extrapolated to obtain the real and imaginary parts of the optical constants, and determined a penetration depth of $\delta = 255$ nm at 800 nm.

3.4.1 Modeling Reflection and Transmission

When dealing with thin films, the overall transmission and reflection are going to depend on the thickness of the films, as well as the optical properties of the layers. In order to model the reflection and transmission, I calculated a 4×4 transfer matrix using the method outlined in Shubert's paper.[43] While this is normally a straight forward calculation with an isotropic material, it becomes a much more involved calculation when one includes anisotropic layers with random orientations.

In particular, I checked that the anisotropy of VO_2 grown on TiO_2 could be reasonably probed by changing the polarization, since the reflection from an s or p polarized light is different even in an isotropic material, as shown in figure 3.13.

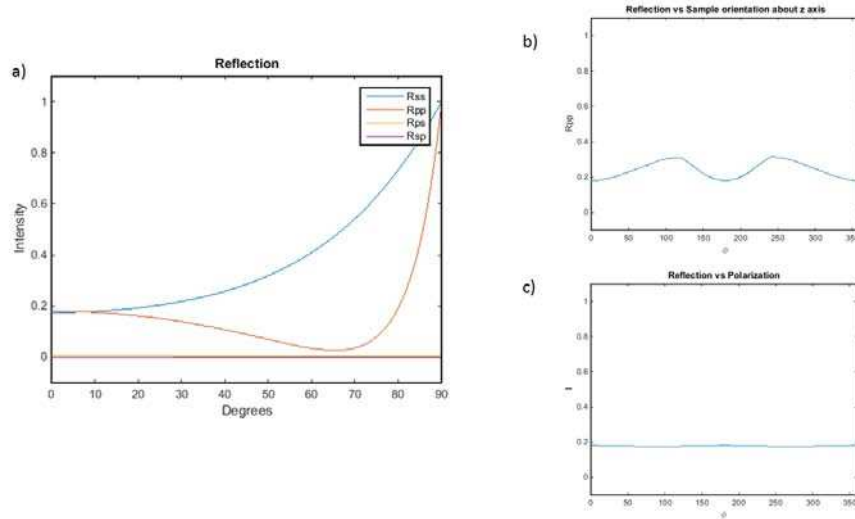


FIG. 3.13: Here are the calculations of M- VO_2 on TiO_2 . The optical constants were measured by ellipsometry. a) shows the s and p reflectivity as a function of incident angle for one orientation of the film. b) shows the p-polarized reflection at an incident angle of 20° as we rotate the sample and c) shows the change in reflection as we rotate the polarization.

In order to calculate a transfer matrix for a series of optical elements, one multiplies the transfer matrix for each individual element in reverse order compared to the beam

direction. For series of thin films the transfer matrix looks like:

$$T = L_a \prod_{i=1}^N T_{ip}(-d_i) L_{out} \quad (3.2)$$

where L_a is the matrix for the interface between the incident medium and the first layer, L_{out} is the matrix for the interface into the exit medium, T_{ip} is the partial transfer matrix for the i 'th layer, and d_i is the thickness of the i 'th layer.

I wrote up a program in MATLAB which calculates the reflection, transmission, and absorption using the general calculation for the partial transfer matrices of a randomly oriented anisotropic crystal. Using index of refraction from ellipsometry and from previous studies [3] I used these calculations to check that our measurements were consistent with available VO₂ data.

3.5 Raman Spectroscopy

3.5.1 Raman Scattering

Raman scattering is an inelastic scattering process where light reflected off a sample is partially absorbed by a vibrational mode in the sample, and therefore has a frequency shift with respect to the incident light due to a decreasing energy. The intensity of the Raman scattering is small compared to the Rayleigh scattering of the incident light, and requires a high intensity incident beam, as well as a notch filter to detect it. By looking at the Raman spectrum of a material, it is possible to measure the energies of the phonon modes that are Raman active (due to lattice symmetry). [27]

We monitored the thermally induced changes in the VO₂ structure using two complementary optical techniques, namely Raman spectroscopy and optical reflectivity of a weak 780 nm laser. The two states of VO₂ have distinct Raman signatures: The insulat-

ing monoclinic phase (at low temperature) displays several sharp Raman peaks, and at temperatures above the transition temperature the Raman spectrum of the metallic rutile phase is characterized by a broadband emission.[44, 45, 46] While we observed this typical behavior in all samples, this transition occurred at a lower temperature for the samples grown on rutile and quartz, compared to those grown on sapphire. Complementary measurements of the optical reflectivity showed a similar trend. A comparison of the crystalline microstructure of the samples shows correlation between the measured temperature at the onset of the phase transition and the average grain size of the different films investigated, consistent with some theoretical predictions.[34, 36, 39] We also experimentally found a wavelength for the excitation laser leading to optimal VO₂ Raman spectra, and found that the near-IR (785 nm) laser yielded the best resolution.

3.5.2 Raman spectroscopy experimental set up

We observed the modifications of the VO₂ samples microstructure through the MIT using Raman spectrometry. The Raman spectra, shown below, were obtained with a Kaiser Raman Rxn1 microprobe using a 50× magnification objective that provided spatial resolution of 11 μm , and a depth of focus of 2 μm . This instrument is configured to operate at three different wavelengths for optical excitation: 532 nm (25 mW), 632.8 nm (3.5 mW), and 785 nm (7.58 mW), allowing us to compare the VO₂ Raman signal at these different optical wavelengths.

Examples of experimental Raman spectra measured at the low-temperature phase (monoclinic) of the VO₂ sample grown on quartz are shown in Fig. 3.14. Group theory predicts a total of eighteen Raman active phonon modes in the low-temperature (insulating) regime: nine Ag modes and nine Bg phonon modes that have been identified in previous works.[44, 45, 46]

In our samples, we have observed a majority of these identified modes (summarized in

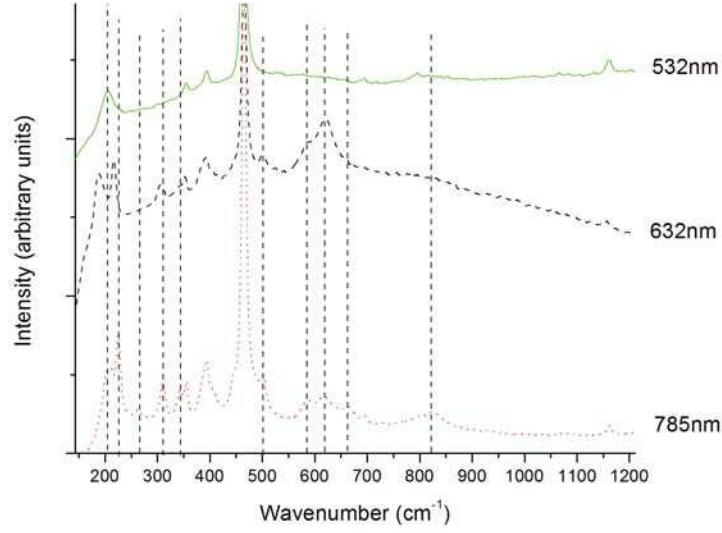


FIG. 3.14: Raman spectra for VO_2 thin films deposited on quartz substrates obtained using different excitation lasers.

Table 3.1). It is important to note that we found none of the peaks associated with other forms of vanadium oxides, in particular, V_2O_5 that has a similar Raman signature. This fact offers good evidence of the high purity of the VO_2 composition in our samples. There are twelve clear VO_2 peaks (ten peaks detectable in the VO_2 on the sapphire sample are identified by dashed vertical lines in Fig. 3.14): 198 cm^{-1} , 225 cm^{-1} , 265 cm^{-1} , 309 cm^{-1} , 342 cm^{-1} , 439 cm^{-1} , 481 cm^{-1} , 501 cm^{-1} , 595 cm^{-1} , 617 cm^{-1} , 660 cm^{-1} , and 810 cm^{-1} . However, on the film grown on sapphire, we have also observed several additional Raman peaks including one near 1075 cm^{-1} , which exhibit temperature dependence consistent with the MIT transition. Moreover, the Raman frequencies of these peaks do not match any of previously identified phonon modes in monoclinic VO_2 , and they lie beyond the expected Raman band for this material. Those peaks will require further study.

Figure 3.14 also shows a strong dependence of the detectability of the VO_2 Raman resonances on the excitation light wavelength. Notably, the clearest spectrum with maximum number of resolved resonances was observed with near-IR excitation ($\lambda = 785\text{ nm}$), while only about half of the peaks were detectable with a red He-Ne laser ($\lambda = 633\text{ nm}$).

For even shorter wavelength ($\lambda = 532 \text{ nm}$), the only visible Raman features were the substrate (quartz) Raman peaks. Such frequency dependence can be attributed to increased contribution of resonance fluorescence for higher-frequency radiation which increases the background and overwhelms any thin film contributions to the detected signal. Thus, our experiments suggest that it is advantageous to use a lower frequency optical wavelength to probe the Raman structure of VO_2 thin films. Since the Raman signature of the substrates was even stronger for the VO_2 films grown on sapphire and rutile, we were able to observe VO_2 Raman peaks only with the IR laser for these samples.

Schilbe13		Pan et al.14		Chen15		Present work	
Peaks	Modes	Peaks	Modes	Peaks	Modes	On quartz	On sapphire
149							
199	Ag	194	Ag			198	200
225	Ag	225	Ag	226	Ag	225	223
259	Bg	258	Bg	262	Ag	250	No
265	Bg	265	Bg	264	Bg	262	266
313	Ag	308	Ag	311	Bg&Ag	309	308
339	Bg	339	Bg	339	Ag	342	339
392	Ag	392	Ag	390	Ag	Blocked	
395	Bg	395	Bg	395	Bg	Blocked	395
444	Bg	444	Bg	444	Bg	439	443
453	Bg	453	Bg	454	Bg	Blocked	453
489	Bg	489	Bg	483	Bg	481	486
503	Ag	503	Ag	500	Ag	501	497
595	Ag	585	Ag	591	Bg	595	No
618	Ag	618	Ag	618	Ag	617	616
670	Bg	650	Bg	662	Bg	662	660
830	Bg	825	Bg	826	Bg	810	825

TABLE 3.1: Comparison of measured monoclinic VO_2 Raman resonances with previously reported results.

Figure 3.15 shows examples of Raman spectra taken at different temperatures above and below the insulator-metal transition for different VO_2 samples. The two possible structures of VO_2 below and above the MIT temperature have distinctly different Raman

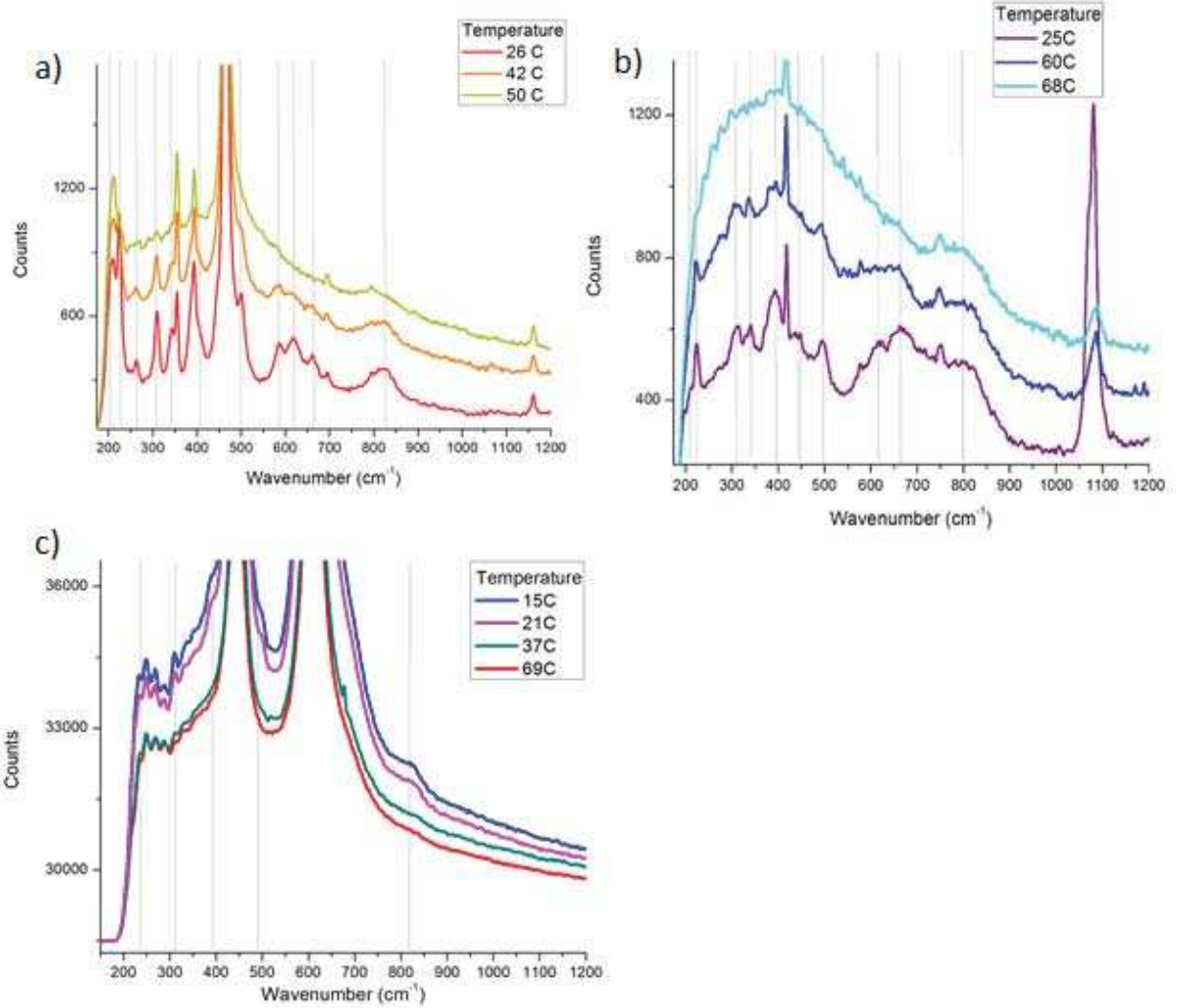


FIG. 3.15: Evolution of Raman spectra for VO_2 thin films deposited on (a) quartz, (b) sapphire, and (c) rutile substrates through the thermally induced MIT. Dashed vertical lines indicate expected positions of M-VO_2 Raman resonances. Unmarked peaks are substrate resonances. Two particularly strong rutile peaks are out of range in (c) in order to highlight the much weaker VO_2 peaks.

signatures, clearly displayed in the experimental data. At low temperatures we observed the sharp spectral features associated with the monoclinic phase, while at higher temperatures we expect to see spectrally broad features associated with the tetragonal conducting phase, as indeed was the case. Thus, as the temperature of a sample increases, the amplitudes of the sharp monoclinic peaks decrease as the sample undergoes the transition. In our experiment, we have not observed any substantial difference between Raman frequencies of VO₂ monoclinic peaks for samples grown on different substrates, although depending on the substrate material, some of the expected resonances were obscured by the stronger substrate Raman peaks. However, as none of the substrate Raman features are temperature-dependent, it is possible to clearly identify any peaks that can be associated with a VO₂ film. It is interesting to note that in previous work[45] the phonon modes of different symmetry groups display different temperature behavior. However, in our experiment we did not observe such difference. In particular, a 224 cm⁻¹ peak (Ag mode) and 660 cm⁻¹ (Bg mode) disappeared at the same rate for both samples when the films were heated.

On Figure 3.16, we display the thermal dependence of the optical properties of the VO₂ samples undergoing MIT: reflectivity measurements with a 780 nm cw laser (left column) and the amplitudes of some well-resolved Raman peaks, associated with the monoclinic VO₂ film (right column). We observed the characteristic reduction in optical reflectivity at the MIT critical temperature T_c . [3] For each of the three samples, we observe only a small difference between the transition temperatures for heating and cooling, manifesting a very narrow hysteresis (with exception of some low-temperature portion of the quartz sample). However, the temperatures at which this transition occurred were quite different depending on the substrate material. We observed the lowest transition temperature for VO₂ film grown on TiO₂, with a $T_c=306$ K. We see this for both sets of measurements, namely the cw measurement and the rate of disappearance of the Raman peaks. For

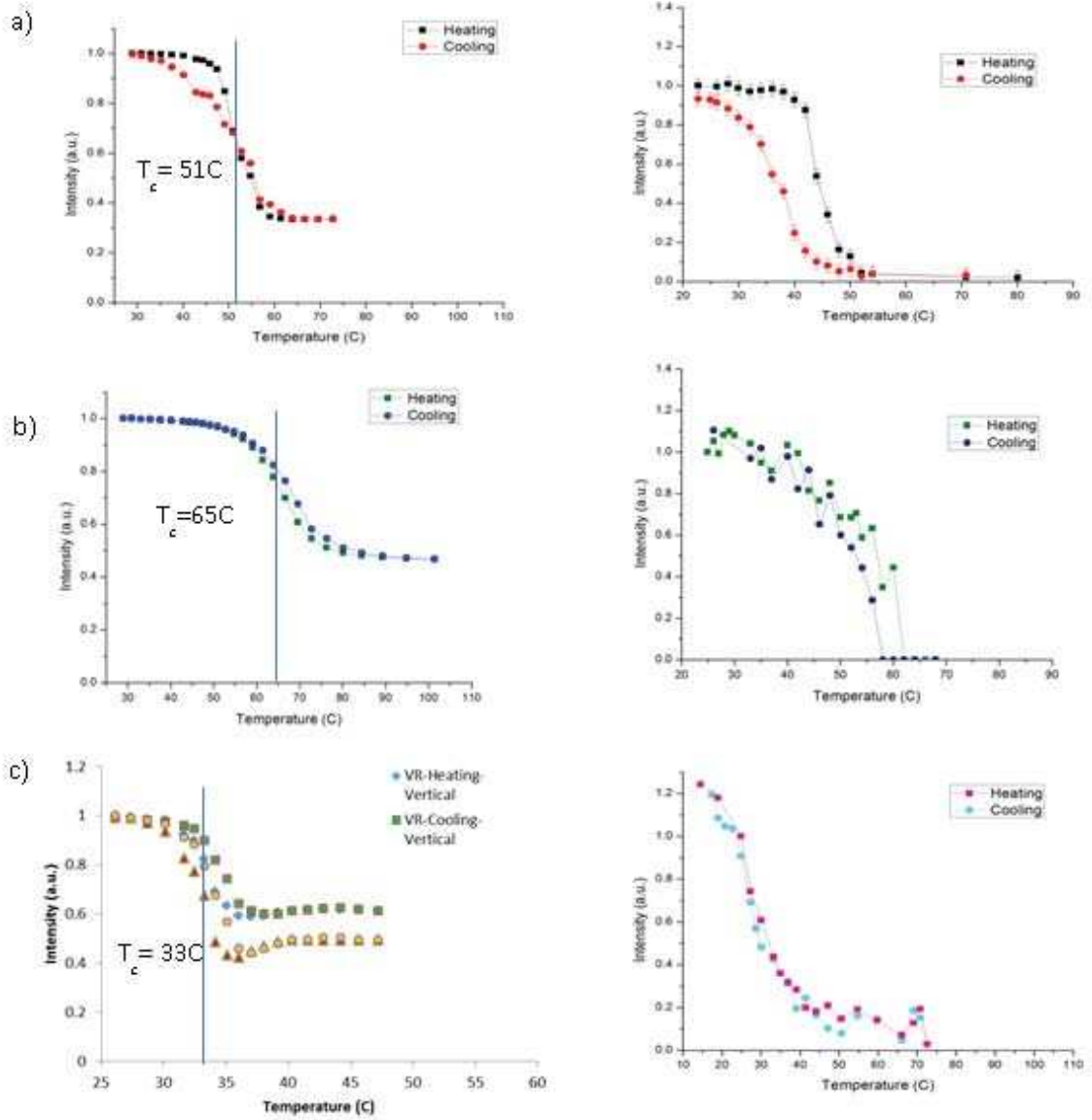


FIG. 3.16: Comparison of the MIT evolution for VO_2 thin films grown on different substrates. Left column: Reflectivity measurements with a 780 nm cw laser. Right column: Change in Raman peak intensity in each film. (a) VO_2 film on quartz, peak 224 cm^{-1} . (b) VO_2 film on sapphire, peak 224 cm^{-1} . (c) VO_2 film on rutile, peak 309 cm^{-1} . For the anisotropic rutile sample, the reflection for two orthogonal polarizations is shown. Some variation in transition temperature between the two detection methods may be due local heating due to focused pump beam in the Raman spectrometer. Vertical lines indicate the temperature for the phase transition temperature T_c .

VO₂ on quartz and sapphire we see $T_c=324$ K and $T_c=338$ K, respectively. We note that MIT seemed to happen at lower temperatures in Raman measurements compared to the reflectivity measurements, most likely due to local heating of the sample by the Raman pump laser. For that reason, we use optical measurements for extracting the transition temperature.

The different behavior observed in the transition temperature for VO₂ thin films deposited under identical conditions but on different substrates can be attributed to differences in the microstructure of the films. Previous experiments have demonstrated that doping[6] and/or the size of the nanostructures[45, 47] can alter the average temperature of the phase transition, although the dominant effect in this case is broadening of the hysteresis loop. In our case, however, all three samples display a very narrow thermal hysteresis width, as seen in Fig.3.16.

We attribute the observed changes in transition temperature mainly to variation in the VO₂ film microstructure, mainly the average grain sizes. A proposed model, describing the properties of the MIT in thin films, considers the overall hysteresis curve as a combination of individual microscopic loops for individual VO₂ grains.[34, 36] In this model, it is postulated that in very thin films the grains are rigidly bound to the substrate and strain relaxation at the grain-substrate interface controls the temperature of the transition, and consequently the degree of strain relaxation upon nucleation determines the width of the thermal loop as well as the shift toward lower transition temperature as a function of grain size. Thus for an average grain size d , the structural transition occurs at a temperature

$$T_{film} = T_{bulk} - A/\sqrt{d} \quad (3.3)$$

where $T_{bulk} = 340$ K is transition temperature for the bulk VO₂, and A is a constant, determined by the material parameters of both the film and the substrate.[34]

We applied this model to our data using the average grain sizes estimated from the XRD data. We noted that indeed the smaller the grain size the lower is the transition temperature as the sample is heated. Table 3.2 shows the average values of the transition temperature from the optical reflection measurements, shown in Figure 3.16, average grain sizes and estimated value of constant A for all three substrates.

Substrate material	T_c , heating ($^{\circ}\text{C}$)	T_c , cooling ($^{\circ}\text{C}$)	Grain size, d (nm)	A ($^{\circ}\text{Ccm}^{-1}$)
Sapphire	64	67	65	32 ± 8
Quartz	51	51	20	67 ± 5
Rutile	33	34	12	131 ± 3

TABLE 3.2: Average transition temperature, grain size, and estimated value of constant A for VO_2 films grown on each substrate. The error bars for the values of A are calculated using 1° uncertainty in the transition temperature measurements

These differences are not surprising when we consider the differences we see in the microstructure of the films from XRD. The film on TiO_2 is monocrystalline, and therefore is likely to have fewer defects from lattice mismatch; this is reflected in the narrower transition. It also has the lowest transition temperature, that is due to the fact that the substrate is has a tetragonal lattice structure, like the R- VO_2 phase. This is reflected in the fact that the phi-scan exhibits a tetragonal symmetry like R- VO_2 , implying that the film is "clamped" at the R- VO_2 phase. From the Raman measurements, we see modes associated with M- VO_2 , so it is probable that there is a mix of the two phases at room temperature. This leads to a higher strain in the film when it is in the M- VO_2 phase, bringing down the energy needed to drive the transition. Other works have shown one can control the T_c depending on how much of a mismatch there is between VO_2 and the substrate.[48, 22, 40] While our XRD measurements show a $\sim 1\%$ shift in the d-spacing of the planes, indicating little strain, the lower T_c is likely the result of clamping, thus reducing the energy required for the structural transition upon the IMT.[49, 50]

The film on Al_2O_3 has an almost bulk like transition temperature, and the width of the transition is much broader. The average grain size is much higher and there is a connection between the grain size and the T_c of the individual grains. [34, 36, 39]

3.5.3 Conclusion

In conclusion, we characterized our thin films, with XRD, continuous wave optical measurements, and Raman spectroscopy. We observed that the Raman peaks associated with the monoclinic VO_2 insulating phase disappear at different temperatures upon annealing thin films of VO_2 deposited on different substrates. Since we observed a noticeable substrate effect on the films microstructure, we speculate that this change in the individual microstructure of each sample is responsible for the shifts in the MIT temperature. This difference in transition temperature was confirmed using optical reflection measurements. Specifically, we attribute this variation in transition temperature to the difference in average grain sizes in VO_2 films, thus opening an exciting avenue for tailoring the transition temperature for applications. An important advantage of the proposed model that we applied to our samples, compared to some previous proposals, is that the shift in transition temperature does not result in broadening of the MIT hysteresis, in agreement with our observations. We also compared the relative sensitivity of the VO_2 spectra using different wavelength pump lasers, and found that best spectral contrast was obtained with 785 nm laser excitation, due to reduced fluorescence background of the substrate material. This information will be useful for future investigations on thin VO_2 films, in which the low optical depth of the film results in a stronger Raman signature from the substrate.

CHAPTER 4

Ultrafast Pump-probe Experimental Set Up

4.1 Ultrafast Laser system

As mentioned the dynamics of the transition dynamics of different films of VO_2 can provide important information about the mechanisms of the insulator metal transition. When optically pumped, these transitions can happen on the order of 100 fs [51]; and at lower powers, it takes on the order of 100 ps to fully transition.[9] These timescales are very difficult to measure using continuous wave (cw) lasers. Our photodetectors at best take tens of nanoseconds to respond. By using a laser system that produces ultrafast pulses, we can split the pulse into two paths, one to pump and one to probe the sample. By changing when the probe hits the sample, we can scan over time with a resolution determined by the pulse duration, not by the photodetector.

In order to create or detect laser pulses that are shorter than a few hundred picoseconds one cannot use external devices, since electronics are not fast enough in their response

times. It is possible to achieve these shorter pulses by designing a cavity that sustain a large number of frequencies: if you have an infinite number of E&M waves that are different frequencies that have the same phase, by adding them all together you have a delta peak. No gain medium is going to have a gain in all frequencies, but with a reasonably large bandwidth, the cavity will output a series of narrow peaks.

The difficulty in setting up an ultrafast system, then, is to find a gain material that has a sufficiently large bandwidth, and to force all the different frequencies to sync up, or 'mode-lock'. Many ultra-fast systems use Ti:sapph crystals, as the gain bandwidth can be as broad as 200 nm[52].

Our oscillator mode-locks by passive mode-locking. Passive mode-locking occurs when the cavity length is varied rapidly. This changes the modes that the cavity can support, and if enough modes are in phase, then the Ti:sapph saturates and is unable to support other modes out of phase with the peak. Other modes that are not in phase will not be able to lase outside this window and will die out. Eventually all the modes will be sync up in the time window that Ti:sapph allows. [52]

Another reason that the Ti:sapph is an ideal material for making femto-second pulses is that it further compresses the pulse as it travels through the material due to the Kerr effect. The Kerr effect is non-linear effect where a material's index of refraction changes in response to a large electric field (in this case from the intensity of the beam itself). At the tail ends of the pulse, the intensity is low enough that there is no change in the index of refraction, while at the peak there is a change. This causes the front of the pulse to travel slower than the back of the pulse in the Ti:sapph crystal, and results in the pulse having a shorter duration. [52]

The commercial laser system we use contains an oscillator (Mantis from Coherent), and an amplifier (Legend Elite from Coherent). The pulses out of the Legend Elite are 100 fs, and have a repetition rate of 1 kHz. The central frequency is 800 nm and the

bandwidth of 8.5 nm. Each pulse has 1 mJ of energy, and the average power is 1 W.

4.2 Characterizing Pulses

4.2.1 Pulse duration

The commercial specs for the Legend-Elite amplifier give us a pulse duration of 100 fs. However, ultrafast laser systems are very susceptible to lab conditions, so it is important to be able to confirm this. In addition, we use different pulse lengths for our experiments, making it important to monitor pulse duration.

One possible check for the pulse duration is looking at the spectrum of the beam. If the spectrum has a certain bandwidth, that sets a limit on the minimum pulse width, as described by

$$\Delta\nu\Delta t \geq K \quad (4.1)$$

where $\Delta\nu$ is the bandwidth at full width half max, and Δt is the duration of the pulse, and K is a constant determined by the shape of the pulse[52]. For a Gaussian pulse, $K = 0.441$. This is a manifestation of the Heisenberg uncertainty principle. The larger the bandwidth, the shorter the pulse can be. We can also calculate Δt from the distribution of wavelengths (as measured with our Ocean optics spectrometer) with the relationship

$$\Delta t = K \times \frac{\lambda_o^2}{\Delta\lambda \times c} \quad (4.2)$$

From the measured spectrum, $\Delta\lambda = 8.57 \text{ nm}$ and $\lambda_o = 801 \text{ nm}$. From this we get a minimum pulse duration of 110 fs, which matches the specs. However, this assumes that all the modes have the same phase. If there is group velocity dispersion, the pulse duration will spread. In addition, we vary the duration of the pulse for our experiments. To confirm that the pulse is optimally compressed by the Legend, we need a way of directly measure

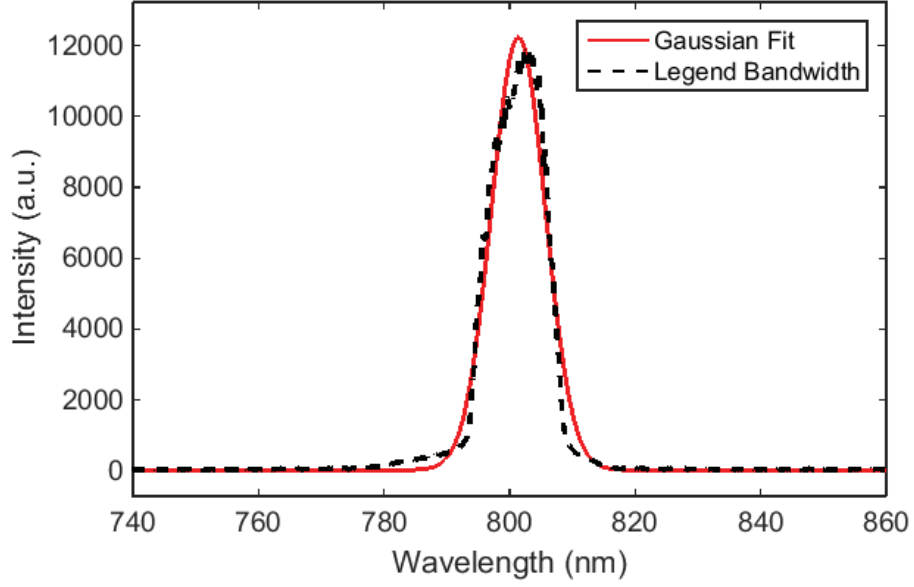


FIG. 4.1: This is the measured bandwidth of the ultrafast pulse coming out of the Legend amplifier (the pulses used for most of this work). By fitting with a Gaussian, we can get an estimate of the limit on the duration of the pulses coming out of the system.

the pulses. The pulses of our laser system are short enough that even fast photodiodes are not fast enough to measure their duration. So in order to measure on the time scales of the pulses, we need to use the pulse itself to characterize it. We assembled an autocorrelator with the aid of Shukui Zhang and Mike Klopff from Thomas Jefferson National Laboratory, and used it to monitor pulse duration for our experiments.

An autocorrelator works by splitting the beam into two pathways. These pulses are then recombined at a small angle in a material with a strong second order process. In our case we use a BBO crystal that has second harmonic generation (SHG) at 800 nm. SHG is a two photon process, so at low enough intensities there will be no blue-light generation with a single pulse. But with both pulses overlapping, photons from both pulses create sufficient intensity to produce a blue spot (400 nm) in-between the two incoming 800 nm beams.

In order to find the pulse duration δt , we fit the beam with a Gaussian to get the width

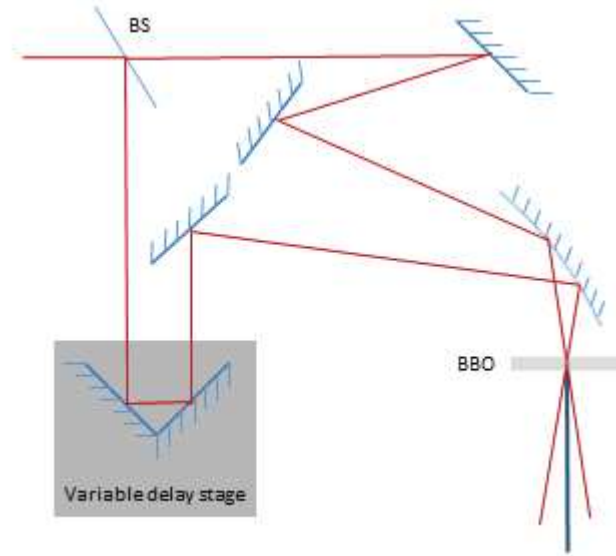


FIG. 4.2: An autocorrelator divides the pulse into two pathways. Recombining the beams in a Beta Barium Borate (BBO) crystal will only produce blue light when the pulses overlap both temporally and spatially. By looking at the profile of the blue light we can determine the pulse duration Δt .

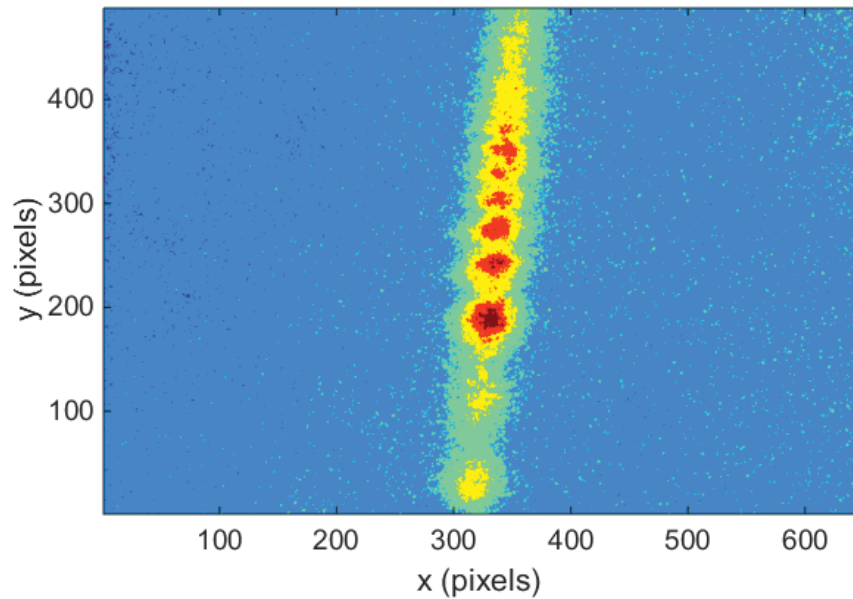


FIG. 4.3: The image from the camera of our autocorrelator shows the SHG from the combination of the two pulses in the BBO crystal. The width of the beam is related to the pulse duration. Each pixel is 7.4 microns.

of the beam. In order to calibrate the autocorrelator, we take an image after changing the length of one of the beam paths with a delay stage. There is a linear relationship between the beam position on the camera and the change in time delay of the pulse. From this we can calculate δt by

$$\delta t = \frac{\delta x \times m}{\sqrt{2}} \quad (4.3)$$

where δx is the fitted width of the beam in the horizontal direction, m is the slope of change in time delay over change in beam position. The $\sqrt{2}$ is a correction factor based on the assumption that the pulse envelope is Gaussian.

4.2.2 Fluence and Spot size

The Fluence of a beam is defined as the energy of the laser pulse over the area of the cross-section of the beam. This area is calculated from the waist the Gaussian beam profile. The waist is the distance from the center of the beam to where the intensity drops to $1/e^2$. If P is the average power of the beam, R is the repetition rate, and w_o is the waist of the beam, we can calculate the fluence by this equation:

$$F = \frac{P}{R \times \pi w_o^2} \quad (4.4)$$

The repetition rate of our laser system is 1 kHz, and the waist size depends on the focal length of the lens. We used a camera to measure the spot size of our pump beam. However, the camera we used had a resolution of 7.4 microns per pixel, and was prone to saturate at the focal point. So we took images of the cross-section of the beam at several points after the lens. From that we were able to fit the waist size with the equation for a gaussian beam[53],

$$w(z) = w_o \sqrt{1 + \frac{z^2}{z_o^2}} \quad (4.5)$$

where z is propagation distance from the focus, $w(z)$ is the beam radius at z , and z_o is Rayleigh range. This gives us a more accurate size for the waist at the focus. Thus the focal length of the pump laser is 50 cm, and has a waist of 90 microns.

4.3 Pump-probe set up

The majority of the measurements made in this work were in a pump-probe configuration, as can be seen in figure 4.4. In our set up, a pulse is split with an (20/80) beam-splitter, where the more powerful leg is sent through a variable neutral density filter, allowing us to control the power in the pump pulse. It is focused with a 500 mm lens. This pump-pulse is used to pump our thin films and optically induce the phase transition.

The second leg is sent down a variable delay stage (total length of 600 mm) before being further attenuated and focused onto the sample with a 250 mm lens. By changing the path length, we change the amount of time that it takes for the pulse to reach the sample. This allows us a finer time resolution than we could get just from measuring the response from a continuous wave beam.

By changing the distance that the probe pulse travels, we can get a snapshot of the film's response at some Δt after the pump pulse hits the sample. So at negative Δt , the probe is looking at times before the pump hit the sample, and at positive Δt the probe is measuring the sample's reaction to the pump pulse. Thus we can measure the change in reflection over time, and track the film's dynamic response. The delay stage has a range of 600 mm (4 ns) and a step size of 1.25 microns (8 fs). This is a much finer resolution than our pulse length, which means our time resolution is limited by the laser pulses, not the stage.

In all measurements, reported below, the relative change in reflection $\Delta R/R$ is defined as $\frac{R_o - R(\tau)}{R_o}$, where $R(\tau)$ is the power of the measured reflected probe beam as the function of the delay τ between the pump and the probe pulses, and R_o is the probe reflected power

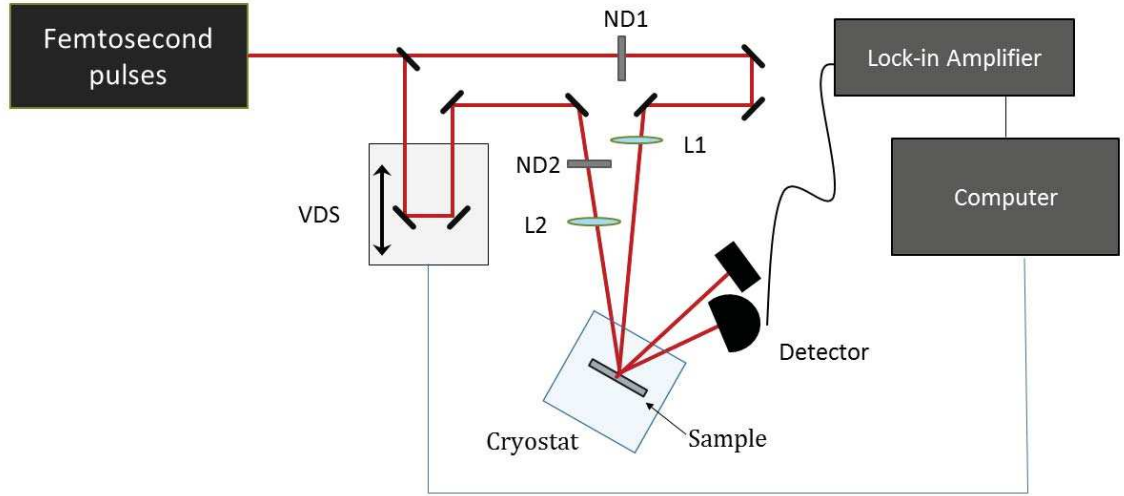


FIG. 4.4: Schematics of the optical pump-probe experimental setup. The output of the amplified ultrafast laser is split into weak probe and strong pump beams using a (20/80) beamsplitter (BS). The energy of the pump pulses is controlled by the variable neutral-density filter ND1, while the probe beam was sent through a computer-controlled variable delay stage (VDS) and further attenuated using ND2 (OD=3.0). The probe and pump beams were focused on the same spot at the surface of the sample, placed inside a cryostat, using 250-mm and 500-mm lenses, correspondingly. The reflected probe power was measured by a photodetector (PD), and further analyzed using a lock-in amplifier.

in the absence of the pump beam. For Chapter 5, because our work is based on reference [12], we multiply $\Delta R/R$ by -1 in order that our descriptions of the behavior is consistent with the previous work. For the measurements described in Chapter 5, the sample is mounted in a cryostat, such that we can control the temperature of the sample, and see how the dynamics of the phase transition change as we cool the sample.

CHAPTER 5

Phase Diagram of the Dynamics of the Ultrafast Response

5.1 Introduction

In the experiments reported in this chapter, we have focused our investigations on the effects of a substrate (material and microstructure) on the ultra-fast photo-induced MIT in two VO_2 thin film samples, specifically grown on TiO_2 [011] and c- Al_2O_3 . For these measurements the MIT was induced by a strong ultrashort (~ 100 fs) laser pulse, and the optical properties of the films were probed by a much weaker probe pulse, after a controlled delay. Following the methodology, proposed by Cocker et al.[12], we have observed and mapped out a range of values of the pump laser fluence corresponding to distinct phases of the photo-induced MIT at various sample temperatures. We then analyzed the possible connection between the two film's microstructure and observed differences in MIT dynamics.

5.2 Measurements of the IMT Temporal Evolution

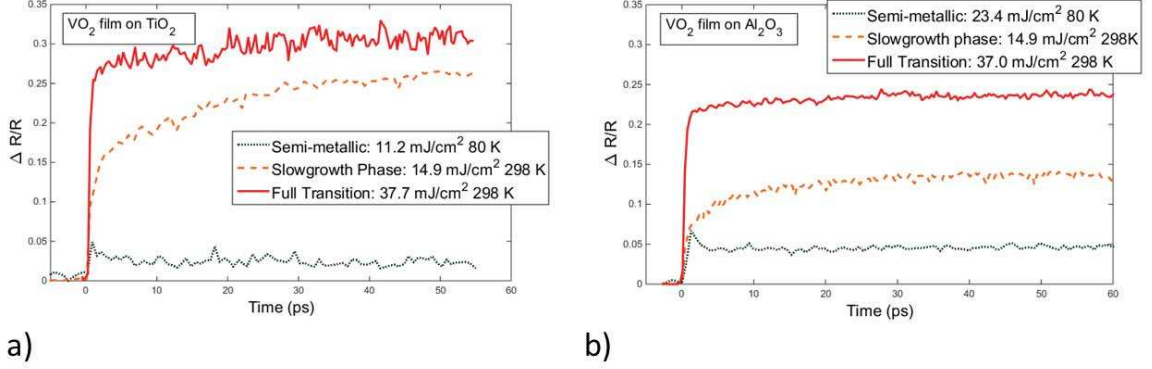


FIG. 5.1: Sample time-dependent changes in the probe reflection corresponding to various dynamical phases of MIT, measured for (a) VO₂/TiO₂ and (b) VO₂/Al₂O₃ samples. The pump pulse hits the sample at zero time, and positive delay times correspond to the probe beam interacting with the sample after the pump beam.

Overall, the temporal evolution of the photo-induced transition in both samples followed similar trends, as illustrated in Fig. 5.1. We varied the pump pulse energy and the temperature we held the sample, keeping the initial temperature well below the T_c . For both films we observed three distinctive dynamical IMT regimes. Similar behavior has been previously reported by Cocker et al[12] in their studies of the THz probe transmission evolution in a photo-induced IMT in a VO₂ film deposited on Al₂O₃. At sufficiently high fluences, we observed a very fast (< 1 ps) change of the probe reflectivity from the value corresponding to the insulating VO₂ state to the fully metallic VO₂ state, that implies that the whole VO₂ films quickly transitioned from the insulating to the fully metallic state ("full-MIT" phase). We characterize the minimum pump fluence value required to achieve this full transition as $\Phi_{full-MIT}$. For intermediate values of the pump fluence below $\Phi_{full-MIT}$, the film reflectivity also changed immediately after the pump pulse, but this change did not reach the value corresponding to the fully metallic VO₂, implying that

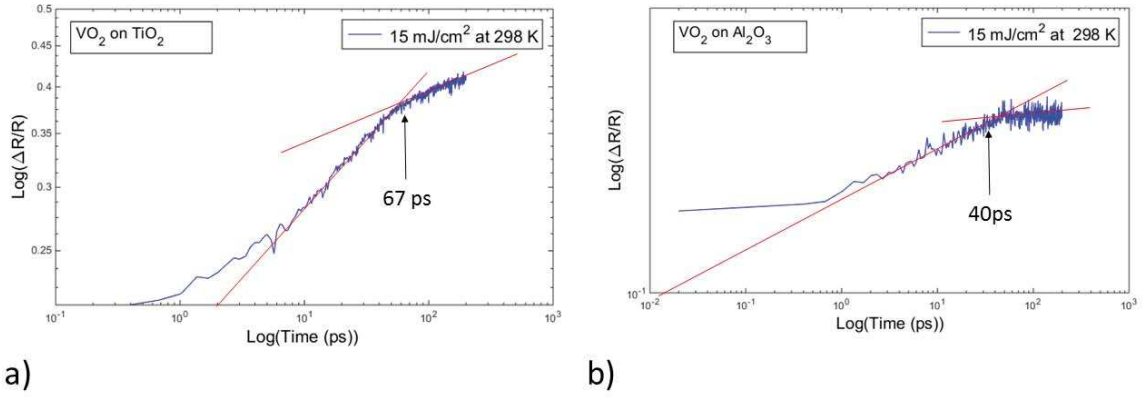


FIG. 5.2: "Slow growth" of relative reflectivity with time, measured for (a) VO_2/TiO_2 and (b) $\text{VO}_2/\text{Al}_2\text{O}_3$ samples with pump fluence of 15 mJ/cm^2 at 298 K , using a log-log scale ("slow growth" phase data in Fig.5.1). Log-log scale clearly shows two time scales of growth for both films. For the $\text{VO}_2/\text{Al}_2\text{O}_3$ sample, the initial faster reflectivity growth (time constant $7.4 \pm 0.3 \text{ ps}$) for the first 40 ps was followed by much slower growth with time constant of $33 \pm 8 \text{ ps}$. For the VO_2/TiO_2 film the switch occurred at approximately 67 ps, from the time constant $6.3 \pm 0.2 \text{ ps}$ to $15.0 \pm 0.6 \text{ ps}$.

the resulting state of the film contains both metallic and insulating regions. Moreover, after this initial sub-picosecond change the relative reflectivity continued to grow at a much slower rate for a few hundreds of ps ("slow growth" phase), indicating further coarsening of the metallic component of the VO_2 film. Interestingly, this dynamical behavior is consistent with the slow coarsening of metallic puddles within the insulating matrix, observed in the thermo-induced MIT.[38, 54, 55, 56] Fig. 5.2 shows the change in both samples reflectivity $\Delta R/R$ at 15 mJ/cm^2 on a Log-Log scale to characterize the rate of this evolution more clearly. It is easy to see the two distinct time constants of this slow growth for both films, with two distinct switching times. In general, the rate of slow growth decreased at the lower values of the pump fluence.

At lower values of the pump fluences, the time evolution of the film became dependent on the temperature of the sample. At higher temperatures if the pump fluences is

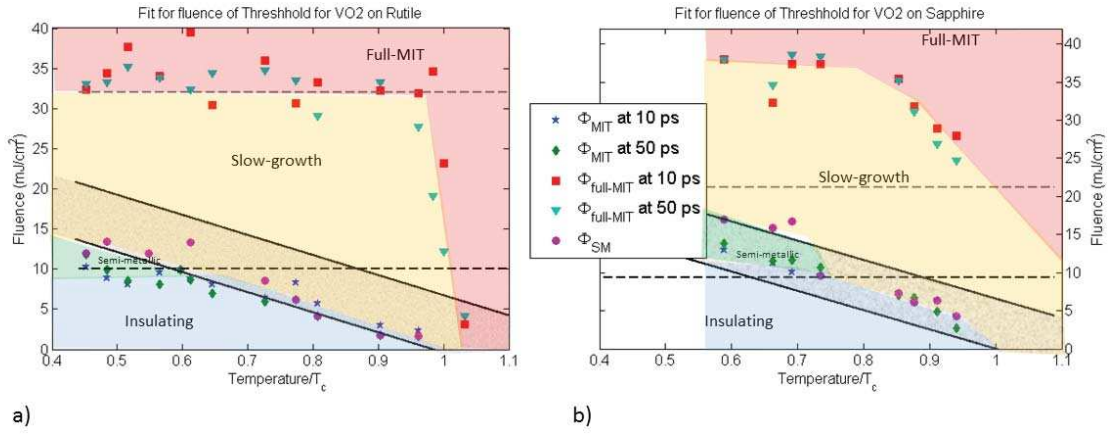


FIG. 5.3: Threshold measurements for the onset and for the full IMT of VO_2 thin films grown on a) TiO_2 and b) Al_2O_3 . Blue stars/Green diamonds correspond to the threshold fluence needed to see a 2% rise in reflectivity at 10 ps and 50 ps, correspondingly. The red squares and cyan triangles correspond to the fluence required to reach the reflectivity value for a fully metallic film in the first 10 ps and 50 ps, correspondingly. The purple circles indicate the boundary where the "slow-growth" phase starts Φ_{SM} . To define this boundary, we took several measurements of the probe reflectivity $\Delta R/R$ as a function of time for the first 20 ps at a range of pump fluences, fitted their linear slopes, and then found fluence values at which the slope becomes indistinguishable from zero within the measurement uncertainty. The dashed lines are the calculated photo-excited electron densities at the front and the back of the films. The shaded region between the solid lines is calculated fluence needed to bring the films up to the transition temperature.

insufficient to reach the slow growth regime, the reflectivity of the sample after the first few ps returned to its insulating value, indicating no long-term changes in the VO₂ state. However, at the lower temperatures (below 250 K for VO₂/Al₂O₃ and below 220 K for VO₂/TiO₂) we clearly observed an intermediate “semi-metallic” phase, as shown in Fig 5.1. For this regime, which occurs at lower fluences than the slowgrowth phase, the pump pulse induced the initial few percent change in relative reflectivity, but then it remained constant, implying no further changes in the VO₂ film phase distribution. While we observed a qualitatively similar photo-induced IMT dynamics for the two VO₂ films grown on TiO₂ and on Al₂O₃ substrates, the structural differences between the two films clearly affected the experimental conditions for realization of each IMT phases. To highlight these differences, Fig. 5.3 shows the experimentally measured values of the fluence thresholds between the phases: $\Phi_{full-MIT}$, the fluence required to induce a fast full transition to the metallic stage; Φ_{SM} , the fluence sufficient to induce the partial MIT, followed by the slow growth of the metallic component; and Φ_{MIT} , the minimum pump fluence required to produce any phase transition in the insulating VO₂ film. For consistency each threshold value was measured for 10 ps and 50 ps delay between the pump and the probe pulses. Also, to take into account the difference between the critical temperatures for the two VO₂ samples, for the phase diagram in Fig. 5.3 we used the relative temperature T/T_c for each sample.

The most noticeable difference between the two samples was observed in the temperature dependence of the full-MIT threshold $\Phi_{full-MIT}$. For the VO₂ film on Al₂O₃ the values of $\Phi_{full-MIT}$ increased slowly as the sample temperature dropped. At the same time, for the VO₂/TiO₂ sample the entire full IMT boundary $\Phi_{full-MIT}$ remained constant for all the temperatures $T/T_c < 0.95$, after the sharp drop around T_c . Remarkably, the measured values for the threshold fluence in the two samples were rather similar (around 32-34 mJ/cm² for $T/T_c \sim 0.6$) despite the structural differences of the films.

The other two threshold values, corresponding to a partial IMT displayed similar temperature dependences for both samples: at lower sample temperatures it required higher pump power to induce the same change in the sample. However, the exact values for Φ_{MIT} and Φ_{SM} were higher for the $\text{VO}_2/\text{Al}_2\text{O}_3$ sample. We also observed the separation of the slow-growth phase and the semi-metallic phase for temperatures below $T/T_c \leq 0.7$ for the both films.

It is important to note that the IMT dynamics for $\text{VO}_2/\text{Al}_2\text{O}_3$ sample observed in the current experiment using all-optical pump-probe detection, was qualitatively similar to that for a similar $\text{VO}_2/\text{Al}_2\text{O}_3$ sample studied by Cocker et al.[12] using 800 nm optical pump pulses and broadband THz probe pulses. Their reported values for threshold fluences were 2-3 times lower than those shown here in Fig. 5.3. However, other works have shown higher threshold values for the onset of MIT, around 7 mJ/cm², and show comparable behavior at higher fluences. [9, 8]

5.3 Mechanisms of Ultrafast MIT

Accurate theoretical description of the fast dynamics of the electron system in VO_2 is a very challenging problem. It requires a proper description of the strong electron-phonon coupling and of the strong electron-electron correlations in the insulating phase, and of the interplay between these correlations and the lattice structure dynamics. However, the analysis of the experimentally measured time evolution of the VO_2 reflectivity after the pump pulse may allow us to infer qualitatively the dominant processes that govern the dynamics in the VO_2 films that we have studied and, in particular, how these processes differ between VO_2 films deposited on TiO_2 and on Al_2O_3 .

After the pump pulse the reflectivity, $\Delta R/R$, of the VO_2 film, that is initially in the insulating phase, increases on a very short time scale[13], shorter than our time resolution ~ 0.5 ps for these measurements, as shown in Fig. 5.1. The change in reflectivity soon

after the pump pulse was shown to be directly proportional to the pump fluence,[13] and therefore can be attributed to the almost instantaneous excitation of electrons from the valence band to the conduction band of the monoclinic phase of VO_2 by the pump pulse.

As shown clearly in Fig. 5.1, and described in the previous section, the behavior on time scales longer than 1 ps strongly depends on the pump fluence and the temperature of the sample[12].

For sufficiently high values of the fluence $\Phi \geq \Phi_{full-MIT}$, the reflectivity increased to the values matching that of the fully metallic VO_2 film[41]. This indicates that for this regime the population of electron-hole excitations created by the pump pulse was large enough to cause a structural deformation[13, 57] throughout the whole VO_2 film and nearly instantaneously drove it from the monoclinic to the rutile phase. The rutile phase is metallic and therefore the excited electrons have no states in the valence band to which they can decay to. For this reason, the film remains metallic until the lattice cools down to temperatures below T_c causing the reversed transition from rutile to monoclinic. This relaxation process is slow and takes place on time scales much longer ($>$ a few ns) than the time interval (few hundred ps) considered in this experiment.

In the limit of weak pump pulses (below a threshold value Φ_{MIT}), the observed change in reflectivity did not last much beyond the duration of the pump pulse, quickly returning to its original value. This can be attributed to the fast relaxation of the particle-hole excitations created by the pump laser: since the number of electron-hole excitations is not high enough to induce a coherent lattice deformation and to drive a noticeable fraction of the VO_2 film from the monoclinic insulating phase to the rutile metallic phase, electrons decay quickly from the conduction to the valence band of the monoclinic structure, quickly restoring the original value of the measured reflectivity.

The time evolution of the reflectivity is more complex at intermediate values of the fluence $\Phi_{MIT} < \Phi < \Phi_{full-MIT}$. For these values, the reflectivity kept increasing after

the almost instantaneous step. We attribute this behavior to the fact that for $\Phi_{MIT} < \Phi < \Phi_{full-MIT}$ the population of electron-hole excitations created by the pump pulse is large enough to trigger a coherent structural deformation that drives the lattice from the monoclinic phase to the rutile phase in some regions of the sample but not in the whole sample. The rutile regions initially form, then heat up the surrounding monoclinic regions and drive them to the rutile phase, as well. This process leads to coarsening of the metallic regions, and may be responsible for the observed continuing increase of the reflectivity on time scales of the order of tens of picoseconds. It also may explain the existence of two timescales in the slow growth regime, shown in Fig. 5.2: at shorter times the change in reflectivity can be dominated by lattice vibrations that can persist up to 100 ps after the initial pump pulse excitation[20]. At later times, heat diffusion mechanisms dominate the transition dynamics.

In this model we expect the values of Φ_{MIT} to decrease as the sample temperature approaches the critical temperature of the thermo-induced transition, since a lower number of electron-hole excitations is necessary to drive the structural phase transition. It is also expected that the semi-metallic phase should appear at the lower temperatures ($T/T_c < 0.7$ for both samples) and lower pump fluences $\Phi_{MIT} < \Phi < \Phi_{SM}$, corresponding to a situation in which the power is sufficient to trigger the IMT transition in isolated regions, but not enough to induce the growth of the metallic regions in the rest of the sample.

We now discuss how the measured structural differences between the two VO₂ films may affect the dynamics of the photo-induced MIT. The large measured strain induced by the TiO₂ substrate indicates that the equilibrium monoclinic VO₂ film is already deformed toward rutile structure, thus making the structural transition easier. This, and the more ordered mono-crystalline structure of the VO₂/TiO₂ samples seems to favor the formation of the more uniform nucleation sites during MIT, as evident by the narrower thermally-induced IMT in this sample, happening at lower critical temperature. The sig-

nificantly broader width of the IMT transition in the $\text{VO}_2/\text{Al}_2\text{O}_3$ sample implies a broader distribution[34] of the metallic nucleation cluster sizes compared to VO_2/TiO_2 samples, as the connection between the width of the thermally-induced IMT and the structure of the film have been demonstrated previously.[41, 34, 36, 58]

These structural differences may also play a critical role in explaining the observed differences in temperature dependence of the full IMT threshold $\Phi_{full-MIT}$ for the two samples. The absence of a temperature sensitivity in $\Phi_{full-MIT}$ for the VO_2/TiO_2 sample indicates that once the critical density of the photo-electrons is reached, the whole film undergoes the IMT uniformly, independently of its original temperature. While there is no direct proof, this observation is consistent with a more strained and more ordered monocrystalline structure in this sample, as well as a sharper thermally-induced IMT transition. In contrast, the less ordered structure of the $\text{VO}_2/\text{Al}_2\text{O}_3$ sample may give rise to stronger local variations of the critical temperature throughout the sample (as indicated by a much wider thermally-induced IMT transition). This non-uniformity can then be responsible for stronger local variations in the critical density of particle-hole excitations necessary to induce the coherent lattice distortion and drive the structural transition, resulting in a temperature dependent critical density of electron-hole excitations necessary to drive the full IMT in the whole sample.

We can estimate the minimum pump fluence values required to excite the critical density of photoelectrons to match the free electron density in the metallic phase of the VO_2 film in equilibrium (above the critical temperature). First, we estimate the electron density in the metallic VO_2 films from the measured dc electrical conductivity, using the Drude-Smith model[59]:

$$\sigma_{DC} = \frac{ne^2\tau_{DS}}{m^*} \times (1 + c) \quad (5.1)$$

where n is the electron density, τ_{DS} is the scattering time, m^* is the effective mass of

the electrons, and c is the correlation parameter, such that $c = 0$ corresponds to free Drude electrons, and $c = -1$ corresponds to fully localized electrons. Using the previously established values for τ_{DS} , m , and c , [59] the estimated value of electron densities are $3.2 \times 10^{21} \text{cm}^{-3}$ for the VO_2/TiO_2 sample, and $2.35 \times 10^{21} \text{cm}^{-3}$ for the $\text{VO}_2/\text{Al}_2\text{O}_3$ sample.

Second, we approximate the number of photo-electrons by the number of photons absorbed; although in this way we clearly overestimate the photoelectron density, this approach provides order of magnitude estimates of the required fluences. Following a similar procedure, described in Ref.[9], we compute the values of the IMT thresholds Φ_{MIT} and $\Phi_{full-MIT}$ based on reaching critical density of photoelectrons at the front of the film (using full pump laser fluence) and in the back of the film (using the attenuated pump laser fluence due to reflection and absorption inside the film). Using the measured values of the penetration depth of the 800-nm optical beam, we estimated the threshold fluence needed to photo-excite the metallic electron density at the front of the VO_2/TiO_2 film to be approximately 10 mJ/cm^2 , and the fluence required to excite the metallic electron density at the back of the film to be 36 mJ/cm^2 . These values are shown as dashed horizontal lines in Fig. 5.3(a). The higher threshold matches the boundary measured for the full metal-insulator transition. Analogous calculations for the VO_2 film on Al_2O_3 lead to threshold fluence values of 9.3 mJ/cm^2 and 21 mJ/cm^2 , respectively. We can see that for Al_2O_3 both thresholds obtained in this way do not match the Φ_{MIT} and $\Phi_{full-MIT}$ thresholds obtained experimentally. This could explain why we see no temperature dependence for $\Phi_{full-MIT}$ for the VO_2 film on TiO_2 , and why we do see one for the VO_2 film on Al_2O_3 . For the film on TiO_2 , the lattice is strained and is already much closer to the R- VO_2 lattice, meaning the energy to trigger a structural transition (which is correlated to the temperature of the film) is lower than the energy needed to pump enough electrons to get the metallic electron density. The energy needed pump the VO_2 film on Al_2O_3 to the full IMT exceeds the energy to achieve the metallic electron density, suggesting additional energy is needed

to pump the lattice, and therefor has a temperature dependence.

Finally, we roughly estimated the minimum pump fluence values required to heat the VO₂ films up to the thermally-induced phase transition, assuming that all the absorbed optical energy can eventually be transferred to heating the sample. The two solid lines in Fig. 5.3 are due to the finite width of the MIT, as can be seen in Table 5.1. The lower solid lines correspond to the minimum pump fluence required to increase the sample temperature to the beginning stage of the thermally-induced IMT (specifically to T=305 K for the VO₂/TiO₂ sample, and T_c = 325 K for the VO₂/Al₂O₃ sample). The upper lines assumed that the samples reached the fully metallic phase at T=315 K and T=355 K respectively, and we included the latent heat required for the phase transition. In these estimates we used the value of heat capacity of the VO₂ film to be 3.0 J/cm³ K, and the latent heat of 235 J/cm³. [60] For both films we find that the experimental Φ_{MIT} threshold matches semi-quantitatively the threshold obtained by estimating the value of the fluence needed to raise the temperature of the VO₂ film to T_c.

5.4 Conclusion

In conclusion, we have investigated the role of substrate-induced microstructure on the ultrafast dynamics of the photoinduced metal-insulator transition in VO₂ films, using optical pump-probe techniques. In particular, we have identified the characteristic patterns of the IMT dynamics that depend on pump laser energy and the temperature of the film, and measured the threshold pump fluence values that characterize the onset and full IMT between such behaviors. We found that two VO₂ samples - one grown on sapphire substrate, and the other grown on rutile substrate, require rather similar threshold laser fluence values, despite a rather significant (30 K) difference in the critical temperature for the thermally-induced MIT. We also identified several important differences, summarized in Table 5.1. In particular, for the VO₂ film on TiO₂ we found almost no temperature

	Film grown on TiO ₂	Film grown on Al ₂ O ₃
Average VO ₂ grain size (from XRD)	Out of plane: >13 nm	Out of plane: 45 nm
VO ₂ film thickness	110 nm	80 nm
Thermal Transition Temperature T _c	310 K	340 K
IMT width ΔT_c	9 K	26 K
DC Conductivity	at 297 K 7.01×10^3 at 340 K 3.03×10^5	at 296K 1.71×10^2 at 369 K 2.24×10^5
Penetration depth at 800 nm	255 nm	294 nm
Slowgrowth threshold fluence Φ_{MIT}	1.2 mJ/cm ² at 300 K 4.2 mJ/cm ² at 250 K 13.3 mJ/cm ² at 190 K	6.1 mJ/cm ² at 300 K 10.6 mJ/cm ² at 250 K 16.7 mJ/cm ² at 200 K
Pump fluence required induce the full transition	27.8 mJ/cm ² at 300 K 33.4 mJ/cm ² at 250 K 32.4 mJ/cm ² at 190 K	31.9 mJ/cm ² at 300 K 37.4 mJ/cm ² at 250 K 37.9 mJ/cm ² at 190 K
Semi-metallic stage emergence conditions	8.5 mJ/cm ² at 220 K	12 mJ/cm ² at 250 K

TABLE 5.1: Summary of basic properties of the two VO₂ samples.

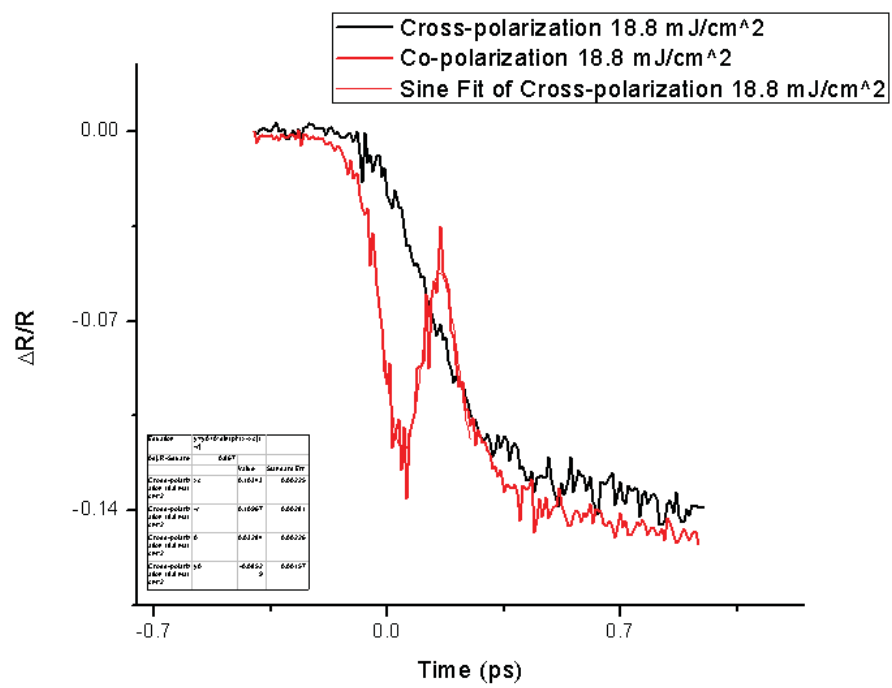
dependence in the values of fluence threshold for the full MIT, while for the VO₂/Al₂O₃ sample this threshold clearly decreased as T approaches T_c. This difference may be linked to the large lattice strain and differences in width of the thermo-induced transition, which we suspect are linked to the variance of the grain size of the film. Understanding the changes in the transition dynamics of films on difference substrates will potentially allow for the selection of desirable traits in the MIT, which is important for future VO₂-based technologies.

CHAPTER 6

VO₂ sub-picosecond polarization dependent response

6.1 Sub-picosecond response

In all other experimental results presented here, I've used orthogonal linear polarizations for pump and probe pulses. However, we also discovered that right after the pump pulse hits VO₂, $\Delta R/R$ shows an interesting response depending on the relative orientation of the polarization of the pulses: when the probe and the pump have the same polarization, a transient feature emerges with a width of ~ 200 fs immediately after the IMT has been induced. This is independent of the orientation of the films in relation to the polarization of the pump and probe. We have seen this both on the films grown on Al₂O₃ and TiO₂. Figure 6.1 shows this sub-ps feature, as measured with the VO₂ on TiO₂. As can be seen, when we have the two beams cross-polarized we see an expected drop in the reflected signal at a timescale proportional to the duration of the pump pulse, and with no sub-ps feature. When the two beams' polarizations are parallel the sub-ps feature occurs during



the pump pulse's interaction time with the sample. However, the duration of the feature does not scale with the duration of the pump (Δt). For shorter Δt , the feature becomes more difficult to see, as the underlying response to the pump cuts off the sub-ps feature. This behavior will be discussed in detail in Sec. 6.2. There is currently no observation of this in the existing literature, to the best of our knowledge.

The obvious first thought is that we are seeing an interference pattern from reflections off the back of the samples. A few things lead us to believe this is not the case. The pump and probe come at the sample from two different directions; the majority of the pump is reflected in a different direction and spatially filtered such that no residual signal from the pump reaches the photodetector. We also see that the presence of the feature is related to the IMT, since the feature disappears when we do a pump-probe measurement with the film heated to the metallic state, as seen in Figure 6.2.

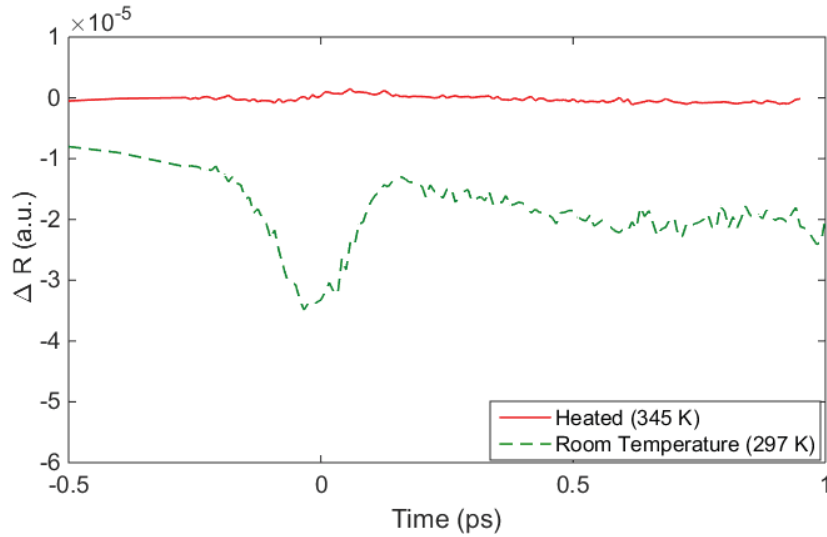


FIG. 6.2: These measurements were taken with a pump power of 11 mJ/cm^2 , and a pulse durations of 520 fs, with both the pump and probe p-polarized. When heated, there is no longer a long term change in $\Delta R/R$, and the feature is no longer present.

There are two plausible explanations for this dip in reflectivity that we are seeing: we could be seeing a strong oscillation from the lattice, or there could be a plasmonic response

in the film. The lack of dependence on the lattice orientation would suggest that it is a plasmonic response. Assuming that we are seeing an oscillation, the fitted frequency is 3.8 ± 0.3 THz, which is below the energy of any of the Raman modes we measured in Chapter 3. We have tried several different methods to determine which of these mechanisms is happening in our VO₂ thin films. First we tried applying a strong magnetic field on the films while performing the pump-probe. We then investigated changing the polarization of the incoming beams. Finally, we got the most interesting results in looking at changing the pulse duration (Δt) of the incoming pulses.

6.2 Changing pulse duration (Δt)

The most enlightening experiment to examine this phenomenon was to change the pulse duration of our beams. This was easily achieved by adjusting the compression of the pulse within our amplifier. Δt was measured with the autocorrelator, as described in Chapter 4. We took a series of measurements from 130 fs to 1 ps, where at each orientation we measured the trace with co-polarized light and cross-polarized light.

On the left column of Figure 6.3, we see both the cross-polarized measurements and the co-polarized measurements. The right column shows the cross-polarized measurement subtracted from the co-polarized measurement. Figure 6.3 shows that as we increase pulse duration Δt the cross-polarized response in the sub-ps regime extends proportionally. But when we look at the co-polarized measurements, while the underlying response is the same as the cross-polarized response, the sub-ps feature is unchanged as Δt changes. This is further highlighted in the right column of graphs, which shows the difference between the two traces and only the sub-ps feature remains. To the eye, the feature looks the same for all pulse durations, and this is confirmed by fitting them with sinusoidal wave. If we assume this is half of an oscillation, the fit gives us a frequency of 3.8 ± 0.3 THz, as can be seen in figure 6.4.

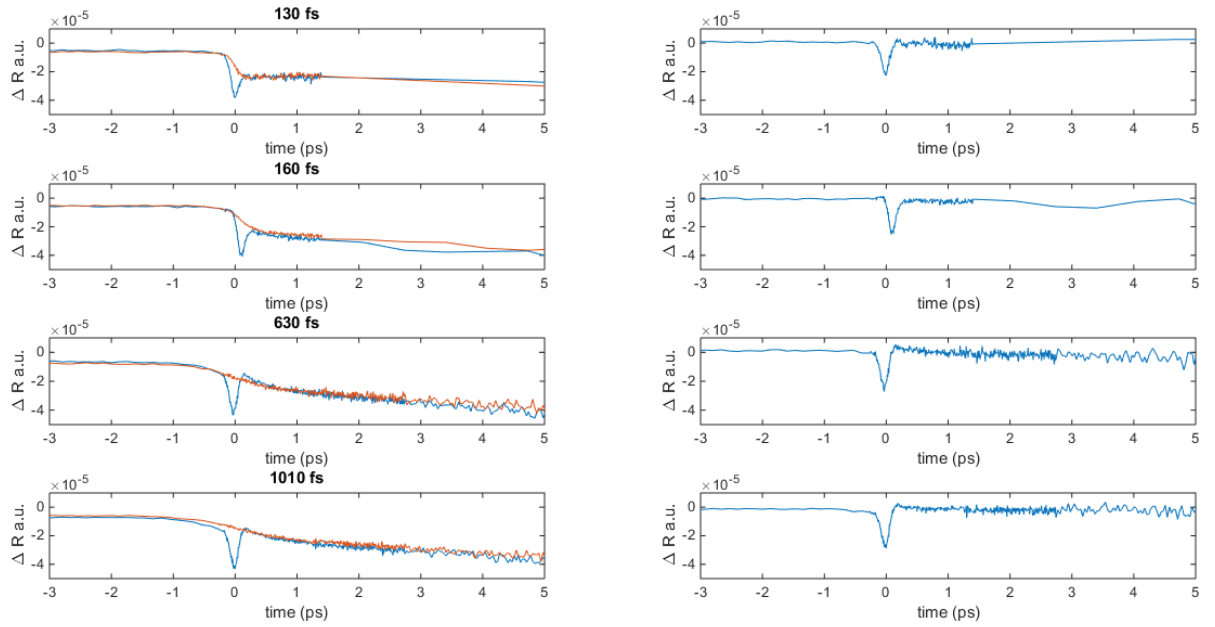


FIG. 6.3: Here are a series of measurements of VO₂ in the pump-probe configuration. The pulse length (as measured with an autocorrelator) goes from 130 fs to 1 ps. The length in the pulse changes how quickly the film responds when the pump and the probe have the same polarization. However, when the pump and probe are cross-polarized there is a ~ 100 fs feature that does not depend on the pulse length.

Similar measurements were done on our VO_2 sample on TiO_2 . Again, the feature seems to stay pretty consistent when changing other parameters. As seen in figure 6.4, the feature on the TiO_2 sample is broader than the feature on the Al_2O_3 sample, with a frequency of 2.9 ± 0.1 THz.

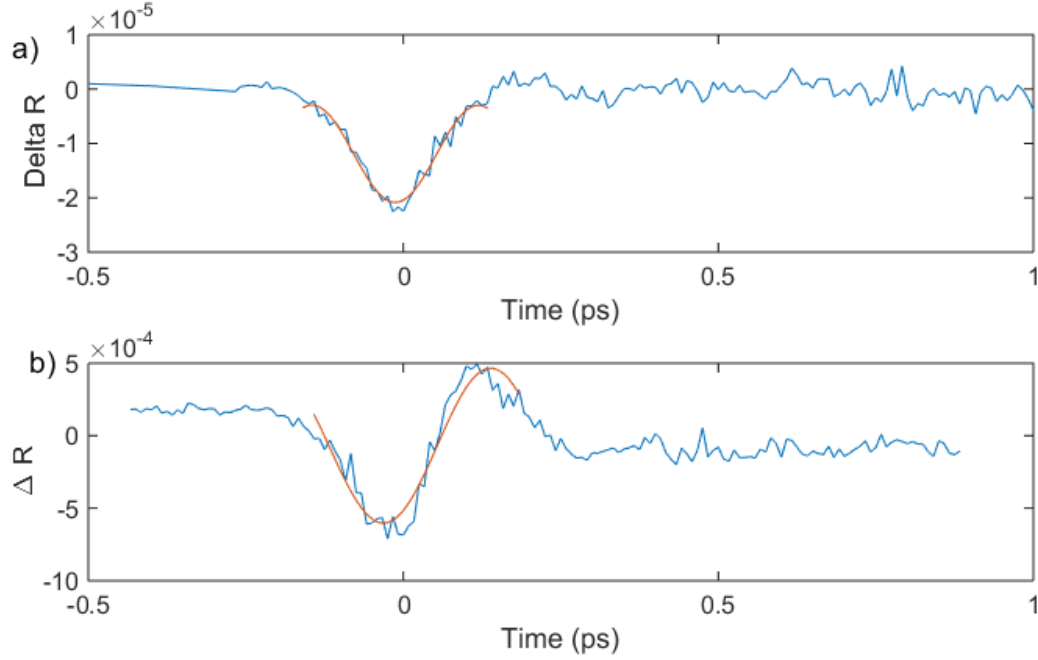


FIG. 6.4: This graph shows the same feature on the film on a) $\text{VO}_2/\text{Al}_2\text{O}_3$ and VO_2/TiO_2 , with a sinusoidal fit. Both films have a similar frequency when fitted.

The other parameter we explored is the intensity of the pump pulse. Figure 6.5 a) shows how the feature gets deeper as we increase the intensity of the pump. The relationship is linear, even when we start to get the fluences where $\Delta R/R$ starts to saturate, around $30 \text{ mJ}/\text{cm}^2$, reaching the fully metallic state after $\lesssim 5$ ps.

6.3 Electro-Magnetic Field

I used a GMW Dipole electric magnet, to produce a magnetic field. The strength of the magnetic field produced is dependent on the current and the geometry of the poles of the

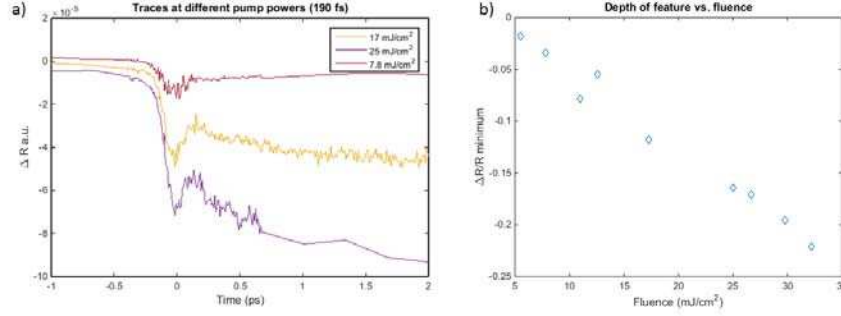


FIG. 6.5: This graph shows the relationship between the intensity of the pump, and the depth of the sub-ps feature. a) Shows the measurement for three different fluences, and one can see a decrease in $\Delta R/R$ for the higher fluence. b) shows the peak of sub-ps feature as a relationship with the fluence.

electromagnet(size of pole ends and separation). Because of the mount we used for the film, we had a separation of 4 cm, which limited the magnetic field we were capable of getting. Another limitation of the setup is the amount of current that we could safely put into the system. We used air to cool the magnet, meaning that we could only safely go up to 2 Amps. With these limitations, the system was operating in the range of 0-1 kGauss.

I first looked at the heat-induced insulator-metal transition with a magnetic field, but there was no difference between having the magnetic field on or off with any of the films. Unsurprisingly, there was also no difference between having a magnetic field on the sample for the pump-probe measurements as well, neither in the sub-ps scale, nor on the long term.

There are a couple different reasons that the magnetic field had no noticeable effect on $\Delta R/R$. First of all, the magnetic fields we used were very small compared to the field strength needed to displace the electrons, due to the configuration we chose, and the cooling method we used. In addition to that, the orientation of the magnetic field with respect to the surface was not ideal if we wished to have an effect on a plasmonic resonance. The E-field of the incident beam is parallel to the surface for p-polarized light.

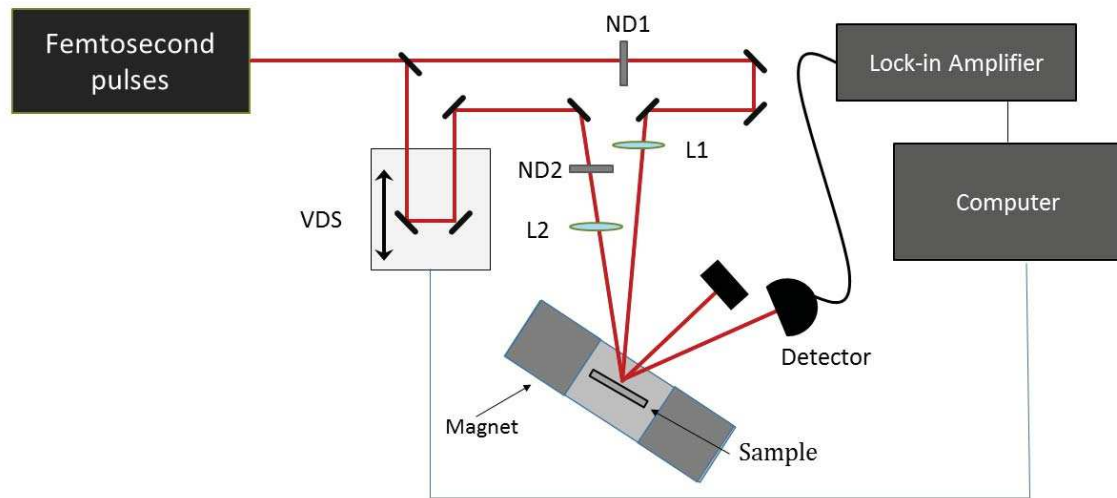


FIG. 6.6: The experimental set up we used for these measurements were much the same as the basic pump-probe measurements, except the sample was not mounted in a cryostat, and there is an electromagnet that creates a magnetic field parallel to the sample surface.

Because the light was near-incident, s-polarized will also have most of the E-field parallel to the surface of the film. If the magnetic field is to have an impact on the motion of the electrons, from maxwell's equations it needs to be orthogonal to the E-field displacing the electrons.

6.4 Analysis and Conclusion

We are confident that what we are observing is a real phenomenon, even if we do not yet have a definitive explanation of the mechanism behind it. The magnetic field experiments certainly need a higher magnetic field.

If we look at the timing of the feature, it is not surprising, but it is interesting that our two samples, VO_2 on TiO_2 and VO_2 have features with different widths. It is tempting to ascribe them to phonon modes, but they both fall a bit short in energy to any of the known Raman and IR modes. Another argument against the sub-ps feature being a phonon oscillation is the scaling in intensity with the fluence of the pump. I would expect there to be an increase in the restoring force for the ions as we increase the oscillation amplitude, there should be a leveling off of the intensity of the sub-ps feature and eventual saturation.

Another argument that we are seeing a plasmonic response is that we see this phenomenon both in the more highly crystalline TiO_2 sample and in the more granular Al_2O_3 sample. We are far more likely to see a coherent crystalline response in the TiO_2 sample because it is monocrystalline. In addition to that, we have seen no preference for how the film is oriented with relation to the polarization of the beams. What matters is the relative polarization of the pump and the probe.

While theses results are inconclusive, we do believe we are seeing a real phenomenon, and they warrant further study. If we can isolate the control of this feature, it opens up possibilities for ultrafast switches that can recover back to the insulating state as fast as

it can be triggered to the metallic state.

CHAPTER 7

Effect of inhomogeneities and substrate on the recovery dynamics of the metal-insulator transition in VO₂ thin films

7.1 Introduction

Several works [33, 61, 13, 9, 62, 63, 64, 12, 65, 66] have investigated the short timescale dynamics after the photo-induced transition. In particular, Ref. [67] presented a comparison of the long timescale recovery dynamics between VO₂ films on a crystal substrate or a glass substrate and found that the recovery time for the films on the glass substrate was much longer than for the films on a crystal substrate. The recovery time was modeled using the heat equation to describe the heat flow across the interface between the VO₂ film and the substrate. The difference in the characteristic time between the two types of

substrates was attributed to the fact that the thermal conductivity of the interface was expected to be much smaller for glass substrates than for crystal substrates.

In this chapter, we present a theory, which was developed by Martin Rodriguez-Vega, to properly take into account the effect of inhomogeneities on the recovery dynamics of VO₂ films. This theory describes simultaneously: (i) the profile of the reflectivity across a thermal induced MIT; (ii) the long timescale recovery dynamics of the reflectivity after a photo-induced insulator-to-metal transition; (iii) the observed difference of two orders of magnitude between samples with different substrates.

The presence of inhomogeneities induces a distribution of values for the transition temperature T_c within the film. To take this into account a generalized heat equation that includes the fact that during the recovery from the photo-induced insulator-to-metal transition, at any given time a fraction of the sample is undergoing the metal-to-insulator transition was derived, where another fraction is still cooling in the metallic phase, and another fraction is already cooling in the insulating phase. A key ingredient of the generalized heat equation is the correct description of the time evolution of the fraction of the sample that is metallic, insulating, or undergoing the phase transition. We then use our theoretical model to obtain the scaling relation between the characteristic recovery time τ and the parameters of the films. Our theoretical model, and the underlying assumptions, are strongly supported by our experimental results. Differently than in Ref. [67] our VO₂ films have all crystal substrates, no glass. Yet, we find that τ can be more than two orders of magnitude different depending on the crystal substrate, TiO₂ or Al₂O₃, Fig. 7.1.

The generalized heat equation, Eqs. (7.9), which properly takes into account the effect of the films inhomogeneities on the recovery dynamics is the main result of our work. Our theory allows the description of the recovery dynamics consistently with the measurements obtained for the thermally driven MIT. The scaling between the characteristic recovery time τ and the parameters of the film is another important result of this work.

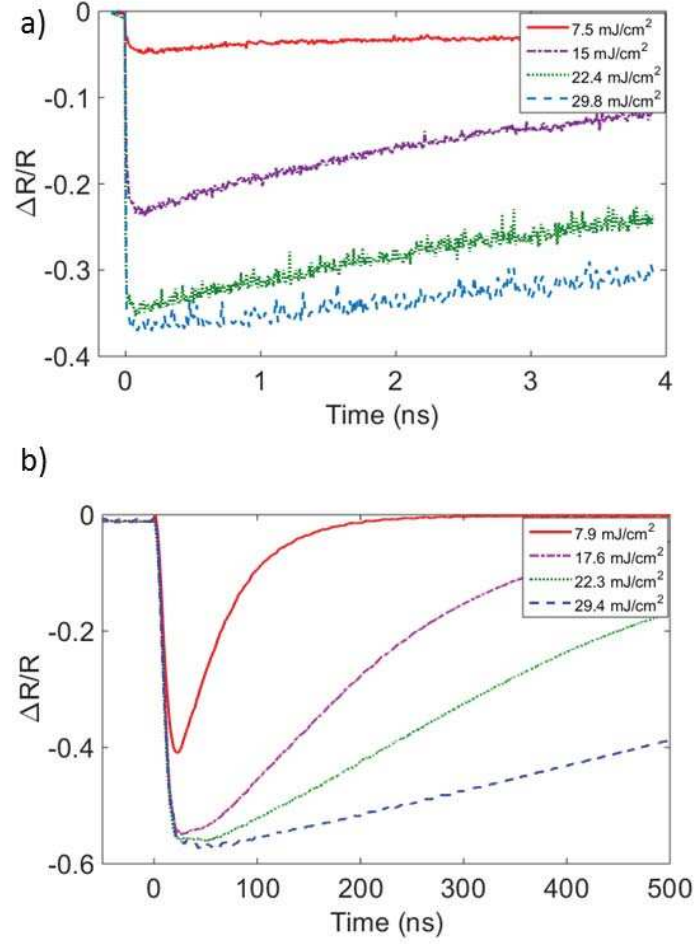


FIG. 7.1: Relative change in reflectivity ($\Delta R/R$) for the VO₂ film on (a) Al₂O₃ substrate and (b) TiO₂ substrate as a function of time after the MIT is induced at time $t = 0$ by a strong ultrafast pump pulse. The values of the pump fluence are shown in the legend, and the sample temperature is set to 311 K in (a) and 280 K in (b), which correspond to approximately 30 K below the critical temperature T_c for thermally-induced MIT for each sample.

This work is relevant to the more general problem of how spatial inhomogeneities affect a first order phase transition. The ability of our treatment to contribute to this general problem relies on the fact that in VO_2 the two phases across the first-order phase transition have very different electronic properties (metallic vs. insulating behavior) that allows us to get an accurate phase mapping, via optical reflectivity measurement, of the time evolution of the metallic (insulating) fraction and, indirectly, of the spatial inhomogeneities present during the transition.

The chapter is organized as follows. Sec. 7.2 describes the experimental arrangements to measure the optical reflectivity time-evolution, particularly for measurements done with a cw probe. The details of the theoretical model that we use to characterize the distribution of the films' inhomogeneities and the long-time dynamics of the reflectivity after a photo-induced insulator-to-metal transition are presented in Secs. 7.3 and 7.4, respectively. In Sec. 7.5 we demonstrate how the variations in statistical properties of the two films result in a significant difference in the relaxation timescales, and in Sec. 7.6 we provide our conclusions.

7.2 Experimental setup

The measurements of $\text{VO}_2/\text{Al}_2\text{O}_3$ were done with the experimental set up described in Chapter 4.

The MIT relaxation of the VO_2/TiO_2 sample was not measurable with the femtosecond probe, as its characteristic decay time exceeded the 4 ns maximum pulse separation, determined by the length of the delay stage. To measure the relaxation of the metallic VO_2 grown on the rutile sample we modified our experimental setup by replacing the femtosecond probe pulses with a continuous-wave (CW) diode laser operating at 785 nm and a fast photodiode (measured response time of approximately 10 ns), as shown in Fig. 7.2.

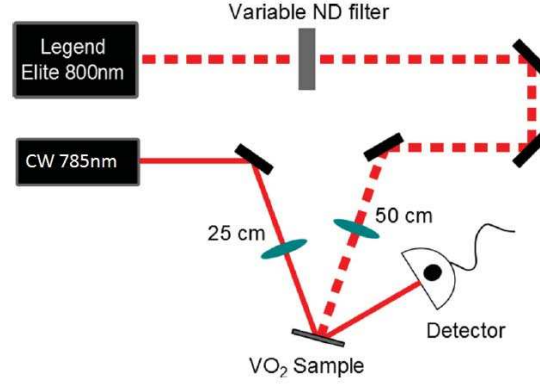


FIG. 7.2: Schematic of the experimental setup using a continuous-wave probe laser.

This detection method allowed us to measure changes in reflectivity for times longer than ≈ 20 ns after the insulator-to-metal transition, that were inaccessible with the femtosecond probe arrangement.

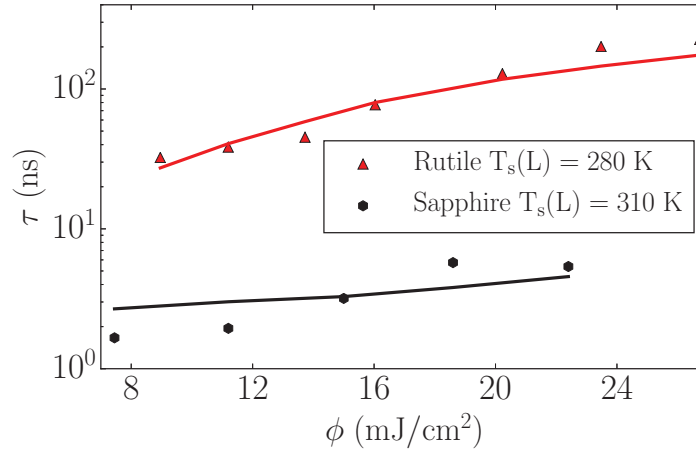


FIG. 7.3: Dependence of metal state decay constant τ on the laser pump fluence and substrate temperature. Dots represent experimental data, and lines corresponds to the results of the theoretical calculations. The initial temperature T_s for both sample substrates was approximately 30 K below their respective MIT critical temperatures.

Figure 7.1 shows sample measurements of both the VO₂/Al₂O₃ and VO₂/TiO₂ films, using the femtosecond and CW probe arrangements respectively. The overall reflectivity depends on the refractive index of both the film and the substrate, and the refractive indices

of TiO_2 and Al_2O_3 are different. Because it is easier to average the CW laser reflection signal, the curves for VO_2/TiO_2 are smoother than the curves for the $\text{VO}_2/\text{Al}_2\text{O}_3$. The rutile reflection spectra recorded using the ultrafast probe had the same noise level as the sapphire samples, indicating that the differences in noise are due to differences in the probes, not in the samples.

For values of the pump fluence higher than a threshold, which depends on the substrate temperature, we can see that the reflectivity, soon after the pump pulse, remains almost constant for some time, i.e. its dynamics exhibits a “flat” region, see in particular Fig. 7.1 (b). The observed “flattening” of the curves is due to the pump pulse heating the sample to a temperature above the threshold value for the thermally-induced insulator-to-metal transition [12, 66]. In this case the reflectivity stays unchanged at the level corresponding to a fully metallic phase until a non-negligible fraction of the sample cools down to the transition temperature. For all experimental curves only the later exponential part of the measured reflectivity was included into the fitting thermal relaxation time analysis.

The analysis of the relative reflectivity for both VO_2 samples demonstrate that after the initial rapid change during the ultra-fast insulator-to-metal transition, its time evolution during the recovery is well fitted by a single exponential function with a recovery time constant τ :

$$R_{\text{fit}}(t) = R_I + (R_0 - R_I) e^{-t/\tau}, \quad (7.1)$$

where R_I corresponds to the reflectivity in the insulating phase, and R_0 corresponds to the reflectivity at $t = 0$ s. The results of such measurements are shown in Fig. 7.3: for $\text{VO}_2/\text{Al}_2\text{O}_3$ films we obtained values of τ of the order of few nanoseconds, whereas it took the VO_2/TiO_2 sample a few hundred nanoseconds to relax back to the insulating state. These two orders of magnitude difference in the recovery times were even more surprising

considering that the characteristic times for the transition itself were quite similar, as demonstrated in Chapter 5. In the discussion below we demonstrate that the relaxation dynamics strongly depend on the microstructure of the VO₂ films which in turn is strongly influenced by the properties of the substrate and their interface. Figure 7.3 also reveals that the rate of thermal relaxation for both samples increases with higher pump power.

7.3 Theoretical modeling of inhomogeneities

The theory in this section was developed by Martin Rodriguez-Vega [68] and is included here for a complete description of this experiment. In order to take into account the effect of the inhomogeneities on the MIT dynamics the first step is to characterize them. To do this we can use the profile of the reflectivity across the thermally induced MIT. The dotted lines in Figures 7.4 (a), and (b) show the measured reflectivity as a function of temperature across the thermally induced MIT for a VO₂ film grown on sapphire and TiO₂, respectively. The temperature driven MIT in VO₂ is a first-order transition. In the ideal case the reflectivity is expected to exhibit a finite, step-like, change at the critical temperature T_c , at which the sample goes from a low-temperature insulating state to a high-temperature metallic state. In thin films, however, the optical reflectivity smoothly changes from the value corresponding to the insulating phase (R_I) to the value characteristic to the metallic phase (R_M) as the temperature increases, as Fig. 7.4 illustrates. For our samples the hysteresis loop is very narrow [41]. The fact that the MIT takes place over a range of temperatures implies that different regions of the sample have different values of T_c . This is different from the case of an ideal, homogeneous, system for which the whole sample exhibits the coexistence of metallic and insulating regions only for $T = T_c$. As a consequence the MIT in the films is characterized not by a single critical temperature but by a distribution $P(T_c)$ of critical temperatures. This is due to the fact that the VO₂ films are inhomogeneous: they are formed by crystal grains with different local

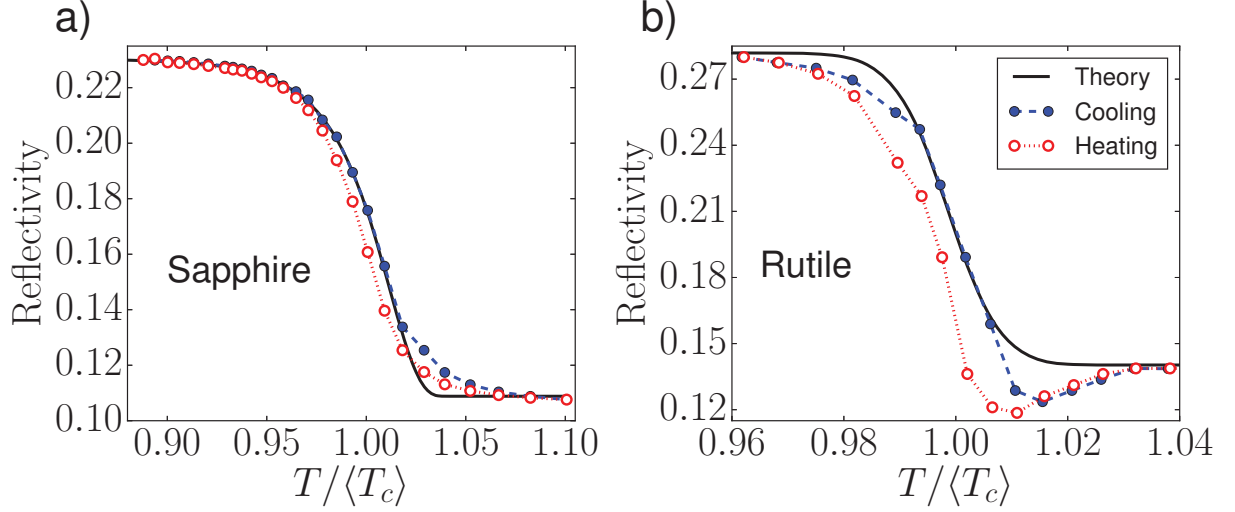


FIG. 7.4: Evolution of the reflectivity across the thermally induced MIT for the case of sapphire and rutile substrates normalized to the average critical transition temperature. The open circles (red) correspond to the measured reflectivity in the heating branch, the solid circles (blue) correspond to the measured reflectivity in the cooling branch, and the solid curve corresponds to the theoretical result. For rutile substrate $\langle T_c \rangle = 314.0$ K, and for the sapphire substrate $\langle T_c \rangle = 340.1$ K.

properties. Different grains in general have different sizes, slightly different stoichiometry, and experience different amounts of local strain. It is very challenging to characterize the distribution of all the local properties that can affect the transition temperature of each grain. However, for our purposes, we only need $P(T_c)$ and, as we show below, this can be obtained directly from the profiles of $R(T)$ without having to characterize the distribution of the local properties affecting T_c . Let η_I be the fraction of the sample in the insulating phase. At a given temperature T we have:

$$\eta_I(T) = \int_T^\infty P(T_c) dT_c. \quad (7.2)$$

Let $\eta_m(T) = 1 - \eta_I(T)$ be the fraction of the film in the metallic phase. To obtain the evolution of $\eta_I(T)$ across the MIT, and therefore $P(T_c)$, considering that changes in the fraction of the film that is metallic (insulating) are the dominant cause of changes in the

reflectivity, we can use a two-fluid effective medium theory (EMT) [69, 70, 71, 72]. In the EMT an inhomogeneous system is replaced by an effective homogeneous medium having the same, bulk, electric properties. Let ϵ_M , ϵ_I be the dielectric constants (at the probing frequency) of VO₂ in the metallic and insulating phase respectively. Then, the dielectric constant of the effective medium, ϵ_{EMT} , is given by the following equation:

$$\frac{\eta_I(\epsilon_I - \epsilon_{EMT})}{\epsilon_{EMT} + g(\epsilon_I - \epsilon_{EMT})} + \frac{\eta_M(\epsilon_M - \epsilon_{EMT})}{\epsilon_{EMT} + g(\epsilon_M - \epsilon_{EMT})} = 0. \quad (7.3)$$

In Eq. (7.3) g is a factor that depends on the shape of the grain. Without loss of generality we set $g = 1/3$. Let n and k be the real and imaginary parts respectively of the index of refraction, so that for the effective medium $n + ik = \sqrt{\epsilon_{EMT}}$ and therefore

$$R = \left| \frac{\cos \theta_0 - \sqrt{(n + ik)^2 - \sin^2 \theta_0}}{\cos \theta_0 + \sqrt{(n + ik)^2 - \sin^2 \theta_0}} \right|^2, \quad (7.4)$$

where $\theta_0 \approx 15^\circ$ corresponds to the probe incidence angle. Given our experimental setup we can reliably obtain the imaginary part of the index of refraction by measuring the absorption. For this reason we set the value of the imaginary part of the complex index of refraction k_M , (k_I) for the metallic and (insulating) phase to the measured values, consistent with the values reported in the literature [3, 73], and then use Eq. (7.4) and the measured value of R_M (R_I) in the metallic (insulating) phase to fix the corresponding value of n_M (n_I) (see Table 7.1).

Using Eqs. (7.2)-(7.4) we can obtain the profile of $R(T)$ across the MIT for a given $P(T_c)$. Assuming $P(T_c)$ to be a Gaussian distribution, by fitting the measured profile of $R(T)$ to the one obtained using Eqs. 7.2-7.4 we can obtain the average value of the critical temperature $\langle T_c \rangle$ and its standard deviation σ_{T_c} . For VO₂/TiO₂ samples we find $\langle T_c \rangle = 314$ K, $\sigma_{T_c} = 2.6$ K, for VO₂/Al₂O₃ samples $\langle T_c \rangle = 340$ K, $\sigma_{T_c} = 8.8$ K. The solid

lines in Fig. 7.4 show the profiles of $R(T)$ obtained using Eqs. (7.2)-(7.4) and the above values for $\langle T_c \rangle$ and σ_{T_c} .

The difference in the value of T_c between VO_2/TiO_2 and $\text{VO}_2/\text{Al}_2\text{O}_3$ samples can be attributed to the fact that TiO_2 , having a rutile structure, might induce strain into the VO_2 film that should favor the metallic phase of VO_2 , as mentioned in Chapter 3. In general, strain effects are expected to play an important role in the physics of the MIT phase transition of VO_2 films. In our approach such effects enter indirectly, via the form of the probability distribution $P(T_c)$, and the value of the thermal conductivity of the interface between the VO_2 film and the substrate.

As we discuss in the following section, for our theoretical treatment of the recovery dynamics over long timescales of VO_2 films the knowledge of $P(T_c)$, i.e., $\langle T_c \rangle$ and σ_{T_c} , is all that is needed. As mentioned before the fact that σ_{T_c} is nonzero is due to inhomogeneities, of different nature, present in the VO_2 film. It is practically impossible to know the distribution in the films of the properties affecting T_c . However, it is interesting to consider the limit in which the grain size D is the dominant property affecting T_c . The reason is that in this limit it is possible to extract, using strong and fundamental arguments, the distribution, $P(D)$, for the grain size. In particular, it is possible to obtain the average grain size, $\langle D \rangle$, and its standard deviation, quantities that are of great practical interest. $\langle D \rangle$ can be compared to estimates obtained using more direct experimental techniques, such as XRD. In the remainder of this section we use the experimental results for $R(T)$ across the MIT to extract $\langle D \rangle$ and its standard deviation.

Theoretical and experimental evidence[74] indicates that for thin films the distribution $P(D)$ of the grain size D typically follows a logarithmic-normal distribution,

$$P(D) = \frac{1}{\sqrt{2\pi}\sigma D} \exp \left[-\frac{\left[\ln D / \hat{D} \right]^2}{2\sigma^2} \right]. \quad (7.5)$$

In Eq. (7.5) D is the effective diameter of a grain, \hat{D} is the grain size (diameter) such that $\ln \hat{D} = \langle \ln D \rangle$, and σ is the standard deviation of $\ln(D)$.

From general and fundamental arguments [75, 76, 77, 78] we have:

$$T_c = T_c^{(\text{bulk})} \left(1 - \frac{1}{D/D_0} \right), \quad (7.6)$$

where $T_c^{(\text{bulk})}$ is the bulk transition temperature and D_0 , equal to 2 nm in our case, is the grain's diameter below which the grain is so small that is not possible to unambiguously identify its crystal structure. We set $T_c^{(\text{bulk})} = 355$ K, that is the temperature above which the $\text{VO}_2/\text{Al}_2\text{O}_3$ samples is completely metallic. This value is higher than the value of bulk VO_2 due to the strain experienced by the films [58, 34]. The relation between $P(D)$ and $P(T_c)$ is given by:

$$P(T_c) = P(D(T_c)) \frac{dD}{dT_c}. \quad (7.7)$$

Using Eqs. (7.2)-(7.7), by fitting the measured profile of $R(T)$ across the MIT, we can obtain $P(D)$ and therefore $\langle D \rangle$ and its standard deviation. Figures 7.5 (a), (b) show the profiles of $P(D)$ used to obtain a good theoretical fit to the evolution of $R(T)$ shown in Fig. 7.4. These profiles correspond to $\langle D \rangle = 64.7$ nm $\sigma_D = 38.5$ nm for $\text{VO}_2/\text{Al}_2\text{O}_3$ samples, and $\langle D \rangle = 17.4$ nm $\sigma_D = 1.1$ nm VO_2/TiO_2 samples. It is interesting to compare the values of $\langle D \rangle$ obtained using this approach to the values estimated using XRD. From XRD data [66] we estimated $\langle D \rangle \approx 45$ nm for $\text{VO}_2/\text{Al}_2\text{O}_3$ and $\langle D \rangle \approx 13$ nm for VO_2/TiO_2 (see Table 7.1). These values are in remarkable semi-quantitative agreement with the values extracted from the profiles of $R(T)$ across the MIT suggesting that the assumption that the grain size is the dominant property affecting the local value of T_c might be qualitatively correct. It is therefore interesting to obtain the profiles of $P(T_c)$ corresponding to the distributions of grain sizes shown in Figs. 7.5 (a), (b). Such profiles are shown in

Figs. 7.5 (c), (d). The evolution of $\eta_I(T)$ across the MIT obtained using these profiles is shown in Fig. 7.6.

	VO ₂ /TiO ₂	VO ₂ /Al ₂ O ₃
$\langle T_c \rangle$	314.0 K	340.1 K
σ_{T_c}	2.6 K	8.8 K
$\langle D \rangle$	17.4 nm	64.7 nm
$\langle D \rangle_{Exp}$ [66]	13 nm	45 nm
σ_D	1.1 nm	38.5 nm
$n_M + ik_M$	$1.53 + i0.8$	$1.49 + i0.65$
R_M	0.14	0.11
$n_I + ik_I$	$3.03 + i0.57$	$2.60 + i0.60$
R_I	0.28	0.23
σ_K	1,100 W/(K cm ²)	13,000 W/(K cm ²)

TABLE 7.1: Comparative table between VO₂/TiO₂, and VO₂/Al₂O₃ sample parameters.

Our analysis suggest that the $R(T)$ profiles could be an indirect method to characterize the distribution of grain sizes in VO₂ films, a very challenging quantity to obtain using direct imaging experiments.

7.4 Theoretical modeling of the relaxation dynamics of the MIT

In our experiment the VO₂ films have a thickness d equal to or smaller than 110 nm (see Fig. 7.7), which is comparable with the laser $1/e$ penetration depth $\delta \simeq 110 - 130$ nm [66]. Thus, we can assume that the pump pulse heats the film uniformly throughout its thickness. To describe the heat transfer process between the film and the substrate, we assume the temperature to be uniform throughout the film at all times. Effectively, given these conditions, the heat transfer problem becomes a one-dimensional problem, and the equa-

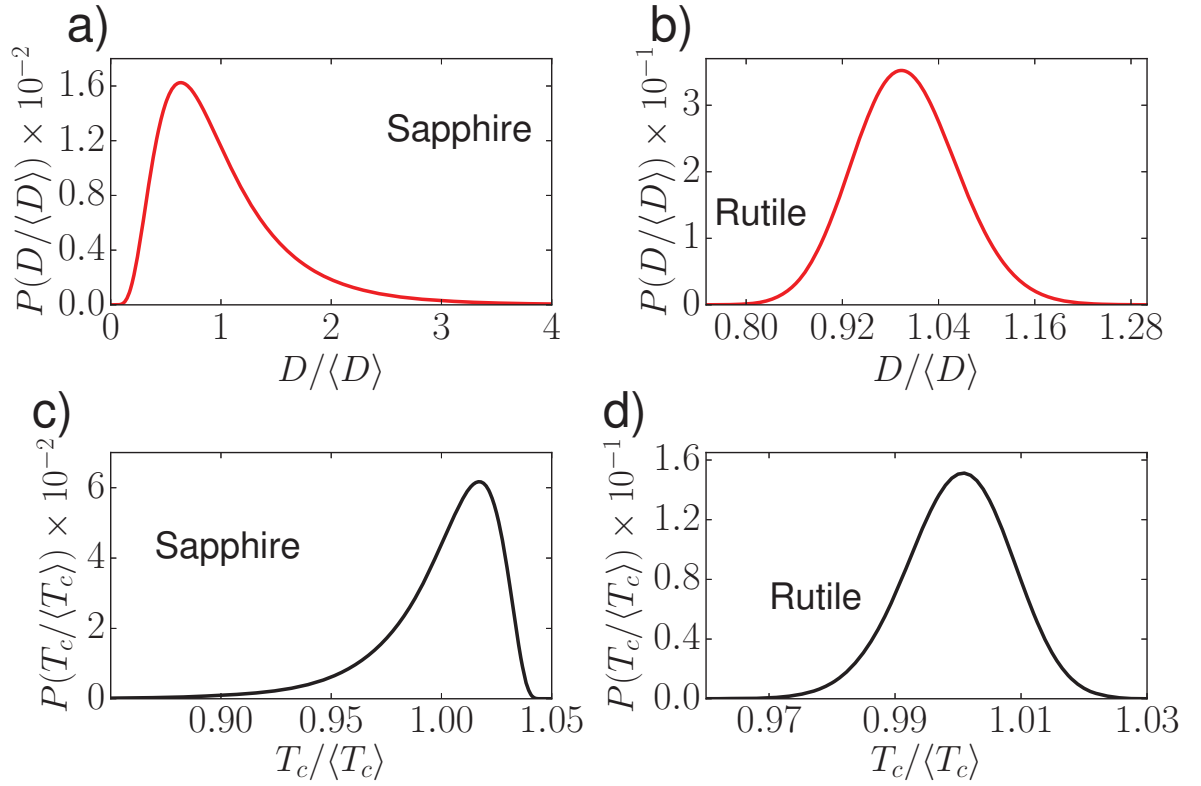


FIG. 7.5: (a) and (b) show the grain size distributions normalized to the average grain size for sapphire ($\langle D \rangle = 64.7$ nm) and rutile ($\langle D \rangle = 17.4$ nm) substrate respectively. (c) and (d) show the critical temperature distribution normalized to the average critical temperature for sapphire ($\langle T_c \rangle = 340.1$ K) and rutile ($\langle T_c \rangle = 314.0$ K) respectively. The bulk critical temperature is taken to be $T_c^{(bulk)} = 355$ K.

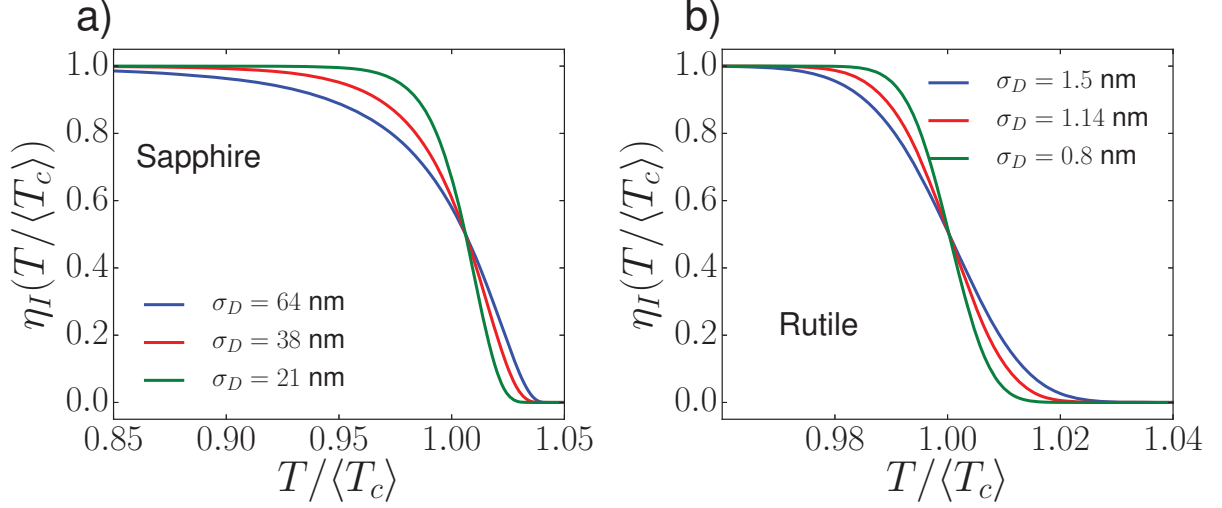


FIG. 7.6: Evolution of the insulating partial volume η_I across the thermally induced MIT for case of (a) sapphire and (b) rutile substrates. For rutile, $\langle T_c \rangle = 314.0$ K, and for sapphire $\langle T_c \rangle = 340.1$ K.

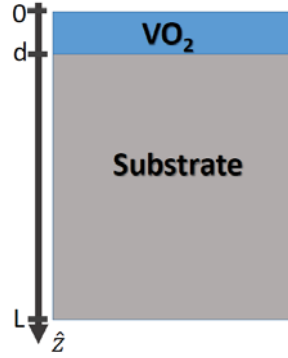


FIG. 7.7: Sketch of the heterostructure considered in this work. It is composed of a vanadium dioxide (VO_2) thin-film deposited on top of a substrate. The substrates considered in this work are titanium dioxide (TiO_2), and aluminum oxide (Al_2O_3). For VO_2/TiO_2 $d = 110$ nm while for $\text{VO}_2/\text{Al}_2\text{O}_3$ $d = 80$ nm. For both substrates, $L = 0.5$ mm.

tion for the rate of change of the heat (Q) in the film takes the form:

$$\begin{aligned} \frac{dQ}{dt} = & A \times d \times (\rho_I C_I \eta_I(T_f) + \rho_M C_M \eta_M(T_f) \\ & + L(T_f) P(T_f) \rho_{av}) \frac{\partial T_f}{\partial t} , \end{aligned} \quad (7.8)$$

where T_f is the film temperature, A is the area of the film, ρ_I (ρ_M) is the density in the insulating (metallic) phase, $\rho_{av} \equiv (\rho_I + \rho_M)/2$, C_I (C_M) is the heat capacity in the insulating (metallic) phase, L is the specific heat and $P(T_f)dT_f$ is the fraction of the sample undergoing the MIT in the time interval dt during which the film temperature is in the interval $[T_f, T_f + dT_f]$. Here $P(T_f)$ is the distribution of critical temperatures due to the inhomogeneities that we have obtained in the previous section. Using Eq. (7.2) and the fact that $\eta_M = (1 - \eta_I)$ we can rewrite Eq. (7.8) in a form that more explicitly shows the effect due to the inhomogeneities, i.e. the fact that the MIT is not characterized by a single T_c , but by a distribution of T_c 's:

$$\begin{aligned} \frac{dQ}{dt} = & A \times d \times \left[\rho_M C_M + (\rho_I C_I - \rho_M C_M) \int_{T_f}^{\infty} P(T_c) dT_c \right. \\ & \left. + L(T_f) P(T_f) \rho_{av} \right] \frac{\partial T_f}{\partial t} . \end{aligned} \quad (7.9)$$

Equation (7.9) is the main result of this work: it allows to properly take into account the effect of inhomogeneities on the long timescale dynamics across a first order phase transition. The key quantity entering Eq. (7.9) is the distribution $P(T_c)$ that, as we have shown in the preceding section, can be obtained from the profile of $R(T)$ across the thermally activated MIT. This work is the first to combine the information from the thermally activated MIT to obtain a physically accurate heat equation to describe the recovery dynamics after a photo-induced MIT.

For the latent heat we have [75, 76, 77]

$$L = L^{(\text{bulk})} \frac{T_c}{T_c^{(\text{bulk})}}. \quad (7.10)$$

where $L^{(\text{bulk})}$ is the value of the specific heat for bulk VO_2 . Given Eq. (7.6), Eq. (7.10) implies $L = L^{(\text{bulk})}(1 - D_0/D)$.

The rate of change of heat in the film given by Eq. (7.8) must be equal to the heat current (J_Q) across the interface between the film and the substrate:

$$J_Q = -\sigma_K A(T_f - T_s(d)) \quad (7.11)$$

where σ_K is the Kapitza constant characterizing the thermal conductivity of the interfaces [79, 80, 81, 82], and $T_s(d)$ is the temperature of the substrate at the surface facing the VO_2 film. Combining Eq. (7.9) and Eq. (7.11), for T_f we obtain the equation:

$$\begin{aligned} & \left[\rho_M C_M + (\rho_I C_I - \rho_M C_M) \int_{T_f}^{\infty} P(T_c) dT_c \right. \\ & \left. + L(T_f) P(T_f) \rho_{av} \right] \frac{\partial T_f}{\partial t} = -\frac{\sigma_K}{d} (T_f - T_s(d)). \end{aligned} \quad (7.12)$$

In Eq. (7.12) the only undetermined quantity is σ_K . We fix σ_K by fitting the theoretically obtained time evolution of $R(t)$ to the one measured experimentally, *for fixed experimental conditions* such as the temperature of the substrate and the pump fluence. The robustness of the theory presented is evidenced by the fact that, the same *fixed* value of σ_K provides a good agreement between the theoretical and the experimental results for a broad range of experimental conditions.

To completely define the problem we need to supplement Eq. (7.12) with proper boundary conditions. The temperature distribution within the substrate, $T_s(z, t)$, satisfies

the diffusion equation:

$$\frac{\partial T_s(z, t)}{\partial t} = \frac{k_s}{C_s \rho_s} \frac{\partial^2 T_s(z, t)}{\partial z^2} \quad (7.13)$$

where k_s , C_s , ρ_s are the thermal conductivity, heat capacity, and mass density, respectively, of the substrate. The bottom of the substrate, for which $z = L$ (see Fig. 7.7), is kept at a fixed temperature $T_s^{(B)}$. At the film/substrate interface the heat transferred from the film must be equal to the heat current $k_s \partial T_s / \partial z|_{z=d}$. We then have that the boundary conditions completing Eq. (7.13) are:

$$T_s(z = L, t) = T_s^{(B)}; \quad (7.14)$$

$$k_s \left. \frac{\partial T_s(z, t)}{\partial z} \right|_{z=d} = -\sigma_K (T_f(t) - T_s(z = d, t)). \quad (7.15)$$

Equations (7.10), (7.12)-(7.15), combined with knowledge of the distribution $P(T_c)$ completely define the temperature evolution of the VO₂ film. Notice that in these equations the only unknown parameter is the Kapitza constant σ_K . All the other quantities are known from direct measurements. $P(T_c)$ is obtained from the profile of $R(T)$ across the MIT, independently from the dynamics of R after the photo-induced insulator-to-metal transition. Also, the relation between the specific heat L and T is fixed by general and fundamental results [75, 76, 77].

While these equations can in general be solved only numerically, some qualitative understanding of the decay time τ can be gained if we make some simplifications. Let $P(T_c) = 1/(\sqrt{2\pi}\sigma_{T_c}) \exp\{-(T_c - \langle T_c \rangle)^2/(2\sigma_{T_c}^2)\}$. At a temperature T the insulating volume fraction is given by $\eta_I(T) = \frac{1}{2} [1 - \operatorname{erf}((T - \langle T_c \rangle)/(\sqrt{2}\sigma_{T_c}))]$. Then assuming that the pump pulse is strong enough to drive the entire film into a fully metallic state at $t = 0$, the time-dependence of the insulating volume fraction can be approximated by a simple exponential form $\eta_I(t) = 1 - Ae^{-t/\tau}$. In this case, an expression for the temperature

can be obtained through the relationship $\eta_I(T(t)) = \eta_I(t)$. Furthermore, assuming that the substrate temperature T_s does not change with time, and the latent heat L to be temperature-independent, we can calculate the decay constant τ :

$$\tau = Cd \frac{\sigma_{T_c}}{\sigma_K} \frac{(C_M \rho_M + L \rho_{av} P(T_0))}{T_0 - T_s} + \tau_0, \quad (7.16)$$

where the constants $C > 0$, and τ_0 can only be determined by solving the full system of equations (7.12)-(7.15)

It is interesting to note that despite its many limitations, Eq.(7.16) captures many important qualitative traits of the actual relaxation process. For example, Figure (7.8) shows a plot of the decay constant as a function of σ_{T_c} obtained solving the full system of equations (7.12)-(7.14) for two different values of the average critical temperature, and same initial temperature $T_0 = 360$ K. It is easy to see that the decay time τ follows the linear trend predicted by Eq. (7.16) in the limit $(T_0 - \langle T_c \rangle) \gg \sqrt{2}\sigma_{T_c}$. Similarly, an exact solution shows the inverse dependence of τ on the Kapitza constant, $\tau \propto \sigma_K^{-1}$, as shown in Figure 7.9.

The relation (7.16) is another important result of our work, it shows how the characteristic time of the recovery dynamics is related to the properties of the VO₂ films. In particular it shows the novel result that τ grows linearly with σ_{T_c} , the standard deviation of $P(T_c)$. σ_{T_c} can be reliably obtained from the profile of $R(T)$ across the MIT.

7.5 Effect of inhomogeneities on the relaxation dynamics of the photo-induced MIT

Using the theoretical approach described in Sec. 7.4 we can obtain the time evolution of the optical reflectivity R through the MIT, as well as explain the significant difference

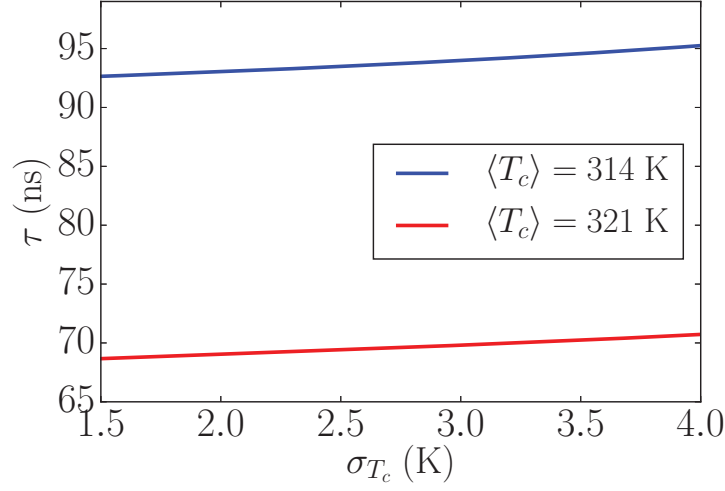


FIG. 7.8: Full numerical calculation of the dependence of metal state decay constant τ on σ_{T_c} for two different values of the sample average critical temperature $\langle T_c \rangle$, and $T_s(L) = 280$ K. The initial temperature $T_0 = 360$ K is such that the sample is initially fully metallic, and $(T_0 - \langle T_c \rangle)/(\sqrt{2}\sigma_{T_c}) \approx 9$.

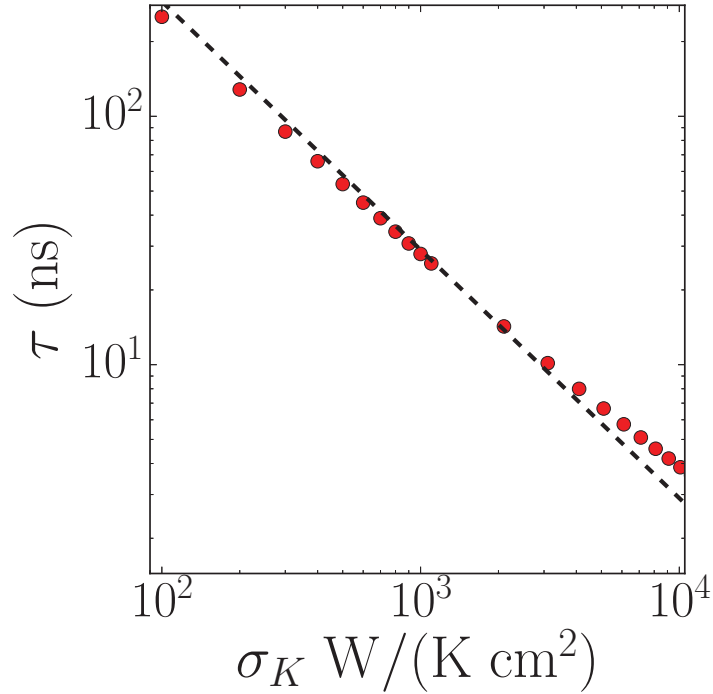


FIG. 7.9: $\text{VO}_2/\text{Al}_2\text{O}_3$ metal state decay time τ dependence on the Kapitza constant σ_k for $\langle D \rangle = 64.7$ nm, $\sigma_D = 38.5$ nm, substrate temperature $T_s(L) = 310$ K, and fluence $\phi = 8$ mJ/cm². The red dots correspond to numerical calculations, and the dashed line is given by $\tau \propto \sigma_K^{-1}$.

VO ₂ heat capacity insulating phase C_I [60]	0.656 J/(g K)
heat capacity metallic phase C_M [60]	0.78 J/(g K)
density insulating phase ρ_I [82]	4.57 g/cm ³
density metallic phase ρ_M [82]	4.65 g/cm ³
thermal conductivity insulating phase κ_I [83]	3.5 W/(m K)
thermal conductivity metallic phase κ_M [83]	6 W/(m K)
bulk latent heat $L^{(Bulk)}$ [60]	51.8 J/g
TiO ₂ heat capacity C_s [84]	0.686 J/(g K)
density ρ_s [82]	4.25 g/cm ³
thermal conductivity κ_s [85]	8 W/(m K)
Al ₂ O ₃ heat capacity C_s [86]	0.779 J/(g K)
density ρ_s [86]	3.98 g/cm ³
thermal conductivity κ_s [86]	30 W/(m K)
VO ₂ /TiO ₂ absorption coefficient at 800 nm α [66]	0.01 nm ⁻¹
VO ₂ /Al ₂ O ₃ absorption coefficient at 800 nm α [66]	0.0076 nm ⁻¹

TABLE 7.2: Parameters of VO₂ and substrates.

in relaxation timescales between the two VO₂ samples considered. In all the numerical calculations we assume C_I , ρ_I , C_M , ρ_M to be equal to the bulk values for insulating and metallic VO₂, see Table 7.2.

The initial film temperature is fixed by the pump fluence taking into account the Gaussian profile of the pulse and the fact that some of the heat is lost by the film during the time interval $[0, t_0]$ for which our analysis does not apply, $t = 0$ is time at which the pump pulse hits the VO₂ film and $t_0 = 10$ ns for VO₂/TiO₂ films and $t_0 = 0.5$ ns for VO₂/Al₂O₃ films.

As discussed in Sec. 7.4, σ_K is the only unknown parameter. For the case of VO₂/TiO₂ samples, by fitting one of the curves for the dynamics of the reflectivity, we find $\sigma_K = 1100$ W/(K cm²). We find that all experimental curves are well approximated assuming the same value for the Kapitza constant, see Fig. 7.10 (a). For the case of VO₂/Al₂O₃ the characteristic timescale of the recovery is much shorter than for VO₂/TiO₂ samples. As

discussed in Sec. 7.3 the two samples have very different inhomogeneities: σ_{T_c} is almost 4 times larger in $\text{VO}_2/\text{Al}_2\text{O}_3$ than VO_2/TiO_2 . All other things being equal, Eq. (7.16) implies, see Fig. 7.11, that τ should be larger in $\text{VO}_2/\text{Al}_2\text{O}_3$ than in VO_2/TiO_2 , the opposite of what is observed experimentally. We are then led to conclude that σ_K in $\text{VO}_2/\text{Al}_2\text{O}_3$ must be much higher than in VO_2/TiO_2 . Figure 7.12 shows the measured evolution of R for the $\text{VO}_2/\text{Al}_2\text{O}_3$ sample for a fixed value of the fluence ϕ and substrate temperature, and the theoretical curves for this case that we obtain using the distribution $P(T_c)$ obtained for $\text{VO}_2/\text{Al}_2\text{O}_3$ and two different values of σ_K . We see that by choosing for σ_K the same value used for VO_2/TiO_2 , there is no agreement between theory and experiment. By setting $\sigma_K = 13000 \text{ W}/(\text{K cm}^2)$ we obtain excellent agreement. Indeed, all the experimental curves $R(t)$ for $\text{VO}_2/\text{Al}_2\text{O}_3$ are well approximated by the theoretical results assuming $\sigma_K = 13,000 \text{ W}/(\text{K cm}^2)$.

Figure 7.13 shows the time evolution of the VO_2 film and substrate temperatures (close to the interface) for the $\text{VO}_2/\text{Al}_2\text{O}_3$ film, panel (a), and for the VO_2/TiO_2 film, panel (b), using the parameter values summarized in Table 7.2. It helps to qualitatively understand the differences in the thermal relaxation between the two samples. Due to the lower values of the Kapitza constant, thermal energy stays more concentrated near the $\text{VO}_2\text{-TiO}_2$ interface, keeping the temperature of the VO_2 film above T_c longer.

To investigate the temperature dependence of the thermal relaxation we repeated the measurements while changing the base substrate temperature of the VO_2/TiO_2 sample. For these measurements the sample was placed inside a cryostat, and cooled down to temperatures $T_s(L)$ between 260 K and 298 K. The results of these measurements, along with the theoretical calculations, are shown in Figure 7.14. We again observe a good semiquantitative agreement between theoretical and experimental results. Also, note that the simple expression for the decay constant τ Eq. (7.16) captures the overall decay rate drop at lower substrate temperatures $T_s(L)$.

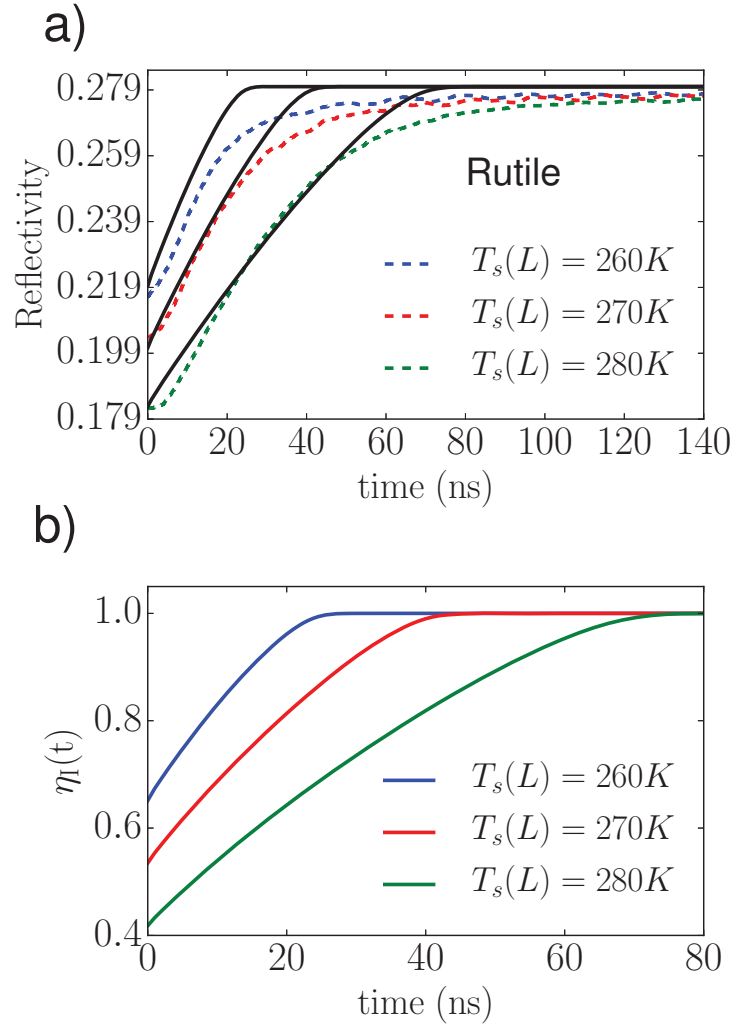


FIG. 7.10: (a) Time evolution of reflectivity after the photo-induced MIT for VO₂/TiO₂ for three different $T_s(L)$ and $\phi = 9 \text{ mJ/cm}^2$. The solid curves correspond to the theoretical results, and the dashed curves correspond to the experimental results. For the three theory curves we use $\sigma_K = 1100 \text{ W/(K cm}^2\text{)}$. Panel (b) shows the corresponding insulating fraction time evolution.

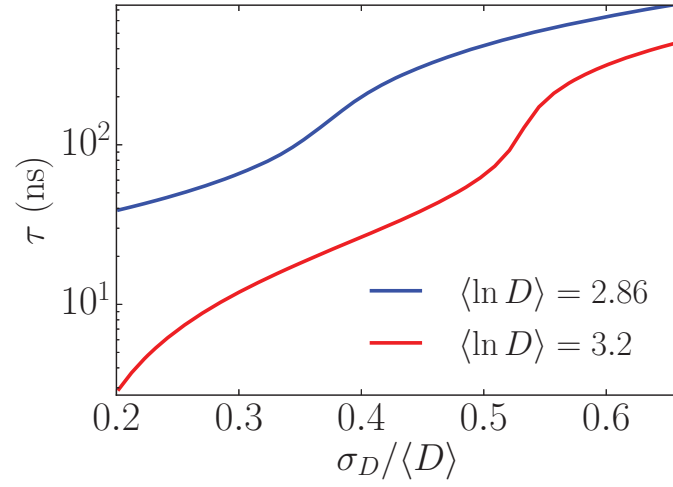


FIG. 7.11: Dependence of the VO₂/TiO₂ metal state decay time constant τ on σ_D for two values of $\langle \ln D \rangle$, as defined in Eq. (7.5), Kapitza constant $\sigma_K = 1100 \text{ W}/(\text{K cm}^2)$, substrate temperature $T_s(L) = 280 \text{ K}$, and initial fluence $\phi = 9 \text{ mJ}/\text{cm}^2$.

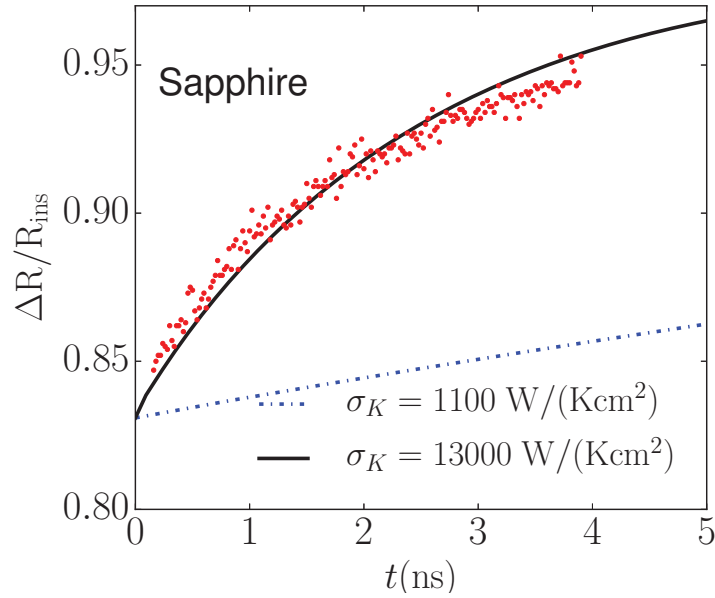


FIG. 7.12: VO₂/Al₂O₃ reflectivity time evolution after photo-induced MIT for $\phi = 7.5 \text{ mJ}/\text{cm}^2$. The red dots correspond to the experimental result. The dotted curve correspond to the theory with $\sigma_K = 1100 \text{ W}/(\text{K cm}^2)$, and the solid curve corresponds to $\sigma_K = 13000 \text{ W}/(\text{K cm}^2)$.

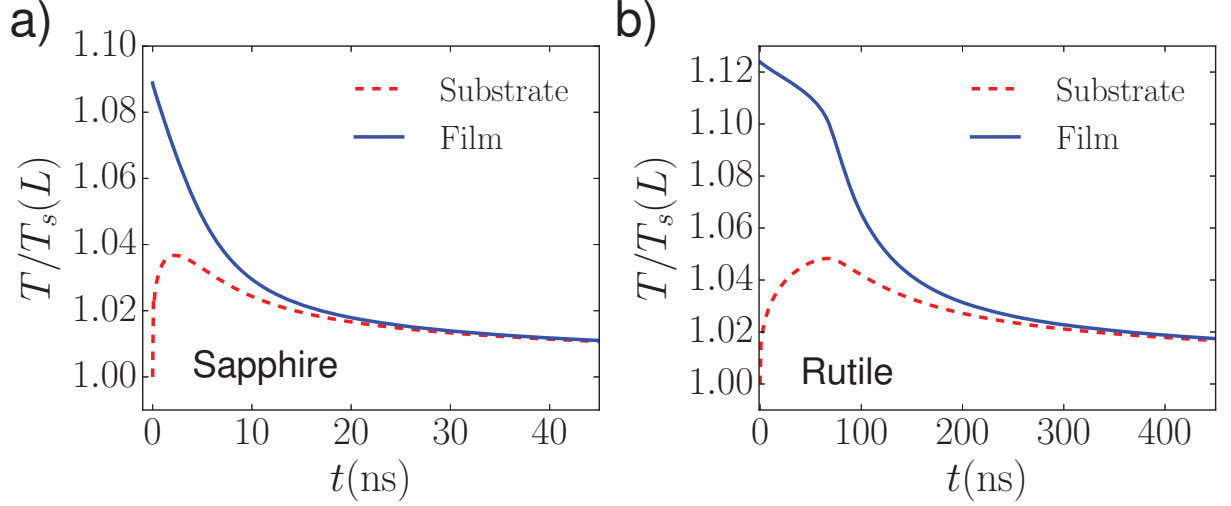


FIG. 7.13: Film and substrate temperature time evolution. For sapphire (a), $T_s(L) = 310$ K, and for rutile (b), $T_s(L) = 280$ K.

We point out that all the theoretical curves are obtained using the fixed set of parameters shown in Table 7.2. As mentioned above, the only unknown parameter that enters the theory is σ_K . In the results presented above σ_K was fixed to a single value for each film, and this value was then used to obtain the results for a range of experimental conditions with different substrate temperatures and pump fluences. For example, Fig. 7.3 shows an excellent agreement between the experimental measurements and theoretical calculations across the entire range of pump fluences, limited on the lower end by our ability to reliably detect the variation in the probe reflectivity, and on the upper end by the damage threshold of our sample (pump fluence $> 40 \text{ mJ/cm}^2$).

7.6 Conclusions

In conclusion, we have presented a combined experimental and theoretical study (done by Rodriguez-Vega) of the long timescale recovery dynamics of VO_2 films following an ultrafast photo-induced insulator-to-metal transition. We have developed a theoretical approach that is able to properly take into account the effect of inhomogeneities. The

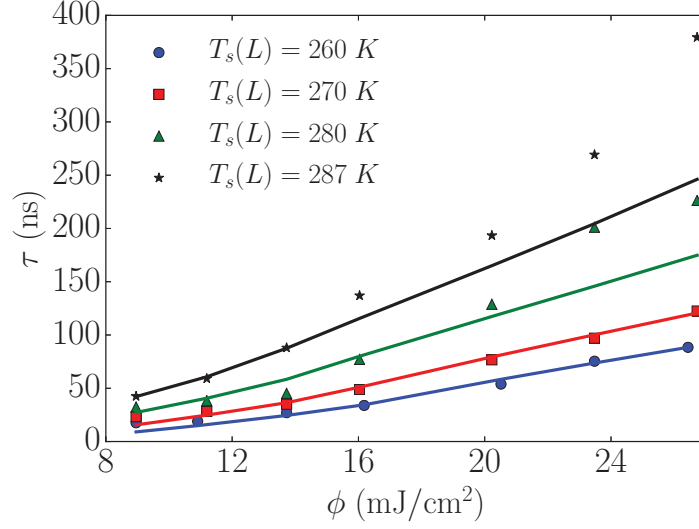


FIG. 7.14: Dependence of metal state decay constant τ on fluence and substrate temperature for VO_2/TiO_2 .

main results of this work are: (i) the derivation of the generalized heat equation (7.9) that properly takes into account that during the recovery, due to the inhomogeneities, only a fraction of the sample is undergoing the metal-to-insulator transition and correctly tracks the evolution in time of the metallic (insulating) phase; (ii) the clarification of the connection between the temperature dependent profile ($R(T)$) of the reflectivity across the thermally induced MIT and its dynamics after a photo-induced insulator-to-metal transition; (iii) the approximate relation, Eq. (7.16), between the characteristic time of the recovery dynamics and the parameters of the film, in particular to the standard deviation of the distribution of critical temperatures as extracted from $R(T)$; (iv) the ability of our theory to describe, using a fixed value of the Kapitza constant, the recovery dynamics for different values of the substrate temperature and pump fluence. By changing the pump fluence the characteristic time of the recovery can be changed, experimentally, by two orders of magnitude: our theory is able to account for such a change.

The theoretical approach that we present is general and can be used to describe the dynamics (in the adiabatic limit) of inhomogeneous systems across a first order phase

transition. The approximate relation between the characteristic time τ and the parameters of the system shows that τ is directly proportional to the width of the thermally activated transition. This result allows to estimate the recovery time of VO₂ films solely on the basis of a measurement of $R(T)$ across the MIT.

Assuming that variations of the size of the grains forming the films are the main source of inhomogeneities, using very general and fundamental relations between the grain size and the grain's critical temperature, we have been able to obtain the distribution of the grain sizes. In particular, we have been able to estimate the average grain's size and its standard deviation. We find that the calculated average grain's size is in remarkable semi-quantitative agreement with the one obtained from XRD measurements. For systems in which inhomogeneities are mostly due to variations of the size D of the grains, our analysis provides a way to obtain the size distribution $P(D)$ from the temperature dependent profile of the reflectivity across the thermally induced MIT. This could be very useful considering that $P(D)$ is a very challenging quantity to obtain via direct measurements.

CHAPTER 8

Directly pumping the lattice of VO₂ films with THz pulses

Very recently, a few experiments reported observation of the VO₂ phase transition induced by strong THz pulses [87, 88, 89]. Unlike an optical pump, such pulses are not sufficient to photoexcite the film across the bandgap.

Here we report on experiments using low-power (< 100 kV/cm) broadband pump pulses in the 0-12 THz spectral range to induce a partial insulator-to-metal transition in a VO₂ thin film, manifested by a change in the optical transmission. Our results demonstrate the possibility of inducing the transition at a significantly lower THz power, compared to previous results [88, 89], and thus provide an interesting new avenue for low-energy THz control of the VO₂ insulator-metal phase transition. In addition, unlike previous studies, we observe distinctly different transition dynamics in the THz-induced transition compared to the photo-induced one. We also investigate the potential role of a resonance interaction with IR-active phonon modes for VO₂, revealing the crucial role of the higher-frequency component of the THz pump pulse used. THz studies offer a new perspective on studies

of the MIT transition mechanism, as well as open new possibilities for applications.

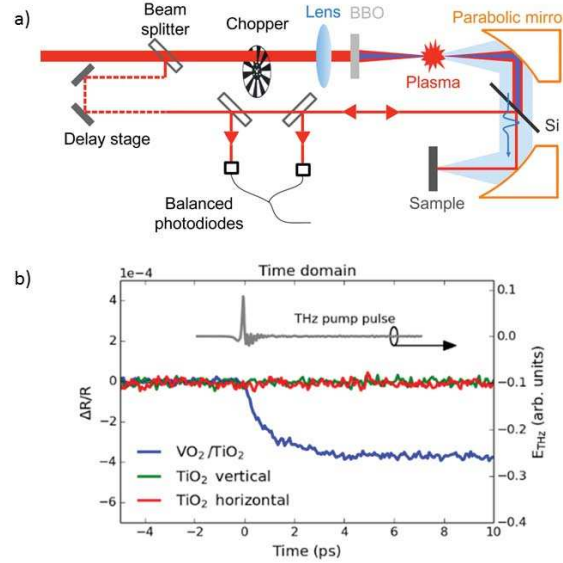


FIG. 8.1: (a) Schematics of the THz pump - optical probe experimental setup. (b) Optical probe reflection by the VO_2 film on a TiO_2 substrate and by the TiO_2 substrate only after interaction with the THz pump pulse.

For the measurements reported below, we used a 110 nm-thick VO_2 film grown on $500\mu\text{m}$ (011) TiO_2 substrate; detailed characterization of this film is found in Chapter 3.

We measured the film in a pump-probe configuration, with a THz pump with a frequency range of 0-12 THz and a probe at 800 nm. The THz pulse was produced with a shaped 800 nm, 35 fs pulse. The beam was split and one leg was frequency doubled with a BBO. Both pulses were then focused in a contained volume purged with nitrogen, producing the THz pulse. The THz pulse has 10% of the peak field above 100 kV/cm.

Another portion of the original 800 nm pulse was sent to a delay stage before being reflected off the front of the sample, so that the reflection could be probed in the optical range, as can be seen in figure 8.1 b). The optical probe reflection was measured in both cases with a balanced detector to reduce noise.

Using such pump-probe arrangement we have observed a small, but clearly detectable

change in the optical probe reflection of VO_2 after the interaction with the THz pump pulse. An example of the recorded signal is shown in Fig. 8.1(b). We see that immediately after the THz pump pulse arrival, the reflectivity of the VO_2 film starts to drop. Because of the low energy of the THz pulses, the observed relative change is significantly smaller than the value corresponding to the complete transition to a fully metallic VO_2 film [90]; nevertheless, the reflectivity drop is detectable with excellent signal-to-noise discrimination. Moreover, to verify that the observed reflectivity variation is due to the VO_2 film only, and not due to substrate itself, we repeated the measurements using a clean TiO_2 substrate, and clearly observed the absence of any changes in the probe reflection before and after the pump pulse.

We then investigated the dependence of the optical response as a function of the THz pump pulse energy, and observed the expected reduction of the reflectivity change $|\Delta R|/R$ for weaker pump pulses, as can be seen in Fig. 8.2(a). Interestingly, the dynamical change in reflectivity does not depend on the pump energy (at least in the experimentally tested range). To illustrate that, Fig. 8.2(b) displays the normalized reflectivity curves; it is easy to see that they overlap exactly (within the experimental noise).

It is useful to compare the THz-induced MIT with that induced by an IR optical pulse. The black curve in Fig. 8.2(b) represents the typical behavior of the optical reflectivity after a partial MIT induced by an approximately 100 fs optical pulse at 800nm wavelength on the same film, and a comprehensive analysis of the VO_2 photo-induced MIT dynamics in such case can be found in Refs. [12, 66]. In both cases we observed an instantaneous response after the arrival of the pump pulse. However, the dynamics of the transition observed in our experiment differs: while the IR optical pump pulse induced almost a step-like change at a timescale comparable with the pump pulse duration, the optical response triggered by a THz pump pulse of similar duration took a few ps to reach its new quasi steady state level that persists for several nanoseconds. This change can be fitted

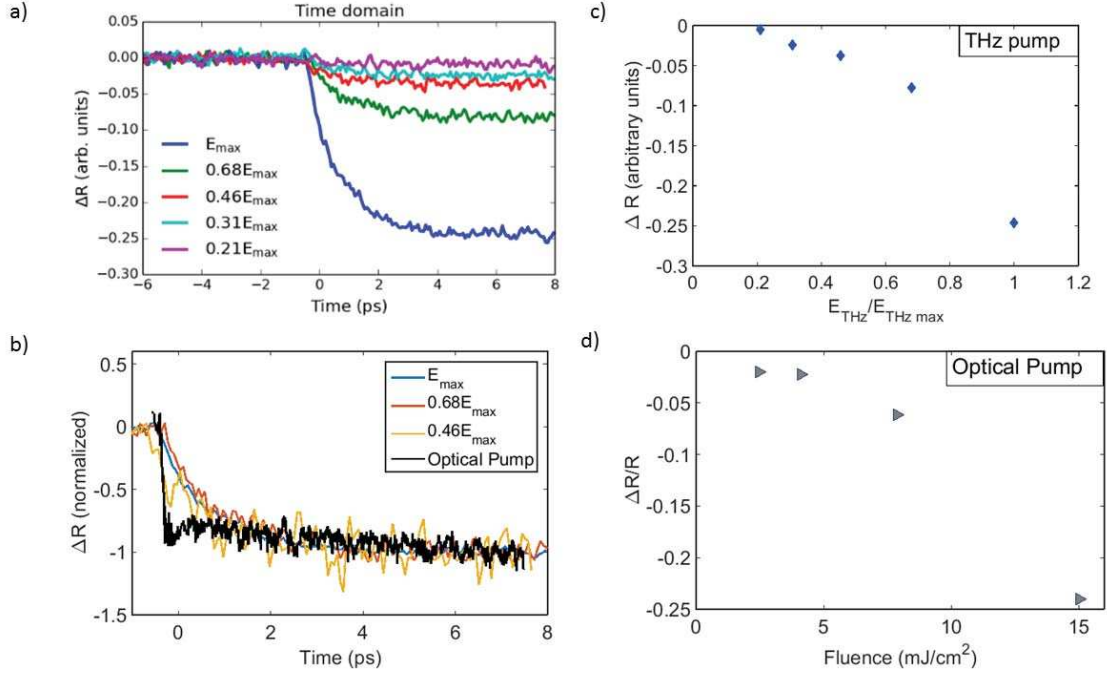


FIG. 8.2: a) shows the probe reflectivity response as the THz pump is attenuated. b) shows all the curves, normalized with respect to the max pump power of 100 kV/cm. Note that they all have the same rate of change over time before the change in reflection flattens out. This is different than the behavior of the film when pumped optically. c) and d) show the relationship between pump power and the resulting change in reflection for THz and 800 nm respectively.

with an exponential with a time constant of $\tau = 0.90 \pm 0.02$ ps. The optical pumped response shown in figure 8.2 b) has a time constant of $\tau = 12.4 \pm 0.3$ fs. The differences in the transition dynamics arise from the difference in transition mechanism induced by the two different pump pulses. The optical photons have energy higher than the VO_2 bandgap, and their absorption produce a photo-excited electron population, that can be the driving force in the insulator-to-metal transition that follows. However, a significantly lower THz photon energy, with a maximum of 0.03 eV, does not allow for this mechanism to play a role.

The time scale (few picoseconds) over which the reflectivity changes strongly suggests that changes in the lattice are the dominant mechanism responsible for the observed re-

sponse. This is consistent with the nature of our pump pulse given that: i) it contains only frequencies in the THz frequency range, i.e. with energies below the electronic band-gap $\Delta \sim 0.6$ eV and therefore cannot excite electrons from the valence band to the conduction band of the insulating phase of VO₂; ii) its maximum electric field is significantly lower than the threshold, a few MV/cm, required in VO₂ to create free electrons via the Poole-Frenkel effect¹ [87, 91, 89]. We are then led to conclude that the THz pulse induces the lattice transition from the monoclinic (M1), insulating, phase to the rutile, metallic, phase of a fraction of the VO₂. The A_g lattice modes of the M1 phase with frequencies 5.85 and 6.75 THz cause the stretching and tilting of the V-V dimers and induce the transition from the M1 structure to the rutile one [28, 32, 13]. In a previous study [41] on the same type of samples considered here, using Raman spectroscopy, we observed that the A_g mode with frequency 6.72 THz disappeared as the VO₂ film underwent the temperature driven transition from insulating to metallic. The A_g modes are Raman active. The infrared active modes are the A_u and B_u modes that are odd with respect to space inversion. The M1 lattice structure of VO₂ belongs to the $P2_1/c$ space group [92] and therefore it is expected to have 3 acoustic modes, 18 Raman active modes, and 15 infrared active modes, for a total of 36 phonon modes. Within the range of frequencies of our pump pulse the dominant modes are two A_u modes with wavenumbers 281 cm⁻¹ [93, 94] and 310 cm⁻¹ [93, 94] respectively, and two B_u modes with wavenumbers 277 cm⁻¹, 324 cm⁻¹, respectively [93, 94]. Considering the relative orientation between the laser beam and the film in our setup, the pump pulse will excite both A_u and B_u modes. Our VO₂ films are formed by grains of different sizes [68]; the presence of defects and grain boundaries breaks the centrosymmetry of the system and allows the mixing of odd and even, A_g , phonon modes. We then expect that the odd modes with frequencies within the pump pulse bandwidth will generate A_g modes

¹The Poole-Frenkel effect is where an insulator can become conductive via large electric fields, such that small thermal fluctuations are sufficient to allow localized electrons to travel from site to site in the lattice.[91]

by scattering off the defects and the boundaries of the grains forming our VO_2 films. In addition, phonon-phonon scattering processes involving three or more phonons, due to anharmonicity, will also contribute to the conversion of the infrared active modes to the A_g modes that drive the M1-to-rutile structural transition [95].

These facts suggest that THz radiation at frequencies around 6 THz may have the strongest effect on the MIT in this film. Since direct analysis of the VO_2 absorption spectra in our experiment was made impossible by the broadband absorption of the THz radiation by the substrate material (TiO_2), we relied on a spectral filtering technique to determine the relative contributions of the different THz frequencies. In particular, we compare the optical response of the VO_2 when using a full-bandwidth pump pulse (approximately 0–12 THz) and when the frequency components above approximately 3 THz were blocked before interacting with the sample. Fig.8.3 (a,b) shows the temporal and spectral profiles of the two pump pulses, used in this measurement. We also made sure that the peak electric fields for both pulses were the same. Fig. 8.3(c) clearly shows that while the attenuated broadband THz pulse produced a clear change in the film's reflectivity, the filtered pulse fails to do so. This implies the critical role of the higher-frequency components in the THz-induced MIT, at least for the regime of weak THz pump pulses.

In conclusion, we report the observation of the metal-to-insulator transition in a multi-grain 110-nm VO_2 film, induced by low-energy THz pulses. Using a THz pump - IR probe experimental arrangement, we demonstrate that the THz pump pulse produces a long-lasting effect on the optical response of the film that we can attribute to the onset of a partially metallic state. We observed a clear nonlinear dependence of the observed variation with THz pulse energy, with a threshold value around 20 kV/cm. The change in optical reflectivity did not happen instantaneously, like in the case of the optical pump pulses or previously reported experiments with strong THz pulses; instead it followed an exponential decay with a time constant of around 1 ps. This slower response hints that the

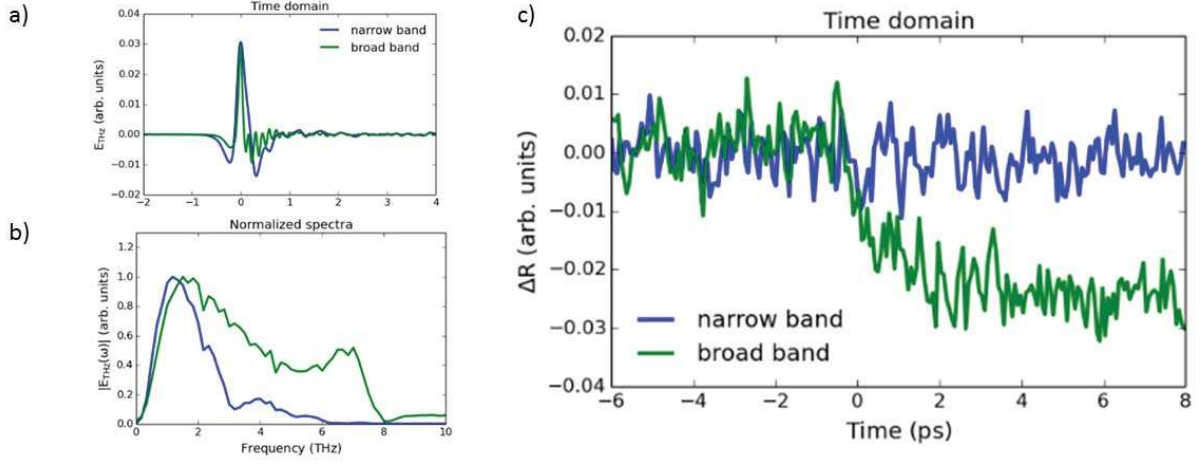


FIG. 8.3: Electric field temporal profiles (a) and spectra (b) for an attenuated broadband and spectrally filtered THz pump pulses. The sharp cut-off of the unfiltered THz pulse spectrum at 8 THz is due to detector response; actual pulse extends to 12 THz. (c) Recorded optical response of the VO_2 film to these THz pump pulses.

transition may be triggered by the resonant interaction of the THz pump with the VO_2 lattice. This suggestion is supported by the fact that when the frequency components above 3 THz are removed from the pump pulse, the optical response disappears, compare to the broad-band pulse with the same peak electric field. Our measurements reveal that the presence of defects and grain boundaries in VO_2 films allows the use of low-power, low-field, THz pulses to drive the insulator-to-metal transition. This opens a new avenue to tune and control the structural and electronic phases of VO_2 .

CHAPTER 9

Conclusion and Outlook

9.1 Summary

In this work, I have looked at how the inhomogeneities and microstructure of vanadium dioxide changes the properties of the photo-induced insulator-metal transition. While the effects of thin film microstructure on the heat induced transition has been well studied, we are the first to take a look at how two very different films will have different ultra-fast responses. In Chapter 5 we mapped out the threshold responses for VO_2 on TiO_2 and Al_2O_3 , and saw a scaling in fluence thresholds for different dynamic behaviors, based on what critical temperature T_c each film has.

I also have looked at, in conjunction with Matt Simons and Martin Rodriguez-Vega, the long time-scale recovery back to the insulating state of the same two samples, as discussed in Chapter 7. Again, both show very different behaviors in recovery. The film on TiO_2 takes two orders of magnitude longer than the film on Al_2O_3 , despite having a lower transition temperature. While the recovery time does limit VO_2 's applications as a switch, a longer recovery opens up the possibility of the material being used for short term memory, as temporary circuits could be induced in the film by a light source. Rodriguez-

Vega’s theoretical modeling shows that while the grain size and strain do play a role in the recovery time, it’s the heat dissipation through the film-substrate interface, as defined by the Kapitza constant σ_K , that limits the recovery time τ of the VO_2 thin films.

We have also looked at a sub-picosecond feature that is present in the $\Delta R/R$ of our ultrafast measurements when the pump and the probe have polarizations parallel to each other. This feature has not been reported before, and is present in both the film on TiO_2 and the film on Al_2O_3 . Each film’s feature has it’s own time-scale that does not depend on the power of the pump, or the pulse duration of the beam. The time scale does not correspond to any measured phonon modes, and is most likely a plasmonic response in the film. Further study will be required to determine what exactly is the mechanism behind the oscillation in reflection.

Lastly, I collaborated with Dr. Yamaguchi’s group at RPI, where we pumped VO_2 with a broadband THz pump, and measured $\Delta R/R$ with an 800 nm probe. We saw a response in the VO_2 on TiO_2 that scaled with the power of the pump. The THz pump has insufficient energy to photoexcite the electrons across the gap, so any pumping of the system must be through the lattice. The timescale of the $\Delta R/R$ confirms this supposition, as there is a slower response from the film than there is for the optically pumped measurements.

9.2 Outlook

There are several different avenues of study that could be pursued after this body of work. Other works have reported seeing coherent phonon oscillations in similar pump-probe experiments.[96] The fact that we can stimulate coherent phonon oscillations with an 800 nm pump suggests that the photoexcitation of the electrons across the gap cannot be completely decoupled from pumping the lattice. If the lattice is the primary driving mechanism for the phase transition, then it would be interesting to look at the life-time of

coherent phonons in different films, and see if there is a relationship between the dynamics and coherent phonon modes. We have been unable to see any coherent phonon modes in any of our samples. Our pulses are sufficiently short enough that we should be able to resolve the lowest energy Raman modes at 233 fs (149 cm^{-1})[97]. We have been unable to resolve any phonon modes at room temperature. In the future, we would like to attempt to take high resolution measurements of $\Delta R/R$ in a cryostat, in order to reduce background thermal noise.

Another interesting avenue of study would be to perform these measurements with a series of films grown on the same substrate, with different thicknesses, much in the way that others have done[48]. I have done most of the work with two very dramatically different films, which has the value of contrasting the behavior deriving from very different microstructures, but does limit how much we can infer causes in a way that a more systematic study would allow us to.

BIBLIOGRAPHY

- [1] J. B. Goodenough, *Journal of Solid State Chemistry* **3**, 490 (1971), ISSN 00224596, URL [http://dx.doi.org/10.1016/0022-4596\(71\)90091-0](http://dx.doi.org/10.1016/0022-4596(71)90091-0).
- [2] M. Imada, A. Fujimori, and Y. Tokura, *Reviews of Modern Physics* **70**, 1039 (1998), ISSN 0034-6861, URL http://rmp.aps.org/abstract/RMP/v70/i4/p1039_1
<http://link.aps.org/doi/10.1103/RevModPhys.70.1039>.
- [3] H. Verleur, A. B. Jr, and C. Berglund, *Physical Review* (1968), URL http://prola.aps.org/abstract/PR/v172/i3/p788_1.
- [4] R. W. G. Wyckoff, *Crystal Structures*, vol. 1 (Interscience Publishers, New York, New York, 1963), 2nd ed.
- [5] C. G. Granqvist, *Solar Energy Materials and Solar Cells* **91**, 1529 (2007), ISSN 09270248, URL <http://dx.doi.org/10.1016/j.solmat.2007.04.031>.
- [6] T. D. Manning and I. P. Parkin, *Journal of Materials Chemistry* **14**, 2554 (2004), ISSN 0959-9428, URL <http://pubs.rsc.org/en/content/articlehtml/2004/jm/b403576n>.
- [7] A. Zylbersztejn and N. Mott, *Physical Review B* (1975), URL <http://journals.aps.org/prb/abstract/10.1103/PhysRevB.11.4383>.

- [8] A. Cavalleri, C. Tóth, C. Siders, J. A. Squier, F. Ráksi, P. Forget, and J. C. Kieffer, *Physical Review Letters* **87**, 237401 (2001), ISSN 0031-9007, URL <http://link.aps.org/doi/10.1103/PhysRevLett.87.237401>.
- [9] D. J. Hilton, R. P. Prasankumar, S. Fourmaux, A. Cavalleri, D. Brasseur, M. A. El Khakani, J. C. Kieffer, A. J. Taylor, and R. D. Averitt, *Physical Review Letters* **99**, 1 (2007), ISSN 0031-9007, URL <http://link.aps.org/doi/10.1103/PhysRevLett.99.226401>.
- [10] D. Wegkamp, M. Herzog, L. Xian, M. Gatti, P. Cudazzo, C. L. McGahan, R. E. Marvel, R. F. Haglund, A. Rubio, M. Wolf, et al., *Physical Review Letters* **113**, 216401 (2014), ISSN 0031-9007, URL <http://link.aps.org/doi/10.1103/PhysRevLett.113.216401>.
- [11] Z. Tao, T.-R. Han, S. Mahanti, P. Duxbury, F. Yuan, C.-Y. Ruan, K. Wang, and J. Wu, *Physical Review Letters* **109**, 1 (2012), ISSN 0031-9007, URL <http://link.aps.org/doi/10.1103/PhysRevLett.109.166406>.
- [12] T. Cocker, L. Titova, S. Fourmaux, G. Holloway, H.-C. Bandulet, D. Brassard, J.-C. Kieffer, M. El Khakani, and F. Hegmann, *Physical Review B* **85**, 155120 (2012), ISSN 1098-0121, URL <http://link.aps.org/doi/10.1103/PhysRevB.85.155120>.
- [13] C. Kübler, H. Ehrke, R. Huber, R. Lopez, a. Halabica, R. Haglund, and a. Leitenstorfer, *Physical Review Letters* **99**, 116401 (2007), ISSN 0031-9007, URL <http://link.aps.org/doi/10.1103/PhysRevLett.99.116401>.
- [14] K. Okazaki, H. Wadati, A. Fujimori, and M. Onoda, *Physical Review B* **69**, 1 (2004), 0312112, URL <http://prb.aps.org/abstract/PRB/v69/i16/e165104>.

- [15] F. F. Morin, Physical Review Letters **3**, 2 (1959), ISSN 0031-9007, URL <http://link.aps.org/doi/10.1103/PhysRevLett.3.34>
https://noppa.tkk.fi/noppa/kurssi/ke-35.2100/luennot/KE-35_2100_mit-efekti.pdf.
- [16] D. N. Basov, R. D. Averitt, D. van der Marel, M. Dressel, and K. Haule, Reviews of Modern Physics **83**, 471 (2011), ISSN 0034-6861, URL <http://link.aps.org/doi/10.1103/RevModPhys.83.471>.
- [17] R. Pynn, J. Axe, and P. Raccach, Physical Review B **17**, 2196 (1978), ISSN 0163-1829, URL <http://link.aps.org/doi/10.1103/PhysRevB.17.2196>.
- [18] A. Tselev, I. A. Luk'yanchuk, I. N. Ivanov, J. D. Budai, J. Z. Tischler, E. Strelcov, A. Kolmakov, and S. V. Kalinin, Nano letters **10**, 4409 (2010), ISSN 1530-6992, URL <http://www.ncbi.nlm.nih.gov/pubmed/20939599>.
- [19] T. Kikuzuki, R. Takahashi, and M. Lippmaa, Physical Review B **82**, 144113 (2010), ISSN 1098-0121, URL <http://link.aps.org/doi/10.1103/PhysRevB.82.144113>.
- [20] K. G. West, J. Lu, L. He, D. Kirkwood, W. Chen, T. P. Adl, M. S. Osofsky, S. B. Qadri, R. Hull, and S. a. Wolf, Journal of Superconductivity and Novel Magnetism **21**, 87 (2008), ISSN 1557-1939, URL <http://link.springer.com/10.1007/s10948-007-0303-y>.
- [21] E. Abreu, M. Liu, J. Lu, K. G. West, S. Kittiwatanakul, W. Yin, S. A. Wolf, and R. D. Averitt, New Journal of Physics **14**, 083026 (2012), ISSN 1367-2630, URL <http://stacks.iop.org/1367-2630/14/i=8/a=083026?key=crossref.667002eceb37a5408851>.
- [22] J. Lu, K. G. West, and S. a. Wolf, Applied Physics Letters **93**, 262107 (2008), ISSN 00036951, URL <http://link.aip.org/link/APPLAB/v93/i26/p262107/s1&Agg=doi>.

- [23] S. Kittiwatanakul, J. Lu, and S. a. Wolf, *Applied Physics Express* **4**, 091104 (2011), ISSN 1882-0778, URL <http://stacks.iop.org/1882-0786/4/091104> <http://apex.jsap.jp/link?APEX/4/091104/>.
- [24] T. Kikuzuki and M. Lippmaa, *Applied Physics Letters* **96**, 132107 (2010), ISSN 00036951, URL <http://link.aip.org/link/APPLAB/v96/i13/p132107/s1&Agg=doi>.
- [25] N. Aetukuri, A. Gray, M. Drouard, and M. Cossale, *Nature Physics* pp. 1–17 (2013), URL <http://www.nature.com/nphys/journal/v9/n10/abs/nphys2733.html>.
- [26] J. H. Park, J. M. Coy, T. S. Kasirga, C. Huang, Z. Fei, S. Hunter, and D. H. Cobden, *Nature* **500**, 431 (2013), ISSN 0028-0836, URL <http://www.nature.com/doifinder/10.1038/nature12425>.
- [27] N. W. Ashcroft and N. D. Mermin, *Solid State Physics* (Brooks/Cole, Belmont, CA, 1976).
- [28] D. Paquet and P. Leroux-Hugon, *Physical Review B* **22**, 5284 (1980), URL <http://journals.aps.org/prb/abstract/10.1103/PhysRevB.22.5284>.
- [29] G. Stefanovich, a. Pergament, and D. Stefanovich, *Journal of Physics: Condensed Matter* **12**, 8837 (2000), ISSN 0953-8984, URL <http://iopscience.iop.org/0953-8984/12/41/310>.
- [30] G. Gopalakrishnan, D. Ruzmetov, and S. Ramanathan, *Journal of Materials Science* **44**, 5345 (2009), ISSN 0022-2461, URL <http://www.springerlink.com/index/10.1007/s10853-009-3442-7>.
- [31] W. R. Roach and I. Balberg, *Solid State Communications* **9**, 551 (1971), ISSN 00381098.

- [32] A. Cavalleri, T. Dekorsy, H. Chong, J. Kieffer, and R. Schoenlein, *Physical Review B* **70**, 161102 (2004), ISSN 1098-0121, URL <http://link.aps.org/doi/10.1103/PhysRevB.70.161102>.
- [33] M. Becker and A. Buckman, *Applied physics ...* **65**, 1507 (1994), URL http://ieeexplore.ieee.org/xpls/abs_all.jsp?arnumber=4883887
<http://scitation.aip.org/content/aip/journal/apl/65/12/10.1063/1.112974>.
- [34] R. A. Aliev, V. N. Andreev, V. M. Kapralova, V. A. Klimov, A. I. Sobolev, and E. B. Shadrin, *Physics of the Solid State* **48**, 929 (2006), ISSN 1063-7834, URL <http://link.springer.com/10.1134/S1063783406050180>.
- [35] G. Xu, P. Jin, M. Tazawa, and K. Yoshimura, *Applied Surface Science* **244**, 449 (2005), ISSN 01694332, URL <http://linkinghub.elsevier.com/retrieve/pii/S0169433204017350>.
- [36] I. Khakhaev, F. A. Chudnovskii, and E. B. Shadrin, *Physics of the Solid State* **36**, 898 (1994), URL <http://adsabs.harvard.edu/abs/1994PhSS...36..898K>.
- [37] M. M. Qazilbash, M. Brehm, B.-G. Chae, P.-C. Ho, G. O. Andreev, B.-J. Kim, S. J. Yun, A. V. Balatsky, M. B. Maple, F. Keilmann, et al., *Science* **318**, 1750 (2007), ISSN 1095-9203, URL <http://www.ncbi.nlm.nih.gov/pubmed/18079396>.
- [38] L. Wang, I. Novikova, J. M. Klopff, S. Madaras, G. P. Williams, E. Madaras, J. Lu, S. A. Wolf, and R. A. Lukaszew, *Advanced Optical Materials* **2**, 30 (2014), ISSN 21951071.
- [39] J. Y. Suh, R. Lopez, L. C. Feldman, and R. F. Haglund, *Journal of Applied Physics* **96**, 1209 (2004), ISSN 00218979, URL <http://scitation.aip.org/content/aip/journal/jap/96/2/10.1063/1.1762995>.

- [40] Y. Muraoka and Z. Hiroi, Applied Physics Letters **80**, 583 (2002), ISSN 00036951, URL <http://link.aip.org/link/APPLAB/v80/i4/p583/s1&Agg=doi>.
- [41] E. Radue, E. Crisman, L. Wang, S. Kittiwatanakul, J. Lu, S. A. Wolf, R. Wincheski, R. A. Lukaszew, and I. Novikova, Journal of Applied Physics **113**, 233104 (2013).
- [42] P. Scherrer, Nachr. Ges. Wiss. Göttingen, Math.-Phys. Kl. **26**, 98 (1918).
- [43] M. Schubert, Physical review. B, Condensed matter **53**, 4265 (1996), ISSN 0163-1829, URL <http://www.ncbi.nlm.nih.gov/pubmed/9983979>.
- [44] P. Schilbe, Physica B **317**, 600 (2002).
- [45] M. Pan, J. Liu, H. Zhong, S. Wang, Z.-f. Li, X. Chen, and W. Lu, Journal of Crystal Growth **268**, 178 (2004), ISSN 00220248, URL <http://linkinghub.elsevier.com/retrieve/pii/S0022024804005585>.
- [46] X.-B. Chen, Journal of the Korean Physical Society **58**, 100 (2011), ISSN ISSN 0374-4884, URL <http://inis.iaea.org/Search/search.aspx?orig.q=RN:43045741>.
- [47] K. Appavoo, D. Y. Lei, Y. Sonnefraud, B. Wang, S. T. Pantelides, S. a. Maier, and R. F. Haglund, Nano letters **12**, 780 (2012), ISSN 1530-6992, URL <http://www.ncbi.nlm.nih.gov/pubmed/22273268>.
- [48] N. B. Aetukuri, A. X. Gray, M. Drouard, M. Cossale, L. Gao, A. H. Reid, R. Kukreja, H. Ohldag, C. a. Jenkins, E. Arenholz, et al., Nature Physics **9**, 661 (2013), ISSN 1745-2473, URL <http://www.nature.com/doifinder/10.1038/nphys2733>.
- [49] S. Kittiwatanakul, S. A. Wolf, and J. Lu, Applied Physics Letters **105**, 1 (2014), ISSN 00036951, 1406.7412.

- [50] J. Laverock, L. F. J. Piper, A. R. H. Preston, B. Chen, J. McNulty, K. E. Smith, S. Kittiwatanakul, J. W. Lu, S. A. Wolf, P.-A. Glans, et al., *Physical Review B* **85**, 081104 (2012), ISSN 1098-0121, URL <http://link.aps.org/doi/10.1103/PhysRevB.85.081104>.
- [51] K. Sokolowski-Tinten, A. Cavalleri, and D. V. D. Linde, *Applied Physics A* **69**, 577 (1999).
- [52] C. Rulliere, *Femtosecond Laser pulses* (Springer Science + Business Media, Inc., New York, New York, 2010), 2nd ed.
- [53] F. L. Pedrotti, L. S. Pedrotti, and L. M. Pedrotti, *Introduction to Optics* (Person Education, Inc., Glenview, IL, 2007), 3rd ed.
- [54] M. M. Qazilbash, K. S. Burch, D. Whisler, D. Shrekenhamer, B. G. Chae, H. T. Kim, and D. N. Basov, *Physical Review B* **74**, 1 (2006), ISSN 1098-0121, URL <http://link.aps.org/doi/10.1103/PhysRevB.74.205118>.
- [55] M. K. Liu, M. Wagner, E. Abreu, S. Kittiwatanakul, A. McLeod, Z. Fei, M. Goldflam, S. Dai, M. M. Fogler, J. Lu, et al., *Physical Review Letters* **111**, 1 (2013), ISSN 0031-9007, URL <http://link.aps.org/doi/10.1103/PhysRevLett.111.096602>.
- [56] E. Abreu, S. Wang, G. Ramirez, and M. Liu, arXiv preprint arXiv: ... (2014), arXiv:1410.6804v1, URL <http://arxiv.org/abs/1410.6804>.
- [57] S. Biermann, A. Poteryaev, A. I. Lichtenstein, and A. Georges, *Physical Review Letters* **94**, 026404 (2005), ISSN 0031-9007, 0410005v1, URL <http://link.aps.org/doi/10.1103/PhysRevLett.94.026404>.
- [58] D. Brassard, S. Fourmaux, M. Jean-Jacques, J. C. Kieffer, and M. a. El

- Khakani, Applied Physics Letters **87**, 051910 (2005), ISSN 00036951, URL <http://link.aip.org/link/APPLAB/v87/i5/p051910/s1&Agg=doi>.
- [59] T. L. Cocker, L. V. Titova, S. Fourmaux, H. C. Bandulet, D. Brasseur, J. C. Kieffer, M. a. El Khakani, and F. a. Hegmann, Applied Physics Letters **97**, 221905 (2010), ISSN 00036951, URL <http://link.aip.org/link/APPLAB/v97/i22/p221905/s1&Agg=doi>.
- [60] C. Berglund and H. Guggenheim, Physical Review **185**, 1022 (1969), URL http://prola.aps.org/abstract/PR/v185/i3/p1022_1 <http://journals.aps.org/pr/abstract/10.1103/PhysRev.185.1022>.
- [61] H. T. Kim, Y. W. Lee, B. J. Kim, B. G. Chae, S. J. Yun, K. Y. Kang, K. J. Han, K. J. Yee, and Y. S. Lim, Physical Review Letters **97**, 10 (2006), ISSN 00319007, 0608085.
- [62] M. Rini, Z. Hao, R. W. Schoenlein, C. Giannetti, F. Parmigiani, S. Fourmaux, J. C. Kieffer, a. Fujimori, M. Onoda, S. Wall, et al., Applied Physics Letters **92**, 181904 (2008), ISSN 00036951, URL <http://link.aip.org/link/APPLAB/v92/i18/p181904/s1&Agg=doi>.
- [63] A. Pashkin, C. Kübler, H. Ehrke, R. Lopez, A. Halabica, R. Haglund, R. Huber, and A. Leitenstorfer, Physical Review B **83**, 195120 (2011), ISSN 1098-0121, URL <http://link.aps.org/doi/10.1103/PhysRevB.83.195120>.
- [64] E. Abreu, M. Liu, J. Lu, K. G. West, S. Kittiwatanakul, W. Yin, S. a. Wolf, and R. D. Averitt, New Journal of Physics **14**, 083026 (2012), ISSN 1367-2630, URL <http://stacks.iop.org/1367-2630/14/i=8/a=083026?key=crossref.667002eceb37a5408851>

- [65] S. Wall, L. Foglia, D. Wegkamp, K. Appavoo, J. Nag, R. F. Haglund, J. Stähler, and M. Wolf, *Physical Review B* **87**, 1 (2013), ISSN 1098-0121, URL <http://link.aps.org/doi/10.1103/PhysRevB.87.115126>.
- [66] E. Radue, L. Wang, S. Kittiwatanakul, J. Lu, S. a. Wolf, E. Rossi, R. a. Lukaszew, and I. Novikova, *Journal of Optics* **17**, 025503 (2015), ISSN 2040-8978, URL <http://stacks.iop.org/2040-8986/17/i=2/a=025503?key=crossref.402967563bdc6925fc1>.
- [67] S. Lysenko, V. Vikhnin, F. Fernandez, a. Rua, and H. Liu, *Physical Review B* **75**, 075109 (2007), ISSN 1098-0121, URL <http://link.aps.org/doi/10.1103/PhysRevB.75.075109>.
- [68] M. Rodriguez-Vega, M. T. Simons, E. Radue, S. Kittiwatanakul, J. Lu, S. A. Wolf, R. A. Lukaszew, I. Novikova, and E. Rossi, *Physical Review B* **92**, 1 (2015), ISSN 2040-8978, [arXiv:1504.05954v1](#).
- [69] D. A. G. Bruggeman, *Annalen der Physik* **416**, 636 (1935), ISSN 00033804, URL <http://doi.wiley.com/10.1002/andp.19354160705>.
- [70] R. Landauer, *Journal of Applied Physics* **23**, 779 (1952), ISSN 00218979.
- [71] X. C. Zeng, D. J. Bergman, P. M. Hui, and D. Stroud, *Physical Review B* **38**, 10970 (1988), ISSN 01631829.
- [72] E. Rossi, S. Adam, and S. Das Sarma, *Physical Review B - Condensed Matter and Materials Physics* **79**, 1 (2009), ISSN 10980121, 0809.1425.
- [73] J. B. Kana Kana, J. M. Ndjaka, G. Vignaud, A. Gibaud, and M. Maaza, *Optics Communications* **284**, 807 (2011), ISSN 00304018, URL <http://dx.doi.org/10.1016/j.optcom.2010.10.009>.

- [74] C. G. Granqvist and R. a. Buhrman, Journal of Applied Physics **47**, 2200 (1976).
- [75] M. E. Fisher and A. N. Berker, Physical Review B **26**, 2507 (1982), ISSN 01631829.
- [76] M. S. S. Challa, D. P. Landau, and K. Binder, Physical Review B **34**, 1841 (1986), ISSN 01631829.
- [77] M. Zhang, M. Y. Efremov, F. Schiettekatte, E. A. Olson, A. T. Kwan, S. L. Lai, T. Wisleder, J. E. Greene, and L. H. Allen, Physical Review B - Condensed Matter and Materials Physics **62**, 10548 (2000), ISSN 01631829.
- [78] Q. Jiang, J. C. Li, and B. Q. Chi, Chemical Physics Letters **366**, 551 (2002), ISSN 00092614.
- [79] P. L. Kapitza, J. Phys. USSR **4** (1941).
- [80] G. L. Pollack, Reviews of Modern Physics **41**, 48 (1969).
- [81] R. Stoner and H. Maris, Physical review. B, Condensed matter **48**, 16373 (1993), ISSN 0163-1829, URL <http://www.ncbi.nlm.nih.gov/pubmed/10008218>.
- [82] H. Wen, L. Guo, E. Barnes, J. H. Lee, D. a. Walko, R. D. Schaller, J. a. Moyer, R. Misra, Y. Li, E. M. Dufresne, et al., Physical Review B **88**, 165424 (2013), ISSN 1098-0121, URL <http://link.aps.org/doi/10.1103/PhysRevB.88.165424>.
- [83] D. W. Oh, C. Ko, S. Ramanathan, and D. G. Cahill, Applied Physics Letters **96**, 0 (2010), ISSN 00036951.
- [84] D. De Ligny, P. Richet, E. F. Westrum, and J. Roux, Physics and Chemistry of Minerals **29**, 267 (2002), ISSN 03421791.
- [85] W. R. Thurber and A. J. H. Mante, Phys. Rev. **139**, A1655 (1965), URL <http://link.aps.org/doi/10.1103/PhysRev.139.A1655>.

- [86] V. Pishchik, L. a. Lytvynov, and E. R. Dobrovinskaya, *Sapphire: Material, Manufacturing, Applications* (Springer US, 2009), 1st ed., ISBN 978-0-387-85694-0, URL <http://link.springer.com/10.1007/978-0-387-85695-7>.
- [87] M. Liu, H. Y. Hwang, H. Tao, A. C. Strikwerda, K. Fan, G. R. Keiser, A. J. Sternbach, K. G. West, S. Kittiwatanakul, J. Lu, et al., *Nature* **487**, 345 (2012), ISSN 1476-4687, URL <http://www.ncbi.nlm.nih.gov/pubmed/22801506>.
- [88] K. Martens, J. W. Jeong, N. Aetukuri, C. Rettner, N. Shukla, E. Freeman, D. N. Esfahani, F. M. Peeters, T. Topuria, P. M. Rice, et al., *Physical Review Letters* **115**, 2 (2015), ISSN 10797114.
- [89] A. X. Gray, J. Jeong, N. P. Aetukuri, P. Granitzka, Z. Chen, R. Kukreja, and D. Higley, arXiv preprint arXiv: ... (2015).
- [90] P. Mandal, A. Speck, C. Ko, and S. Ramanathan, *Optics Letters* **36**, 1927 (2011), ISSN 0146-9592, URL <https://www.osapublishing.org/abstract.cfm?URI=ol-36-10-1927>.
- [91] J. G. Simmons, *Physical Review* **155**, 657 (1967), ISSN 0031-899X, URL <http://link.aps.org/doi/10.1103/PhysRev.155.657>.
- [92] V. Eyert, **11**, 61 (2002), 0210558, URL <http://arxiv.org/abs/cond-mat/0210558>.
- [93] a. Barker, H. Verleur, and H. Guggenheim, *Physical Review Letters* **17**, 1286 (1966), ISSN 0031-9007, URL <http://link.aps.org/doi/10.1103/PhysRevLett.17.1286>.
- [94] T. J. Huffman, P. Xu, M. M. Qazilbash, E. J. Walter, H. Krakauer, J. Wei, D. H. Cobden, H. A. Bechtel, M. C. Martin, G. L. Carr, et al., *Physical Review B* **87**, 115121 (2013), ISSN 1098-0121, URL <http://link.aps.org/doi/10.1103/PhysRevB.87.115121>.

- [95] M. Först, R. Mankowsky, H. Bromberger, D. Fritz, H. Lemke, D. Zhu, M. Chollet, Y. Tomioka, Y. Tokura, R. Merlin, et al., Solid State Communications **169**, 24 (2013), ISSN 00381098, URL <http://linkinghub.elsevier.com/retrieve/pii/S0038109813002901>.
- [96] L. Foglia, Ph.D. thesis, Fritz-Haber-Institut der Max-Planck-Gesellschaft (2011), URL <http://pubman.mpdl.mpg.de/pubman/item/escidoc:1375221:2/component/escidoc:1375221:2>.
- [97] P. Schilbe and D. Maurer, Materials Science and Engineering: A **370**, 449 (2004), ISSN 09215093, URL <http://linkinghub.elsevier.com/retrieve/pii/S0921509303009407>.

VITA

Elizabeth Radue

Elizabeth Radue was born in 1987 in the District of Columbia, and grew up in Mount Airy, MD. As a young girl she dreamed of being a writer/astronaut/ballerina/scientist/dolphin trainer; she figures one out of five isn't bad. She attended Sandy Spring Friends School from 1992-2005. She graduated from Mount Holyoke College cum laude in 2009 with a B.A. in physics. She entered College of William and Mary in Williamsburg, Virginia in Fall 2010 and joined Irina Novikova's group in the summer of 2011. She has worked on the vanadium dioxide project in collaboration with Ale Lukaszew's group.